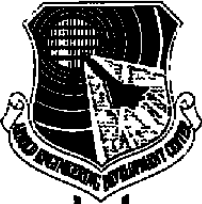


AEDC-TR-92-4



Transonic Flow Calculations for a Cavity with and without a Store

N. E. Suhs
Calspan Corporation/AEDC Operations

September 1992

Final Report for Period October 1988 through January 1992

Approved for public release; distribution is unlimited.

**ARNOLD ENGINEERING DEVELOPMENT CENTER
ARNOLD AIR FORCE BASE, TENNESSEE
AIR FORCE MATERIEL COMMAND
UNITED STATES AIR FORCE**

NOTICES

When U. S. Government drawings, specifications, or other data are used for any purpose other than a definitely related Government procurement operation, the Government thereby incurs no responsibility nor any obligation whatsoever, and the fact that the Government may have formulated, furnished, or in any way supplied the said drawings, specifications, or other data, is not to be regarded by implication or otherwise, or in any manner licensing the holder or any other person or corporation, or conveying any rights or permission to manufacture, use, or sell any patented invention that may in any way be related thereto.


Qualified users may obtain copies of this report from the Defense Technical Information Center.

References to named commercial products in this report are not to be considered in any sense as an endorsement of the product by the United States Air Force or the Government.

This report has been reviewed by the Office of Public Affairs (PA) and is releasable to the National Technical Information Service (NTIS). At NTIS, it will be available to the general public, including foreign nations.

APPROVAL STATEMENT

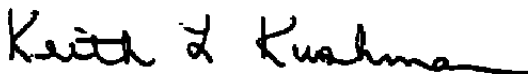
This report has been reviewed and approved.



PAUL LACASSE, Capt, CF
Propulsion Division
Directorate of Technology
Deputy for Operations

Approved for publication:

FOR THE COMMANDER



KEITH L. KUSHMAN
Director of Technology
Deputy for Operations

REPORT DOCUMENTATION PAGE			<i>Form Approved</i> OMB No. 0704-0188		
Public reporting burden for this collection of information is estimated to average 1 hour per response, including the time for reviewing instructions, searching existing data sources, gathering and maintaining the data needed, and completing and reviewing the collection of information. Send comments regarding this burden estimate or any other aspect of this collection of information, including suggestions for reducing this burden, to Washington Headquarters Services, Directorate for Information Operations and Reports, 1215 Jefferson Davis Highway, Suite 1204, Arlington, VA 22202-4302, and to the Office of Management and Budget, Paperwork Reduction Project (0704-0188), Washington, DC 20503					
1. AGENCY USE ONLY (Leave blank)	2. REPORT DATE September 1992	3. REPORT TYPE AND DATES COVERED Final - Oct. 1988 - Jan. 1992			
4. TITLE AND SUBTITLE Transonic Flow Calculations for a Cavity with and without a Store			5. FUNDING NUMBERS PN - 62602F		
6. AUTHOR(S) Suhs, N. E., Calspan Corporation/AEDC Operations					
7. PERFORMING ORGANIZATION NAME(S) AND ADDRESS(ES) Arnold Engineering Development Center/DOT Air Force Materiel Command Arnold Air Force Base, TN 37389-5000			8. PERFORMING ORGANIZATION REPORT NUMBER AEDC-TR-92-4		
9. SPONSORING/MONITORING AGENCY NAME(S) AND ADDRESS(ES) Arnold Engineering Development Center/DOT Air Force Materiel Command Arnold Air Force Base, TN 37389-5000			10. SPONSORING/MONITORING AGENCY REPORT NUMBER		
11. SUPPLEMENTARY NOTES Available in Defense Technical Information Center (DTIC).					
12a. DISTRIBUTION/AVAILABILITY STATEMENT Approved for public release; distribution is unlimited.			12b. DISTRIBUTION CODE		
13. ABSTRACT (Maximum 200 words) A computational fluid dynamics capability has been developed to support weapons bay (cavity) and internal store separation testing. Specifically, a computational capability that can be used to improve the ability to predict store trajectories and strut or sting interference was targeted by this effort. The chimera embedded grid scheme, a domain decomposition technique, was used to divide the cavity, store, and support hardware into simpler overlapping regions for which grids were more easily generated. The flow field was solved using an implicit Navier-Stokes code based on the Pulliam-Steger algorithm with thin-layer approximations to the viscous terms. Unsteady flow calculations were made for an empty cavity at Mach numbers of 0.60, 0.95, and 1.20 for a cavity length-to-height ratio of 4.5. Computations were also made for an ogive-cylinder-ogive store supported by a sting and positioned both in a free-stream flow and in the plane of the cavity opening at Mach numbers of 0.60, 0.95, and 1.20. Additional flow-field computations were made for the store supported by the sting at other positions within and outside the cavity at a Mach number of 1.20. Comparisons of the computations with experimental data were made for the time-averaged and fluctuating static pressures along the walls of the cavity for all of the above calculations. Comparisons were also made for the computed and measured time-averaged static pressures located axially along two opposing sides of the store. The evaluation of sting interference was achieved by removing the sting grid, calculating the flow field for this new configuration, and assessing differences between the store pressures and loads with and without the sting. Calculations for the store without the sting were made at Mach numbers of 0.60, 0.95, and 1.20 in a free-stream flow and with the store positioned in the plane of the cavity opening.					
14. SUBJECT TERMS computational fluid dynamics cavity flow weapons bay			15. NUMBER OF PAGES 130		
			16. PRICE CODE		
17. SECURITY CLASSIFICATION OF REPORT UNCLASSIFIED			18. SECURITY CLASSIFICATION OF THIS PAGE UNCLASSIFIED	19. SECURITY CLASSIFICATION OF ABSTRACT UNCLASSIFIED	20. LIMITATION OF ABSTRACT SAME AS REPORT

PREFACE

The work reported here was done at the Arnold Engineering Development Center (AEDC), Air Force Systems Command (AFSC), at the request of the AEDC Directorate of Technology (AEDC/DOT). The work was accomplished by Calspan Corporation, AEDC Operations, support contractor for the Aerospace Flight Dynamics test facilities at AEDC, AFMC, Arnold Air Force Base, TN, under AEDC Project Number DC72PW. The Air Force Project Manager was Captain (CF) J. E. P. Lacasse, AEDC/DOTP. Work was accomplished during the period October 1, 1988 through January 31, 1992, and the manuscript was submitted for publication on July 19, 1992.

The author acknowledges the contributions of J. C. Erickson, Jr. and R. E. Dix for their many useful suggestions during the conduct of this work.

CONTENTS

	<u>Page</u>
1.0 INTRODUCTION	7
2.0 EXPERIMENTAL DATA DESCRIPTION	9
2.1 Models and Instrumentation	10
2.2 Experimental Data	10
3.0 NUMERICAL PROCEDURE	11
3.1 Chimera Methodology	11
3.2 Accuracy and Numerical Stability	11
3.3 Grids	13
3.4 Initial/Boundary Conditions	14
3.5 Computational Data Analysis Techniques	16
4.0 RESULTS AND ANALYSIS	17
4.1 Empty Cavity	17
4.2 Store/Sting in a Free-Stream Flow	19
4.3 Store/Sting in the Cavity	20
4.4 Sting Interference	24
5.0 CONCLUSIONS	26
REFERENCES	27

ILLUSTRATIONS

<u>Figure</u>	<u>Page</u>
1. Flow in a Cavity	31
2. Photograph of WICS Models Installed in Tunnel 4T	32
3. Dimensions of the WICS Flat-Plate/Cavity Model	33
4. Store Mounted on the Bent Sting	34
5. Experimental Data Samples along the Centerline of the Empty Cavity Walls	35
6. Computational Regions for Two-Grid Cavity Configuration	37
7. Symmetry Plane Grids of Two-Grid Empty Cavity Configuration	38
8. Symmetry Plane Grids of the Store/Sting and Store Alone	39
9. Symmetry Plane Grids of the Free-Stream Configuration with the Store/Sting and Store Alone	40
10. Computational Regions for the Five-Grid Cavity Configuration	41

<u>Figure</u>	<u>Page</u>
11. Symmetry Plane Grids of the Cavity Configuration with the Store/Sting and Store Alone	42
12. Diagram of the Surfaces Requiring Boundary Conditions	43
13. Comparisons of Computations and Measurements on the Empty Cavity Walls, $M_\infty = 0.60$	44
14. Comparisons of Computations and Measurements on the Empty Cavity Walls, $M_\infty = 0.95$	49
15. Comparisons of Computations and Measurements on the Empty Cavity Walls, $M_\infty = 1.20$	50
16. Mach Number Contours in the Symmetry Plane of the Empty Cavity, $M_\infty = 0.60$	51
17. Velocity Vectors in the Symmetry Plane of the Empty Cavity, $M_\infty = 0.60$	57
18. Velocity Vectors in Cross Flow Planes of the Empty Cavity, $M_\infty = 0.60$	58
19. Mass Flow through the Opening of the Empty Cavity, $M_\infty = 0.60$	61
20. Mach Number Contours in the Symmetry Plane of the Empty Cavity, $M_\infty = 0.95$	63
21. Mach Number Contours in the Symmetry Plane of the Empty Cavity, $M_\infty = 1.20$	69
22. Comparisons of Computations and Measurements on the Store/Sting in a Free-Stream Flow, $M_\infty = 0.60$	75
23. Comparisons of Computations and Measurements on the Store/Sting in a Free-Stream Flow, $M_\infty = 0.95$	77
24. Comparisons of Computations and Measurements on the Store/Sting in a Free-Stream Flow, $M_\infty = 1.20$	79
25. Store/Sting Locations within the Cavity	81
26. Comparisons of Computations and Measurements on the Cavity Walls with the Store/Sting Present, $M_\infty = 0.60$, $Z_s/H = 0$	82
27. Comparisons of Computations and Measurements on the Store/Sting in the Cavity, $M_\infty = 0.60$, $Z_s/H = 0$	83
28. Comparisons of Computations and Measurements on the Cavity Walls with the Store/Sting Present, $M_\infty = 0.95$, $Z_s/H = 0$	85
29. Comparisons of Computations and Measurements on the Store/Sting in the Cavity, $M_\infty = 0.95$, $Z_s/H = 0$	86

<u>Figure</u>	<u>Page</u>
30. Comparisons of Computations and Measurements on the Cavity Walls with the Store/Sting Present, $M_\infty = 1.20$, $Z_s/H = 0$	88
31. Comparisons of Computations and Measurements on the Store/Sting in the Cavity, $M_\infty = 1.20$, $Z_s/H = 0$	89
32. Comparisons of Computations and Measurements on the Cavity Walls with the Store/Sting Present, $M_\infty = 1.20$, $Z_s/H = 0.75$	91
33. Comparisons of Computations and Measurements on the Store/Sting in the Cavity, $M_\infty = 1.20$, $Z_s/H = 0.75$	92
34. Comparisons of Computations and Measurements on the Cavity Walls with the Store/Sting Present, $M_\infty = 1.20$, $Z_s/H = -0.30$	94
35. Comparisons of Computations and Measurements on the Store/Sting in the Cavity, $M_\infty = 1.20$, $Z_s/H = -0.30$	95
36. Mach Number Contours in the Symmetry Plane of the Cavity with the Store/Sting, $M_\infty = 1.20$, $Z_s/H = 0.75$	97
37. Mach Number Contours in the Symmetry Plane of the Cavity with the Store/Sting, $M_\infty = 1.20$, $Z_s/H = 0$	103
38. Mach Number Contours in the Symmetry Plane of the Cavity with the Store/Sting, $M_\infty = 1.20$, $Z_s/H = -0.30$	109
39. Mass Flow through the Opening of the Cavity with the Store/Sting, $M_\infty = 0.60$, $Z_s/H = 0$	115
40. Comparisons of Computations for the Store/Sting and Store Alone in a Free-Stream Flow, $M_\infty = 0.60$	116
41. Comparisons of Computations for the Store/Sting and Store Alone in a Free-Stream Flow, $M_\infty = 0.95$	117
42. Comparisons of Computations for the Store/Sting and Store Alone in a Free-Stream Flow, $M_\infty = 1.20$	118
43. Comparisons of Computations for the Store/Sting and Store Alone in the Cavity, $M_\infty = 0.60$, $Z_s/H = 0$	119
44. Comparisons of Computations for the Store/Sting and Store Alone in the Cavity, $M_\infty = 0.95$, $Z_s/H = 0$	120
45. Comparisons of Computations for the Store/Sting and Store Alone in the Cavity, $M_\infty = 1.20$, $Z_s/H = 0$	121
46. Time History of Loads for the Store/Sting in the Cavity, $M_\infty = 0.60$, $Z_s/H = 0$	122
47. Time History of Loads for the Store Alone in the Cavity, $M_\infty = 0.60$, $Z_s/H = 0$	123

TABLES

	<u>Page</u>
1. Load Comparisons for the Store/Sting and Store Alone in the Free-Stream Flow	124
2. Load Comparisons for the Store/Sting and Store Alone in the Cavity, $Z_s/H = 0$	124
 NOMENCLATURE	 125

1.0 INTRODUCTION

Wind tunnel testing and analysis of three-dimensional cavity (weapons bay) configurations to evaluate the internal separation of stores and to define the acoustic environment are continuing activities at the Arnold Engineering Development Center (AEDC) (Refs. 1-2). A complementary computational fluid dynamics (CFD) approach to the testing programs also is under investigation at the AEDC and is the subject of this report. The primary objective of the current CFD effort is to develop capabilities for computational support of internal store separation testing. Specifically, computational capabilities to predict store trajectories and strut or sting interference are targeted by this effort. This computational capability can also be applied to the evaluation of the acoustic environment of the weapons bay, although it was not within the scope of this effort. The first step in the investigation, the computation of unsteady flow in an empty three-dimensional cavity, is documented in Ref. 3. Additional results for an empty weapons bay are presented here to demonstrate improvements in the computational techniques made since Ref. 3 was published. Furthermore, a different weapons bay geometry is considered in the current work. The second step is the computation of the flow field in a weapons bay with a store that is both unsupported and supported by a sting.

There are three methodologies that can be considered as possible approaches to estimate the trajectory of a store computationally. Two of these methods require the coupling of CFD calculations with existing AEDC trajectory prediction codes (Ref. 4). These two methods are similar, in principle, to the methods used to obtain trajectory predictions using wind tunnel data. The first of these methodologies requires a single CFD calculation for a clean weapons bay configuration (without stores). The resulting local flow angles and Mach numbers are used with the Flow-Angle Trajectory Generation Program (Ref. 4) to produce trajectory predictions. Wind tunnel probe data of local flow angularity and Mach number are used in a similar manner in the corresponding test procedure. This approach allows parametric studies of a variety of stores to be performed easily, although mutual interference between the store and aircraft (including the weapons bay) is not included. To include mutual interference, the second methodology calls for a number of CFD solutions to be performed with the store at different locations and orientations, within and about the weapons bay, producing store grid data in a manner identical to store grid data obtained from tests in a wind tunnel. The computed store grid data would then be used with the Multi-Dimensional Interpolation Trajectory Generation Program (Ref. 4) to obtain store trajectory predictions. The third method is a complete CFD prediction in which calculated loads on the store are used to determine the movement of the store throughout its trajectory. This method uses a moving computational grid scheme (Refs. 5-7) and requires a time-accurate calculation.

To further enhance internal store separation testing, the interference that a strut or sting has on store loads must be assessed. Strut or sting interference can be obtained by modeling

a store with and without its support hardware. The differences between the two calculations provide a measure of the interference caused by the strut or sting (Ref. 8).

Cavity flow is an unsteady phenomenon with large velocity and pressure fluctuations inside the cavity (Refs. 9-12). Cavity flow can be categorized into three types: open, closed, and transitional (Ref. 13). For all of these cavity flow types, the flow is driven by the external stream. A boundary layer develops over the body upstream of the cavity, separates from the leading edge of the cavity, and becomes a free shear layer. The shear layer typically oscillates in and out of the cavity, developing a highly vortical flow in the cavity. As shown in Fig. 1a, for open cavity flow (length-to-height (L/H) ratio less than about 9), the shear layer spans the cavity and stagnates on the aft wall. For closed cavity flow (L/H greater than about 13) the flow attaches to the bottom wall of the cavity as shown in Fig. 1b. Cavities with an L/H between about 9 and 13 are considered to be transitional, where either type of flow may occur. These L/H ranges for open, closed, and transitional cavities are not precise and are used only as a general guideline in categorizing cavity flow.

Experimentally, studies have also been performed with stores placed within the weapons bay. Recent studies at AEDC (Refs. 1-2) and at NASA Langley (Ref. 14) have investigated the loads and trajectories of stores within a weapons bay for subsonic through supersonic Mach numbers. For a survey of the experimental studies done at supersonic speeds, see Ref. 15.

Several numerical studies which solve the Navier-Stokes equations for two- and three-dimensional cavity flows have been made over the past several years. The two-dimensional computations will be discussed first. Hankey and Shang (Ref. 16) performed computations for a rectangular cavity (L/H = 2.3) at a free-stream Mach number (M_∞) of 1.5. These results were compared with experimental static pressure measurements represented as pressure coefficients and sound pressure levels. Baysal and Stallings (Ref. 17) performed calculations for a range (L/H = 6, 12, and 16) of cavities at $M_\infty = 1.5$ and compared the computations to measured static pressure data. Computations of midplane flow in and around an airborne telescope cavity at $M_\infty = 0.8$ were performed by Venkatapathy, et al. (Ref. 18) with comparisons to experimental measurements of the streamwise velocity component, total pressure, mass flux, and Mach number. Dougherty, et al. (Ref. 19) computed the flow for a cavity (L/H = 2) at $M_\infty = 0.6, 0.8,$ and 1.2 , concentrating on the acoustic environment in the cavity.

Extensive three-dimensional computations also have been made. Computations were performed by Gorski, et al. (Ref. 20) for a simplified version of an F-111 weapons bay at $M_\infty = 2.36$, although no comparisons with data were made. Suhs (Ref. 3) performed computations for cavities (L/H = 5.6) at $M_\infty = 0.74$ and 1.5 with comparisons to static pressure data represented as pressure coefficients and sound pressure levels. Other numerical

cavity studies include the work of Rizzetta (Ref. 21) and Baysal, et al. (Refs. 22-23). Rizzetta's calculations (Ref. 21) were for a cavity ($L/H = 5.0$) at $M_\infty = 1.5$ and include a comparison to static pressure data as well as the frequency spectrum of the fluctuating pressures in the cavity. The Baysal, et al. (Ref. 22) calculations were for cavities ($L/H = 6$ and 16) at $M_\infty = 1.5$, and the results were compared with time-averaged static pressure data. The transonic solutions presented by Baysal, et al. (Ref. 23) for $M_\infty = 0.58$ ($L/H = 11.7$) and $M_\infty = 0.9$ ($L/H = 4.4$) are compared with time-averaged static pressure data. The comparisons of the computations with the experimental data for the preceding numerical studies typically showed good agreement for the supersonic Mach number computations and poorer agreement for the subsonic and transonic Mach number computations.

Computations for a store mounted on a support in a three-dimensional cavity have been made by Baysal, et al. (Ref. 24) for supersonic flow at $M_\infty = 1.65$ and 2.75 . The agreement between the computations and the experimental static pressure data within the cavity was good, and the agreement for the store loads was mixed.

The approach of using the complete Navier-Stokes formulation was followed in all of the above numerical studies (Refs. 16-24), with the exception of the study by Suhs (Ref. 3), which uses the thin-layer approximation to the viscous terms in one direction. All of the studies used some form of an eddy viscosity model to simulate turbulence.

The computations presented in this report demonstrate the ability to compute the flow in a three-dimensional cavity at transonic Mach numbers using the thin-layer approximation to the viscous terms, which is a less computationally intensive approach. Comparisons with data include static pressure orifice data and differential pressure transducer data for locations on the cavity walls as well as on the store. A description of the experimental data is presented in Section 2.0. The numerical procedure used to perform computations is described in Section 3.0. Comparisons of the computations with the experimental data, as well as analysis of these results, are presented in Section 4.0, with conclusions and recommendations in Section 5.0.

2.0 EXPERIMENTAL DATA DESCRIPTION

Data used for comparisons were acquired during the Weapons Internal Carriage Separation Program (WICS), which was sponsored by the Air Force Armament Laboratory (AFATL) to establish a database for internal carriage and release of stores (Refs. 1-2). The basic configuration tested was a generic flat plate and cavity with a store mounted on a bent sting (Fig. 2). For convenience the store/sting combination will be referred to as the store/sting while the store without the sting will be referred to as the store alone. The store/sting was placed at various locations within and about the flat plate and cavity configuration. Measurements were taken at Mach numbers from 0.6 to 5.0 in AEDC Aerodynamic Wind Tunnel 4T and Supersonic Wind Tunnel A.

2.1 MODELS AND INSTRUMENTATION

The generic flat plate and cavity model, as well as typical instrumentation locations, are shown in Fig. 3. The store shown in Fig. 4 is an ogive-cylinder-ogive without fins and is mounted on a bent sting. The sting is connected to the wind tunnel captive trajectory system (CTS) which controls the movement and positioning of the store (Ref. 1). Particularly note the store free-stream side and cavity side, since these designations will be used in the discussions in the following sections.

Two basic types of instrumentation, static pressure orifices [connected to Electronically Scanned Pressure (ESP) modules] and flush-mounted differential pressure transducers, were installed on the flat plate, cavity, and store (Refs. 1-2). The generic cavity configuration is equipped with 95 static pressure orifices and 33 differential pressure transducers. The store is instrumented with 38 static pressure orifices and 6 differential pressure transducers.

2.2 EXPERIMENTAL DATA

When the experimental data are compared with computations, it is important to consider the methods used in processing the signal received and recorded by each instrument type. The methods used are discussed to allow an objective interpretation of the comparisons of the experimental data with the unsteady flow computations.

2.2.1 Static Pressure Orifices

Each static pressure orifice is sampled 15 times per sec (once every 66 msec). The most recent 15 values are averaged to give the recorded value of pressure at each location following standard steady-state-flow ESP sampling techniques. With such a coarse sample of a rapidly varying flow, it is not surprising that repeat static pressure coefficient (C_p) orifice measurements using steady-state techniques show variations in magnitude greater than the typical uncertainty ($+0.01$ in C_p) for steady flow. Such measurements, expressed as C_p^e , are shown in Fig. 5 for the centerlines of the front, bottom, and aft walls of an empty cavity for 13 samples at $M_\infty = 0.60$ and 5 samples at $M_\infty = 0.95$ and 1.20. These variations in C_p^e are large in the subsonic and transonic Mach number range but are not as pronounced in the supersonic Mach number range. The same wide variation in C_p^e from repeat measurements, using standard steady-state ESP sampling techniques, was also observed for subsonic and transonic flow by Plentovich (Ref. 25). Clearly, the wide variations observed must be taken into account when they are compared to the computed results.

2.2.2 Differential Pressure Transducers

The differential pressure transducers measure the difference between the pressure acting on the transducer surface and a reference pressure. For all differential pressure data, the reference pressure was the static pressure in the instrumentation housing of the flat plate and cavity (Fig. 3), which was essentially free-stream static pressure. The differential pressure measurements were recorded at a rate of 10,000 samples/sec and analyzed using fast Fourier transform techniques to obtain power spectral density distributions for each sensor location. For comparison to computational results, the overall sound pressure level (SPL) at each sensor location was used.

3.0 NUMERICAL PROCEDURE

3.1 CHIMERA METHODOLOGY

Several factors were taken into account in determining the numerical approach to use in the present study. First, cavity flow has been shown experimentally to be unsteady; hence, the numerical flow solver must be time accurate. Second, the shear layer that crosses the cavity opening should be spatially resolved. Finally, cavity flow problems become even more complex with the addition of doors, acoustic suppression devices (fences, rakes, vortex generators), and stores. Domain decomposition is a convenient methodology for treating these complex configurations. Thus, the chimera embedded grid scheme (Refs. 26-28) was chosen as the numerical approach for solving three-dimensional cavity flow.

The chimera scheme allows the computational domain to be divided into simpler overlapping regions for which grids are more easily constructed. The chimera scheme is composed of two codes. The first, PEGSUS (Ref. 28), takes individually generated grids as input and defines the communication and interpolation data among interacting grids. The second, XMERGA, takes as input the composite grid and interpolation data created by PEGSUS and calculates the flow field. XMERGA is a 3-D implicit Navier-Stokes code based on the Pulliam-Steger algorithm (Ref. 29) with a thin-layer approximation to the viscous terms in one direction (normal to the flat plate and the bottom wall of the cavity, Fig. 1). The algorithm is first-order accurate in time and uses the Baldwin-Lomax turbulence model (Ref. 30). The turbulence model is used only on the flat plate and not within the cavity.

3.2 ACCURACY AND NUMERICAL STABILITY

The flow in a cavity is unsteady and requires the computation to have sufficient temporal (time step) as well as spatial (grid spacing) resolution to accurately define the flow. Specifically, the time step must be small enough to resolve the frequencies observed in the cavity, while

the grid must resolve the shear layers on the cavity walls and stores. Both the time step and grid spacing play an important role in the numerical stability of the solution.

Numerical stability considerations can be illustrated by considering an explicit solution algorithm. The relationship for the maximum allowable time step for numerical stability of a compressible inviscid flow (Ref. 31) is given by:

$$\Delta t_i < \{(|u|/\Delta X) + (|v|/\Delta Y) + (|w|/\Delta Z) + a [(1/\Delta X^2) + (1/\Delta Y^2) + (1/\Delta Z^2)]^{0.5}\}^{-1} \quad (1)$$

When compressible viscous flow is considered, the following modification (Ref. 31) is required:

$$\Delta t_v < \Delta t_i / (1 + 2/R_{e\Delta}) \quad (2)$$

where:

$$R_{e\Delta} = \min (R_{e\Delta x}, R_{e\Delta y}, R_{e\Delta z})$$

$$R_{e\Delta x} = \rho |u| \Delta X / \mu$$

$$R_{e\Delta y} = \rho |v| \Delta Y / \mu$$

$$R_{e\Delta z} = \rho |w| \Delta Z / \mu$$

From Eq. (2), as

$$u, v \text{ or } w \rightarrow 0, \text{ or } \Delta X, \Delta Y \text{ or } \Delta Z \rightarrow 0, \text{ then } R_{e\Delta} \rightarrow 0 \text{ and } \Delta t_v \rightarrow 0.$$

Also note that as

$$R_{e\Delta} \rightarrow \infty, \text{ then } \Delta t_v \rightarrow \Delta t_i \text{ as expected.}$$

Based on these relationships and the fact that the time step required to resolve the physically significant frequencies of the flow (Δt_f) is much greater than either numerical time step restriction, the following relationship is obtained:

$$\Delta t_v < \Delta t_i < \Delta t_f$$

Hence, Δt_v determines the maximum time step allowed.

The accuracy and numerical stability must be balanced with the computer time required to obtain a solution. In the cavity, the velocity components u , v , and w approach zero for an appreciable distance from the corners. The minimum grid spacing for viscous flow is chosen to resolve the laminar sublayer of the boundary layer on the solid surfaces. A balance between accuracy and cost was achieved by increasing the grid spacing near the cavity walls, thereby allowing the time step for numerical stability to be increased. The minimum grid spacing used in the current work was smaller by a factor of 2 to 5 than that used in other computations (Refs. 21-22) that utilized full Navier-Stokes flow solvers.

3.3 GRIDS

The grids for computing the flow field were generated to obtain good resolution for regions with high flow gradients and sized to fit in the available computer memory of the AEDC Cray X-MP/12. Fifteen different meshes were developed and combined into eight configurations required for the computations. To decrease the computational time required for each solution, the domain was reduced by one-half by assuming a lateral plane of symmetry. Representative trial computations for the entire domain showed that the flow in an empty cavity had this symmetry.

3.3.1 Empty Cavity Grids

For the computations of the flow in an empty cavity, two grids were generated. One grid defined the cavity and a small region above the cavity opening, and the other grid defined the region above the plate (see Fig. 6). Each region was discretized with a stretched Cartesian grid. The points were clustered near walls and in the vicinity of the shear layer. The symmetry plane is shown in Fig. 7.

Both exponential and hyperbolic tangent stretching functions (Ref. 32) were used to cluster the points. The exponential stretching function was used for placing points where a specific spacing is needed at only one end point, e.g., from the flat plate to the far-field boundary. The hyperbolic tangent stretching function was used when a specific spacing was needed at both ends of a line, e.g., from the front wall to the aft wall and from the bottom wall to the opening of the cavity.

One difficulty with using the hyperbolic tangent stretching function is that the values which are calculated for the spacing at each end of a line are not equal to the values which were initially specified. These values can differ by 10 percent or more. To ensure that the specified spacing is obtained, an iterative correction procedure was developed.

3.3.2 Store/Sting and Store-Alone Grids

The store and sting are represented with separate body-conforming grids. The store and sting grids were generated separately to allow for the removal of the sting, and therefore, to obtain solutions for the store without the sting. The grid points on the body and symmetry plane surfaces were obtained by using both exponential and hyperbolic tangent stretching functions. The interior mesh points were obtained by using transfinite interpolation (Ref. 33). The symmetry plane of the store and sting grids is shown in Fig. 8a. When a store-alone solution was required, the sting grid was omitted and replaced with one which closed the aft end of the store (see Fig. 8b).

3.3.3 Free-Stream Grids with the Store/Sting and the Store Alone

The grids used for the free-stream calculations of the store/sting and store alone are all stretched Cartesian grids. Shown in Fig. 9 is the symmetry plane for the free-stream grids used for both the store/sting and the store-alone computations. Points interior to the store and sting are excluded from the grids because they are not part of the solution when the store/sting (Fig. 9a) or the store-alone grids (Fig. 9b) are present. The chimera scheme provides the proper communication among the free-stream and the store/sting or store-alone grids. Also note the grids that have been embedded around the store and sting to increase the overlap among the grids.

3.3.4 Cavity Grids with Store/Sting and Store Alone

Two grids are used to define the region above the plate and three grids to define the cavity and a small region above the cavity opening (see Fig. 10). The reason for the increased number of grid points in the cavity with the store present was the need to have sufficient overlap when embedding the store, sting, and store cap grids. In Fig. 11a, the symmetry plane of the flat plate and cavity grids is shown with the store/sting embedded. Shown in Fig. 11b are the same symmetry plane grids, but with the store alone embedded. As was the case for the free-stream grids in Fig. 9, the points excluded from the grids are points that are not part of the solution because of the embedded store/sting (Fig. 11a) or store-alone grids (Fig. 11b).

3.4 INITIAL/BOUNDARY CONDITIONS

Figure 12 illustrates the location of each of the surfaces on which boundary conditions are specified. The conditions are as described below. The $Y = 0$ plane is the plane of symmetry and the side plane coincides with the side edge of the flat plate.

3.4.1 Inflow Surface

Two approaches were used to define the boundary conditions on the inflow surface. One was to locate the inflow plane about one cavity length upstream of the flat plate leading edge and allow the boundary layer to develop along the plate. All points on the inflow surface (see Fig. 12) were set to free-stream conditions. This approach was used in the preliminary work on cavity flow calculations (Ref. 3) and was used in the present computations at $M_\infty = 0.60$ and 0.95 . The other approach located the inflow plane 1.0 cavity depths upstream of the leading edge of the cavity, with the inflow velocity profile set to that of a turbulent boundary layer corresponding to that location. The velocity profile was computed based on the 1/7th-power law, and the density and energy terms were computed from the X-distribution of the experimental static pressure with an assumed zero normal pressure gradient through the boundary layer. This approach was used for the cases with $M_\infty = 1.20$.

3.4.2 Solid Wall Surfaces

The no-slip condition was imposed on the solid surfaces of the plate and cavity. This is the correct condition for the cavity bottom wall and for the flat plate since the thin-layer viscous terms are included normal to these surfaces. For the cavity front, aft, and side walls, the no-slip condition was used as a matter of convenience to avoid double-valued points at the edges and corners. It was felt that the use of the no-slip conditions (as opposed to the normally used inviscid slip conditions) was justified because a computation with thin-layer approximations for all surfaces showed no significant changes in the computed flow.

Inviscid slip conditions were imposed on the solid surfaces of the store and sting. This condition was used to keep the run time to a minimum for these calculations (i.e., if the no-slip condition were used and the viscous terms were resolved near these surfaces, finer grid spacing would be required which would greatly increase the run time). A test case, with the viscous terms and no-slip conditions imposed on the store and sting, showed only small changes in the results from those with the slip boundary conditions.

3.4.3 Side and Symmetry-Plane Surfaces

Symmetry conditions were enforced on the side surface (see Fig. 12) of the grids exterior to the cavity and on the symmetry plane of the cavity.

3.4.4 Upper Surface

The boundary conditions for the upper surface (see Fig. 12) were set to free-stream conditions, except for the value of the Z-component of momentum, which was evaluated by zeroth-order extrapolation.

3.4.5 Downstream Surface

The conditions on the downstream outflow surface (see Fig. 12) depended on whether the local flow was subsonic or supersonic. If the flow was subsonic, all flow variables except the energy were set by zeroth-order extrapolation. The energy was calculated assuming free-stream pressure and the extrapolated values. If the flow was supersonic, all values, including energy, were set by zeroth-order extrapolation.

3.4.6 Initial Conditions

The flow velocity in the cavity was set to zero. A linear velocity distribution from zero to the free-stream value was imposed on the 10 planes ($-0.025 < Z/H < 0$) adjacent to the flat plate for the flow at $M_\infty = 0.60$ and 0.95 . The remainder of the grid was set to the free-stream value. For the flow at $M_\infty = 1.20$, where a boundary-layer profile was prescribed at the inflow surface, this profile was used as the initial condition across the entire exterior grid. It was found that the thickness of the initial boundary layer should be as realistic as possible since an inaccurate distribution could have a profound effect on the decay of the initial condition transients. Particularly, if the boundary-layer thickness is initialized too large, the computation would require significant additional time steps before the starting transients disappear.

3.5 COMPUTATIONAL DATA ANALYSIS TECHNIQUES

Calculations of C_p and sound pressure level (SPL) are compared to experimental data. Since cavity flow is unsteady, the SPL and the time-averaged pressure coefficient (\bar{C}_p) are obtained by integrating over a time interval (T_{avg}) long enough to ensure that \bar{C}_p is no longer changing if the time interval is increased from T_{avg} . From experience, T_{avg} was determined to be a minimum of $6t_c$, where the characteristic time, t_c , is the time required for the flow to traverse the length of the cavity at the free-stream velocity. At $M_\infty = 0.60$, 0.95 , and 1.20 , t_c is 0.00225 , 0.00149 , and 0.00123 sec, respectively, based on the test conditions. To ensure that the starting transients have decayed, solutions are calculated over $5t_c$ prior to beginning the T_{avg} interval used in the determination of \bar{C}_p and SPL. The SPL in decibels (dB) is defined as:

$$\text{SPL(dB)} = 180 + 20 \log[P_{rms}/P_{ref}] \quad (3)$$

where P_{rms} is the root-mean-square of the pressure fluctuations about the average in pounds per square inch (psi) and P_{ref} is equal to 2.90075 psi (a standard reference pressure).

4.0 RESULTS AND ANALYSIS

This section addresses the accuracy of the computations by comparison with experimental data, represents the computed flow by numerical visualization techniques, and analyzes the interference that the sting support has on the store. First, in Section 4.1 results of the computations for the empty cavity ($L/H = 4.5$) are presented. The computations for the store/sting in a free-stream flow and in the cavity are presented in Sections 4.2 and 4.3. Finally, the computations for evaluating the sting interference are presented in Section 4.4.

4.1 EMPTY CAVITY

Computations were performed for the empty cavity at $M_\infty = 0.60, 0.95,$ and 1.20 . Comparisons of these results to experimental data are given in Section 4.1.1. Selected graphical representations for these computations are presented in Section 4.1.2.

4.1.1 Data Comparisons

Comparisons of computations to experimental data for an empty cavity at $M_\infty = 0.60, 0.95,$ and 1.20 are given for C_p and SPL. Extensive comparisons are given for the empty cavity at $M_\infty = 0.60$. Of special note are the comparisons for C_p along the centerlines of the front, bottom, and aft walls, *lateral variations along the bottom wall*, and *vertical variations along the side walls*. At $M_\infty = 0.95$ and 1.20 , comparisons are made only for the centerlines of the front, bottom, and aft walls, since the trends observed in the lateral and vertical variations are similar to those at $M_\infty = 0.60$. For all Mach numbers, the comparisons of computations to experimental data for SPL are shown only for the centerlines of the front, bottom, and aft walls of the cavity.

For the comparisons of computations with experimental data, the experimental values of C_p^e , such as those from Fig. 5, are illustrated along with the calculated values of C_p . The calculated results are represented by \bar{C}_p (solid line) and the sum of \bar{C}_p plus/minus the standard deviation of the time history of the calculated pressure coefficients about \bar{C}_p (\bar{C}_p^s , dashed lines). \bar{C}_p^s is shown because it displays the variations that are present in the calculations with respect to the variations of the measurements.

4.1.1.1 $M_\infty = 0.60$

Given in Fig. 13 are the comparisons of the computations to the experimental data for the empty cavity at $M_\infty = 0.60$. Shown in Fig. 13a are the C_p distributions along the centerlines of the front, bottom, and aft walls of the cavity. The spread of experimental data

is bounded by the computational results \bar{C}_p^s . On the other hand, as shown in Fig. 13b, the agreement was not as good for the overall SPL, especially for $0.65 < X/L < 1.0$ on the bottom wall of the cavity. In Figs. 13c and 13d are plots of the C_p distributions along the bottom wall for two different spanwise locations. Both of these comparisons display good agreement. The computed \bar{C}_p distributions from Figs. 13a, 13c, and 13d at the three lateral locations are summarized in Fig. 13e. Only small spanwise variations in \bar{C}_p are seen across the cavity bottom wall in Fig. 13e. Shown in Figs. 13f, 13g, and 13h are the C_p comparisons for the side wall at different depths (Z/H) within the cavity. Again, good agreement is seen. The computed \bar{C}_p distributions from Figs. 13f, 13g, and 13h at the three depths are summarized in Fig. 13i. Also, only small variations in \bar{C}_p with Z/H are observed for the computations, as shown in Fig. 13i.

4.1.1.2 $M_\infty = 0.95$

Shown in Fig. 14 are comparisons for an empty cavity at $M_\infty = 0.95$. In Fig. 14a, the C_p distributions along the centerlines of the front, bottom, and aft walls of the cavity are compared. Depicted in Fig. 14b is the comparison of the SPLs with very good agreement apparent between the computations and the experimental data. Both the amplitude and trends are predicted by the computation.

4.1.1.3 $M_\infty = 1.20$

In Fig. 15 comparisons for the empty cavity at $M_\infty = 1.20$ are illustrated. Similar to the results obtained at $M_\infty = 0.95$, the comparisons of computations with experimental data are satisfactory for the pressure coefficients shown in Fig. 15a and for the SPL shown in Fig. 15b.

4.1.2 Graphical Representation of the Computed Flow

Cavity flow is known to be unsteady, but the degree of unsteadiness is typically not appreciated. In Figs. 16-21, the graphical representation of the empty cavity results is illustrated to point out particular features of the flow. In each of these figures, three instants are shown to illustrate the temporal variations. Shown in Fig. 16 are the Mach contours in the plane of symmetry at $M_\infty = 0.60$. Very low-speed flow with small variations occurs in the front region of the cavity, and significant changes occur in the aft region from one instant to the next. Illustrated in Fig. 17 are the velocity vectors in the plane of symmetry at $M_\infty = 0.60$. The direction and magnitude of the velocity clearly change dramatically from one instant to the next, with significant regions of reversed flow evident. For Figs. 18 and 19, the flow field is reflected about the symmetry plane for ease of visualization. In Fig. 18, velocity vectors

are illustrated at three different longitudinal cross sections at $M_\infty = 0.60$. Again, the flow direction clearly changes very rapidly. Depicted in Fig. 19 is the mass flow through the opening of the cavity at $M_\infty = 0.60$. The height of the contours below or above the cavity opening indicates the relative local mass flow into or out of the cavity. The figure demonstrates the three-dimensional nature of the flow as well as the temporal fluctuations. In Figs. 20 and 21, Mach contours in the plane of symmetry are shown for $M_\infty = 0.95$ and 1.20. Again, low-speed flow is noted in the front of the cavity, and higher speed flow with large temporal variations exists in the aft region of the cavity.

The graphical representation gives evidence of the nature of the time- and space-dependent variations in the cavity, especially the large amplitudes in the region aft of the cavity midpoint. It is in this region, and on the aft wall in particular, that both the repeat C_p^e measurements and the computed \bar{C}_p and \bar{C}_p^s results have the greatest variability in the comparisons of Figs. 13a, 14a, and 15a in Section 4.1.1.

4.2 STORE/STING IN A FREE-STREAM FLOW

The computational results for the isolated store/sting configuration in a uniform steady-state free-stream flow are presented to demonstrate the validity of the computational method for this geometry. The time-accurate computations for this configuration converged to a steady-state solution. Comparisons of the computed steady-state C_p distributions with the steady-state experimental data are shown in Figs. 22-24 for $M_\infty = 0.60, 0.95,$ and 1.20. Shown in each figure are the C_p distributions on the free-stream and the cavity sides of the store, as well as the difference in C_p between the two sides. The difference in C_p between the free-stream and cavity sides is defined as

$$\Delta C_p = C_{p,\text{free-stream side}} - C_{p,\text{cavity side}} \quad (4)$$

The ΔC_p distribution along the length of the store is illustrated to give a relative indication of the loads in the Z direction that would be experienced by the store. In this case, non-zero values of ΔC_p arise from the asymmetric sting. For all store results, X/L relates the position of the store in the cavity, where X is the axial distance of a point on the store measured from the front wall of the cavity, and L is the length of the cavity. Thus, the store nose is at $X/L = 0.026$ and the boattail of the store intersects the sting at $X/L = 0.824$. For all three Mach numbers, the comparisons of the computations with the experimental data are very good. The only small disagreement occurs just aft of the store nose at about $X/L = 0.15$ for $M_\infty = 0.95$ and 1.20 where the shock location is in error because of the inviscid flow approximation on the store/sting.

4.3 STORE/STING IN THE CAVITY

Computations were performed for the store/sting in the cavity at $M_\infty = 0.60, 0.95,$ and 1.20 . For all Mach numbers the store was located at $Z_s/H = 0$. Additionally, computations were made with the store located at $Z_s/H = 0.75$ and -0.30 for $M_\infty = 1.20$. Depicted in Fig. 25 are the three locations of the store used for the computations. For all computations the store nose is located at $X/L = 0.026$. Comparisons of these results to experimental data are given in Section 4.3.1. Graphical representation of the flow for these computations is illustrated in Section 4.3.2. The store pressures are discussed in Section 4.3.3.

4.3.1 Data Comparisons

Comparisons of computations to experimental data for the store/sting in the cavity at $Z_s/H = 0$ for $M_\infty = 0.60, 0.95,$ and 1.20 , and at $Z_s/H = 0.75$ and -0.30 for $M_\infty = 1.20$ are given for C_p and SPL. For these comparisons only one value of C_p^e is available at each sensor location, unlike the empty cavity results which have five to thirteen measurements. Comparisons along the centerlines of the front, bottom, and aft walls are made for both C_p and SPL. Since the trends observed in the results for lateral and vertical variations along the bottom and side cavity walls, respectively, were similar to those for the empty cavities, Figs. 13c - 13i, these comparisons are not shown with the store/sting present. Comparisons of computational with experimental C_p distributions on the store are made for the free-stream and cavity sides of the store and the ΔC_p difference [Eq. (4)] between the sides.

4.3.1.1 $M_\infty = 0.60, Z_s/H = 0$

Comparisons of the computations with the experimental data are shown in Fig. 26 for the store/sting in the cavity at $M_\infty = 0.60$ and the store at $Z_s/H = 0$. In Fig. 26a, the C_p distributions along the centerlines of the front, bottom, and aft walls of the cavity are illustrated. The agreement between the computations and the data is reasonable, with the exception of the portion $0.45 < X/L < 0.95$ of the bottom wall. However, the agreement was not good for the overall SPL along the centerlines of all three walls of the cavity (Fig. 26b). This latter trend was also observed for the empty cavity at $M_\infty = 0.60$ (see Fig. 13b), but is more pronounced here.

Comparisons of the computed and measured C_p distributions on the free-stream and cavity sides of the store are shown in Figs. 27a and 27b, respectively. The agreement on the store is unsatisfactory in the aft region of the cavity, similar to what was observed for the cavity wall pressures. To investigate the overall effect that the poor agreement has on computing store loads, ΔC_p is shown in Fig. 27c. The computed ΔC_p distribution gives a relative indication of the store loads in the Z direction. As can be inferred, the loads on the store would be predicted with relatively small errors.

4.3.1.2 $M_\infty = 0.95, Z_s/H = 0$

Comparisons of the computations with experimental data are presented in Fig. 28 for the store/sting in the cavity at $Z_s/H = 0$ for $M_\infty = 0.95$. Shown in Fig. 28a are the C_p distributions along the centerlines of the cavity walls. Similar to the comparisons at $M_\infty = 0.60$ (see Fig. 26a), the agreement is particularly poor in the aft region of the cavity. In Fig. 28b, the comparisons of the SPL are shown. The SPL agrees well with the exception of the region $0.65 < X/L < 0.95$. The C_p comparisons along the free-stream and cavity sides of the store shown in Figs. 29a and 29b disagree everywhere on the store aft of $X/L = 0.1$. This is even worse agreement than at $M_\infty = 0.60$ (see Figs. 27a and 27b). Nevertheless, the ΔC_p distributions shown in Fig. 29c indicate that the loads would be reasonably predicted.

4.3.1.3 $M_\infty = 1.20, Z_s/H = 0$

Comparisons of the computations with experimental data are depicted in Fig. 30 for the store/sting in the cavity at $M_\infty = 1.20$ and the store at $Z_s/H = 0$. Again, similar trends are seen for the comparisons of C_p . In Fig. 30a, the C_p distributions along the centerlines of the cavity walls are shown. The comparisons differ substantially in the aft region of the cavity. The comparisons for the SPL are very good, as shown in Fig. 30b. In Figs. 31a and 31b, the comparisons of C_p distributions are illustrated for the free-stream and cavity sides of the store. Similar to the computations at $M_\infty = 0.60$ (Figs. 27a and 27b), the computed C_p increases along the aft portion of the store and does not compare well to the experimental data. Depicted in Fig. 31c is the ΔC_p distribution for the store. The front portion of the store compares well, and the aft portion shows some divergence from the data. This is similar to what was seen for $M_\infty = 0.60$ (Fig. 27c).

4.3.1.4 $M_\infty = 1.20, Z_s/H = 0.75$

For this case, the store has been placed deep within the cavity at $Z_s/H = 0.75$ (see Fig. 25). The comparisons of the computed and experimental C_p distributions along the centerlines of the front, bottom, and aft walls of the cavity (Fig. 32a) were found to be somewhat less satisfactory than for $Z_s/H = 0$ (Fig. 30a) as the store approaches the bottom of the cavity. However, the computed and experimental SPL (Fig. 32b) compared better than in Fig. 30b. The C_p comparisons along the free-stream and cavity sides of the store (Figs. 33a and 33b) also were unsatisfactory. However, good agreement between the computations and the experimental data for ΔC_p on the store is shown in Fig. 33c.

4.3.1.5 $M_\infty = 1.20$, $Z_s/H = -0.30$

The final case of the interaction between the store/sting and the cavity is with the store located outside of the cavity at $Z_s/H = -0.30$ (see Fig. 25). At this location the store is farther from the influence of the cavity, and there is improved comparison between the computations and the experimental data. In Fig. 34a, the comparisons of C_p distributions along the centerlines of the front, bottom, and aft walls of the cavity are given. Likewise, the SPL is shown in Fig. 34b for the same centerline locations. The comparisons of both C_p and SPL are very good. In Figs. 35a and 35b, the comparisons for C_p along the free-stream and cavity sides of the store are shown and are very good. Finally, the ΔC_p distribution for the store is shown in Fig. 35c. It is unsatisfactory near the nose ($X/L \leq 0.2$), which is in marked contrast to Figs. 31c and 33c. The influence of the cavity on the store is still apparent when the C_p distributions on the store/sting in a free-stream flow (Figs. 24a and 24b) and the results for the store/sting near the cavity (Figs. 35a and 35b) are compared.

4.3.2 Graphical Representation of the Computed Flow

Mach number contours in the plane of symmetry of the store/sting in the cavity at $M_\infty = 1.20$ for $Z_s/H = 0.75$, 0 , and -0.30 , respectively, are shown in Figs. 36-38 at three instants. As in the empty cavity flow field (Fig. 21), large variations in flow are seen between the different instants. These figures clearly illustrate the range of flow velocities that a store must traverse when it is released from a weapons bay.

The Mach number contours in Figs. 36-38 can be related directly to features of the time-averaged pressure distributions on the store/sting. For example, as shown in Fig. 36 at $Z_s/H = 0.75$, the flow near the nose of the store/sting is nearly stagnant. This low-speed flow results in the lack of significant amplitudes of both the measured C_p^e and computed \bar{C}_p distributions in Figs. 33a and 33b on the free-stream and cavity sides of the nose, respectively. The character of the pressure distributions on both sides of the nose in Fig. 33 is in marked contrast to the free-stream distributions for the store/sting at any of the M_∞ in Figs. 22-24. Even more striking are the results at $Z_s/H = 0$. The remarkable feature shown for this case in Fig. 37 is that the free-stream side of the store/sting nose essentially is in a nearly sonic flow, while the cavity side is in a nearly stagnant flow. This is reflected in both the measured C_p^e and computed \bar{C}_p distributions in Figs. 31a and 31b. On the free-stream side, the distribution is characteristic of the free-stream flow over the store/sting in a nearly sonic flow (Figs. 23 and 24), while on the cavity side it is characteristic of the nearly stagnant flow, as in Fig. 33b for $Z_s/H = 0.75$. Finally, as the store/sting exits the cavity to $Z_s/H = -0.30$, the nose is almost entirely in a free-stream flow (see Fig. 38) so that the corresponding \bar{C}_p distributions in Fig. 35 are in excellent agreement near the nose with the free-stream results in Fig. 24.

Finally, Fig. 39 illustrates the mass flow through the opening of the cavity that is realized when the store is at that location ($Z_s/H = 0$) at $M_\infty = 0.60$. See Fig. 19 for the empty cavity equivalent. The overall character of the mass flow has not changed with the presence of the store, except for a local region around the perimeter of the store and sting.

4.3.3 Discussion of Store Pressure Distributions

A few remarks can be offered about the disagreement between the computed and measured C_p distributions on the ogive-cylinder-ogive store when it is within the cavity (see Figs. 27, 29, 31, and 33). This store is a very slender configuration with a constant diameter in the interval of approximately $0.10 < X/L < 0.75$. After correction for sting interference (see Section 4.4.1), the free-stream C_p distributions on the cylindrical portion of this store at zero angle of attack are approximately zero, which is consistent with the results for the two-velocity-component static pipes used in wind tunnel flow-field measurements (Refs. 34-35). The theory of Refs. 34-35 is directly applicable to spatially varying, steady flows incident on a static pipe. Basic results of the theory are, first, that the average of the local C_p measurements on the opposing sides of the pipe are, to first order, equal to the C_p distribution which would exist along the centerline of the pipe if the pipe were not present. The difference of the X-component of the local centerline velocity from its free-stream (Δu) value is related linearly to the centerline C_p . Second, the Z-derivative of Δu at the pipe centerline is proportional to the local difference of the pressure coefficient between the opposing orifices (ΔC_p). If the assumption is made that the temporally varying flow effects on the store are of higher order than the spatially varying effects, then static pipe theory can be used to evaluate the flow in the cavity as though the store were not present. That is, the cylindrical portion of the store can be considered to be a static pipe.

Although the computational and experimental ΔC_p distributions over the cylindrical portions of the store are nearly zero (Figs. 27c, 29c, 31c, 33c, and 35c), there are major differences between the computational and experimental C_p distributions with the store in the cavity (Figs. 27a-b, 29a-b, 31a-b, and 33a-b). The computed results generally display an increasing \bar{C}_p with X, which implies a decreasing $\Delta \bar{u}$. On the other hand, the experimental results generally display a decreasing C_p^e with X, implying an increasing Δu^e . When the store is beyond the cavity opening at $Z_s/H = -0.30$, the computed \bar{C}_p and measured C_p^e distributions in Figs. 35a and b are in much better agreement than for the cases with $Z_s/H \geq 0$. This is consistent with the observation from the computed Mach number contours in Fig. 38 that the store basically remains outside the shear layer.

The computations show the trend of the velocity in and near the center of the shear layer to decay faster with X than in the experiment. This problem generally results from inadequate spatial resolution which artificially diffuses the shear layer. Large oscillations of the shear

layer cause it to move into regions with much coarser grid resolution. Thus, the differences observed between the measured and computed C_p may be caused by inadequate spatial resolution of the shear layer. Further investigation of the details of the computed shear layer is warranted.

4.4 STING INTERFERENCE

The interference induced on the store by the sting can be evaluated by removing the sting and recalculating the flow field. This process was accomplished by replacing the sting grid with a grid to cap off the end of the store (see Section 3.3.2). Experience has shown that using the identical store mesh for both calculations gives the best support interference predictions. Although no experimental data are available for the cases presented, the computations are shown to demonstrate the capability of computing sting interference and to provide an estimate of the magnitude of the interference.

First, the sting interference for the store in a free-stream flow is discussed. These results are presented to demonstrate sting interference computations for a simpler flow field for which the interference is easier to understand. Sting interference with the store placed at $Z_s/H = 0$ in the cavity will be discussed next. The trends for sting interference in a free-stream flow will then be compared to those for the store within the cavity. For both computations, results at $M_\infty = 0.60, 0.95,$ and 1.20 are presented.

4.4.1 Sting Interference in a Free-Stream Flow

Steady-state computations for a store alone were made and compared to the computations made for the store/sting in a free-stream flow (see Section 4.2). The C_p distributions are shown in Figs. 40-42 for the free-stream and cavity sides of the store at $M_\infty = 0.60, 0.95,$ and 1.20 . In all three figures, the solid line is the computation of the store with a sting, and the dashed line represents the computation of the store without the sting. As expected, greater differences occur on the store farther upstream for the subsonic $M_\infty = 0.60$ and 0.95 cases than for the supersonic $M_\infty = 1.20$ case. Also, the difference in C_p distributions for the free-stream side of the store is slightly greater than for the cavity side of the store. This result was expected since the sting is bent very close to the base of the store in the direction of the free-stream side of the store, thereby creating greater interference.

Sting interference was quantified by integrating the computed pressure distributions over the store to give the coefficient of the normal force (C_N) and the coefficient of the pitching moment (C_m) of the store. C_N is positive in the $+Z$ direction and C_m is positive nose down into the cavity. The area of integration was the same for the store/sting and store alone,

with no inclusion of forces from the base of the store. The values obtained for C_N and C_m , as well as the differences (ΔC_N and ΔC_m), where

$$\Delta C_N = C_{N, \text{ with the sting}} - C_{N, \text{ without the sting}} \quad (5)$$

$$\Delta C_m = C_{m, \text{ with the sting}} - C_{m, \text{ without the sting}} \quad (6)$$

are given in Table 1. For all Mach numbers, C_N increases with the addition of the sting while the C_m decreases. The largest changes in C_N and C_m occur at $M_\infty = 0.95$, near sonic conditions where support interference has been shown to be greatest (Ref. 8).

4.4.2 Sting Interference in a Cavity

Computations for a store alone at $Z_s/H = 0$ in the cavity were made and compared to computations for the store/sting (see Section 4.3). The first comparisons presented in Figs. 43-45 are the \bar{C}_p distributions along the sides of the store at $M_\infty = 0.60$, 0.95, and 1.20. These cavity comparisons differ greatly from the corresponding results for the store in a free-stream flow (see Figs. 40-42). At $M_\infty = 0.60$ (Fig. 43), the difference between the C_p distributions is detectable from just past the store nose all the way to the aft end of the store on the free-stream side and along the entire cavity side of the store. Interestingly, the shift in C_p distribution changes sign over the aft quarter of the store. At $M_\infty = 0.95$ (Fig. 44), a large difference consisting of a nearly uniform positive shift in \bar{C}_p is observed between the \bar{C}_p distributions on both the free-stream and cavity sides of the store. At $M_\infty = 1.20$ (Fig. 45), the difference between the \bar{C}_p distributions on the free-stream side of the store is similar to the result obtained at $M_\infty = 0.95$ (see Fig. 44a), while on the cavity side, the difference between the \bar{C}_p distributions has a sign change over the aft portion of the store as it does at $M_\infty = 0.60$ (Fig. 43b).

The computed time-averaged \bar{C}_N and \bar{C}_m , as well as their standard deviations (σ) are presented in Table 2 for the store/sting and store alone. The differences $\Delta \bar{C}_N$ and $\Delta \bar{C}_m$ [Eqs. (5) and (6)] are also given. Some of the trends seen in the free-stream flow results are also seen here. The addition of the sting increases \bar{C}_N for $M_\infty = 0.95$ and 1.20, but not for $M_\infty = 0.60$. For all cases, the presence of the sting causes \bar{C}_m to decrease. A notable difference from the free-stream case is that the greatest interference is seen at $M_\infty = 1.20$, not at $M_\infty = 0.95$.

The standard deviations in Table 2 show large variations in both C_N and C_m for most Mach numbers, with the value of the σ 's being larger than the time-averaged values \bar{C}_N and \bar{C}_m . To illustrate the variations in C_N and C_m that the store experiences, computed time histories of these values are given in Figs. 46 and 47 at $M_\infty = 0.60$ for the store/sting and

store alone, respectively. The solid lines represent the instantaneous values of C_N and C_m of the store and the dashed lines represent the time-averaged values. The store is clearly subjected to large, rapid variations with or without the sting. Similar results have been computed for $M_\infty = 0.95$ and 1.20 , but are not presented here since they do not provide additional information.

5.0 CONCLUSIONS

The capability to compute store/sting configurations in a cavity has been demonstrated. Complete validation was not achieved, in part at least because deficiencies in the technique used to obtain the time-averaged experimental unsteady pressures led to excessive measurement variability. Moreover, there are questions concerning the adequacy of the shear layer representation in the computations. Nevertheless, the results obtained are considered adequate to allow for the assessment of support interference by considering the differences between the support-on and the support-off solutions. Further assessment of loads and trajectory predictions must be postponed until the computational results are combined with engineering methods (Ref.4).

The following conclusions can be drawn for the computations presented in this report at Mach numbers of 0.60 , 0.95 , and 1.20 :

1. Several factors were important in obtaining solutions for the empty cavity and the store/sting in the cavity. Specifically, increasing the cell size within the cavity helps the numerical stability and reduces the computer time required to obtain a solution. However, the questionable adequacy of the shear layer representation may necessitate a reassessment of the cell-size requirements. Also, use of a satisfactory representation of the approaching boundary layer greatly improves the solution.
2. The flow within the empty cavity was observed to be highly unsteady, with the shear layer moving in and out of the cavity. Very low-amplitude velocities were measured and computed in the front region of the cavity, and highly varying velocity amplitudes occurred in the aft region of the cavity. Comparisons of the computations with experimental data were typically good, although clouded by the fact that the steady-state ESP measuring techniques do not adequately capture the time average of the flow.
3. Excellent agreement between the computational and measured data was obtained for the isolated store/sting in the uniform free-stream flow. The shock location was observed to be slightly shifted from the data for the transonic and low supersonic flow computations, which is consistent with the inviscid flow approximation.

4. The agreement between computations and experimental data for the store/sting in the cavity varied with the position of the store. When the store was positioned at the plane of the cavity opening ($Z_s/H = 0$), poor agreement was observed on the aft portion of the store for all computed Mach numbers. The computed difference in pressure across the store agreed well with the data. When the store was positioned deep within the cavity ($Z_s/H = 0.75$) at $M_\infty = 1.20$, the agreement between computed and experimental data on the aft portion of the store deteriorated. However, the computed difference in pressure across the store agreed well with measurement and was similar to what was seen for the store at the plane of the cavity opening. Finally, when the store is positioned outside of the weapons bay at $Z_s/H = -0.30$ for $M_\infty = 1.20$, the agreement between computations and experimental data was found to be good, probably because the store was outside the shear layer.
5. It is believed that the poor agreement between the computations and measurements for the aft region of the cavity indicates that the shear layer needs more resolution to avoid excessive dissipation of the streamwise velocity component within the shear layer.
6. The computed sting interference was shown to be significant for both the store in a uniform free-stream flow and within the cavity flow. The sting interference for the isolated store in a uniform free-stream flow showed the expected variations with M_∞ . When the store was positioned in the plane of the cavity opening, the sting interference was greater in magnitude and quite different in character from that in a uniform free-stream flow.

REFERENCES

1. Dix, R. E. and Butler, C. "Cavity Aeroacoustics." *Proceedings of the Store Carriage Integration and Release Conference*, Bath, U.K., The Royal Aeronautical Society, April 1990.
2. Bauer, R. C. and Dix, R. E. "Engineering Model of Unsteady Flow in a Cavity." AEDC-TR-91-17, December 1991.
3. Suhs, N. E. "Computations of Three Dimensional Cavity Flow at Subsonic and Supersonic Mach Numbers." AIAA-87-1208, June 1987.
4. Keen, K. S. "New Approaches to Computational Aircraft/Store Weapons Integration." AIAA-90-0274, January 1990.

5. Dougherty, F. C. "Development of a Chimera Grid Scheme with Applications to Unsteady Problems." Ph.D Dissertation, Stanford University, April 1985.
6. Dougherty, F. C. and Kuan, J. "Transonic Store Separation Using a Three-Dimensional Chimera Grid Scheme." AIAA-89-0637, January 1989.
7. Meakin, R. L. and Suhs, N. E. "Unsteady Aerodynamic Simulation of Multiple Bodies in Relative Motion." AIAA-89-1966, June 1989.
8. Suhs, N. E. "Computational Estimates of Strut Support Interference at Transonic Mach Numbers." AIAA-85-5018, October 1985.
9. Rossiter, J. E. "Wind Tunnel Experiments on the Flow over Rectangular Cavities at Subsonic and Transonic Speeds." British A.R.C., R & M No. 3438, 1966.
10. Heller, H. H. and Bliss, D. B. "Aerodynamically Induced Pressure Oscillations in Cavities—Physical Mechanisms and Suppression Concepts." AFFDL-TR-74-133, February 1975.
11. Kaufman, L. G. II, Maciulaitis, A., and Clark, R. L. "Mach 0.6 to 3.0 Flows Over Rectangular Cavities." AFWAL-TR-82-3112, May 1983.
12. Komerath, N. M., Ahuja, K. K., and Chambers, F. W. "Prediction and Measurement of Flows over Cavities—A Survey." AIAA-87-0166, January 1987.
13. Stallings, R. L., Jr. and Wilcox, F. J., Jr. "Experimental Cavity Pressure Distributions at Supersonic Speeds." NASA TP-2683, June 1987.
14. Stallings, R. L., Jr., Wilcox, F. J., Jr., and Forrest, D. K. "Measurements of Forces, Moments, and Pressures on a Generic Store Separating from a Box Cavity at Supersonic Speeds." NASA TP-3110, September 1991.
15. Wilcox, F., Jr. "Tangential, Semisubmerged, and Internal Store Carriage and Separation at Supersonic Speeds." AIAA-91-0198, January 1991.
16. Hankey, W. L. and Shang, J. S. "Analyses of Pressure Oscillations in an Open Cavity." *AIAA Journal*, Vol. 18, No. 8, August 1980, pp. 892-898.
17. Baysal, O. and Stallings, R. L., Jr. "Computational and Experimental Investigations of Cavity Flow Fields." AIAA-87-0144, January 1987.

18. Venkatapathy, E., Lombard, C. K., and Nagaraj, N. "Numerical Simulation of Compressible Flow Complex Two-Dimensional Cavities." AIAA-87-0166, January 1987.
19. Dougherty, N. S., Holt, J. B., Nesman, T. E., and Farr, R. A. "Time-Accurate Navier-Stokes Computations of Self-Excited Two-Dimensional Unsteady Cavity Flows." AIAA-90-0691, January 1990.
20. Gorski, J. J., Ota, D. K., and Chakravarthy, S. R. "Calculation of Three-Dimensional Cavity Flow Fields." AIAA-87-0117, January 1987.
21. Rizzetta, D. P. "Numerical Simulation of Supersonic Flow Over a Three-Dimensional Cavity." AIAA-87-1288, June 1987.
22. Baysal, O., Srinivasan, S., and Stallings, R. L., Jr. "Unsteady Viscous Calculations of Supersonic Flows Past Deep and Shallow Three-Dimensional Cavities." AIAA-88-0101, January 1988.
23. Baysal, O. and Srinivasan, S. "Navier-Stokes Calculations of Transonic Flow Past Cavities." NASA CR-4210, January 1989.
24. Baysal, O., Fouladi, K., Lessard, V., and Miller, D. "Navier-Stokes Computations of Internal and External Store Carriage and Separation." *Proceedings, 8th JOCG Aircraft/Store Compatibility Symposium*, Fort Walton Beach, FL, October 23-25, 1990.
25. Plentovich, E. B. "Three Dimensional Cavity Flow Fields at Subsonic and Transonic Speeds." NASA TM-4209, September 1990.
26. Benek, J. A., Steger, J. L., Dougherty, F. C., and Buning, P. G. "Chimera: A Grid-Embedding Technique." AEDC-TR-85-64 (AD-A167466), December 1985.
27. Benek, J. A., Donegan, T. L., and Suhs, N. E. "Extended Chimera Grid Embedding Scheme with Application to Viscous Flows." AIAA-87-1126CP, June 1987.
28. Suhs, N. E. and Tramel, R. W. "PEGSUS 4.0 User's Manual." AEDC-TR-91-8, October 1991.
29. Pulliam, T. H. and Steger, J. L. "On Implicit Finite-Difference Simulations of Three-Dimensional Flow." *AIAA Journal*, Vol. 18, No. 2, February 1980, pp.159-167.

30. Baldwin, B. S. and Lomax, H. "Thin Layer Approximation and Algebraic Model for Separated Turbulent Flows." AIAA-78-257, January 1978.
31. Anderson, D. A., Tannehill, J. C., and Pletcher, R. H. "Computational Fluid Mechanics and Heat Transfer." Hemisphere Publishing Corporation, New York, 1984 (First Edition).
32. Thompson, J. F., Warsi, Z. U. A., and Mastin, C. W. "Numerical Grid Generation: Foundation and Applications." North-Holland, New York, 1985.
33. Soni, B. K. "Grid Generation for Internal Flow Applications." AEDC-TR-85-25, July 1985.
34. Erickson, J. C., Jr., Wittliff, C. E., and Daughtry, D. C. "Further Investigations of Adaptive-Wall Wind Tunnels." AEDC-TR-80-34, October 1980.
35. Nenni, J. P., Erickson, J. C., Jr., and Wittliff, C. E. "Measurements of Small Normal Velocity Components in Subsonic Flows by Use of a Static Pipe." *AIAA Journal*, Vol. 20, No. 8, August 1982, pp. 1077-1083.

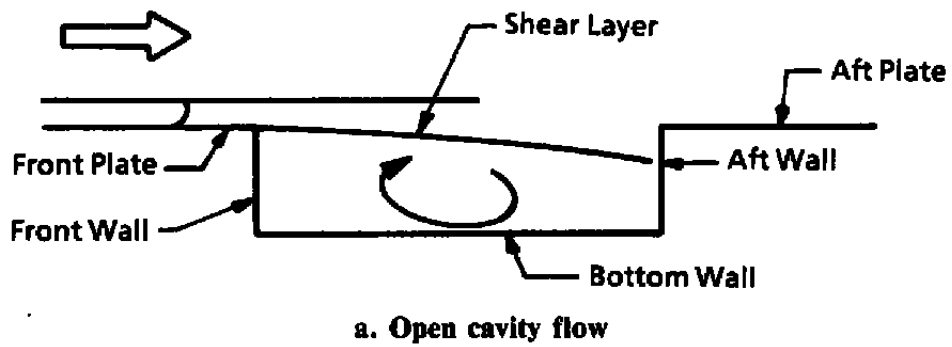


Figure 1. Flow in a cavity.

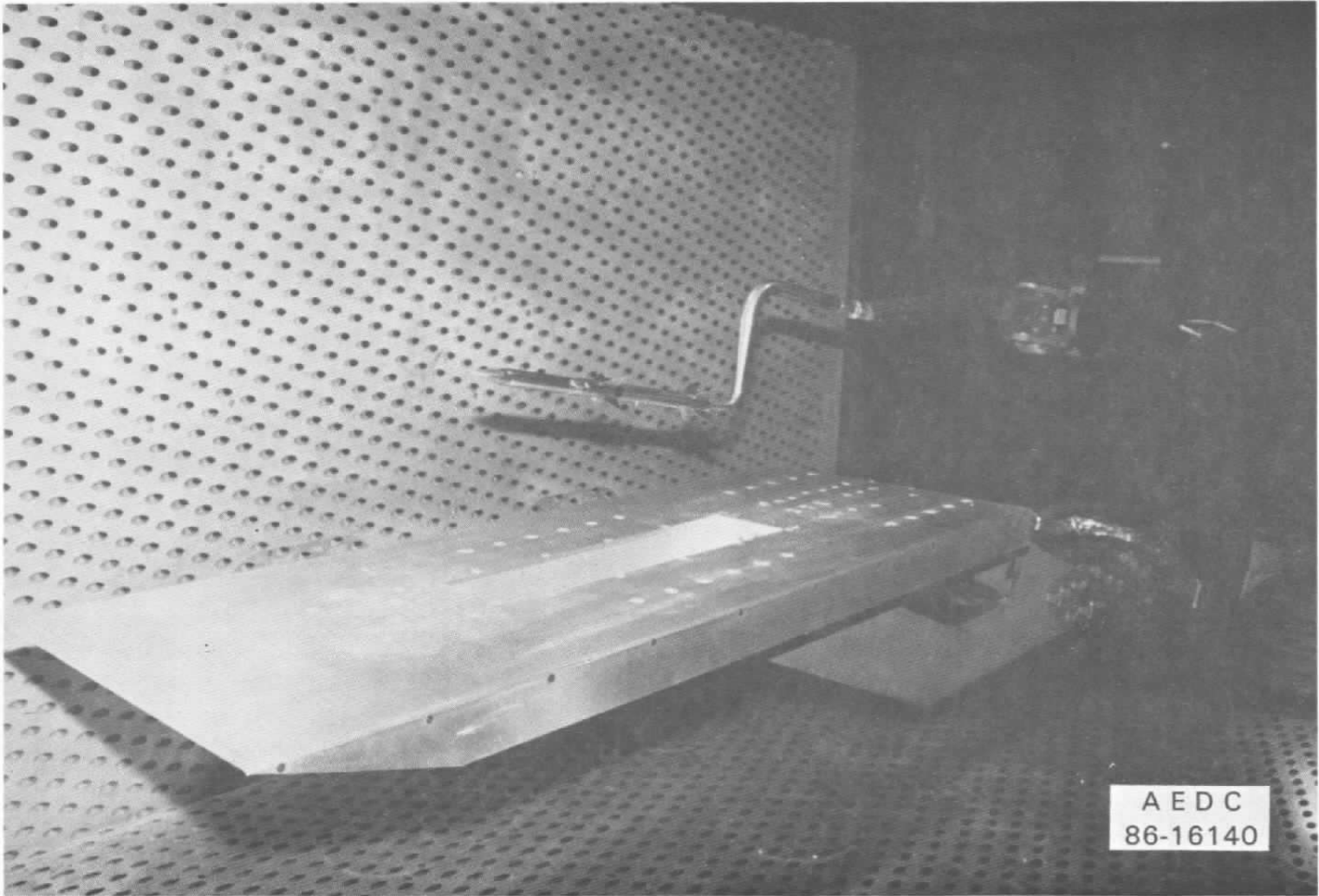
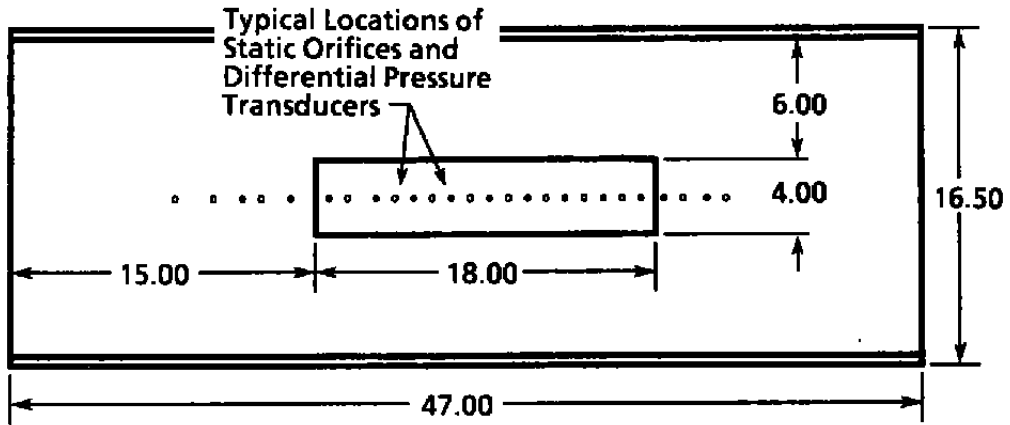
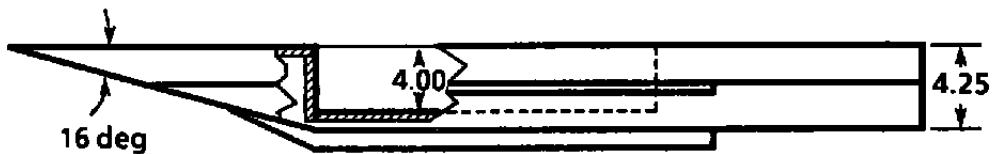


Figure 2. Photograph of WICS models installed in Tunnel 4T.

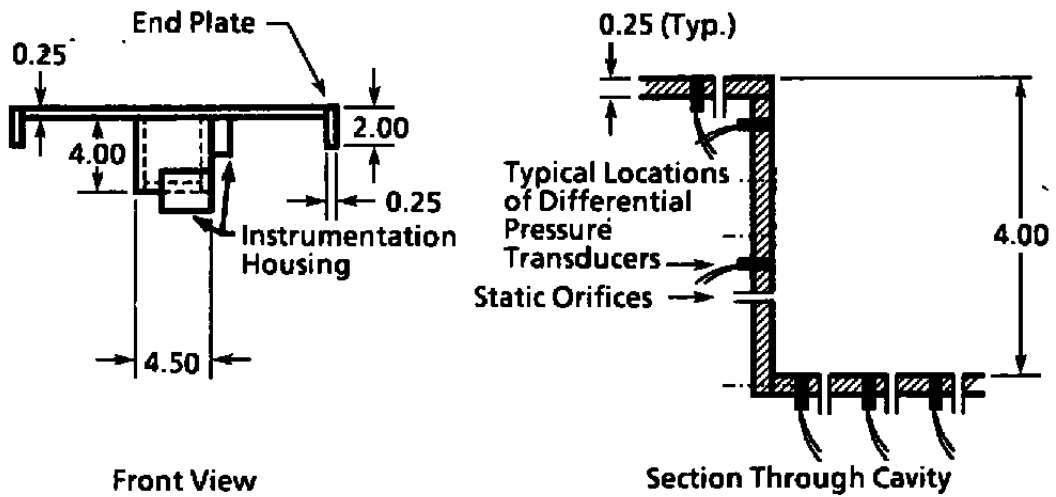
Linear Dimensions are Inches



Top View (As Mounted in Wind Tunnel) of Plate/Cavity Model



Side View



Front View

Section Through Cavity

Figure 3. Dimensions of the WICS flat-plate/cavity model.

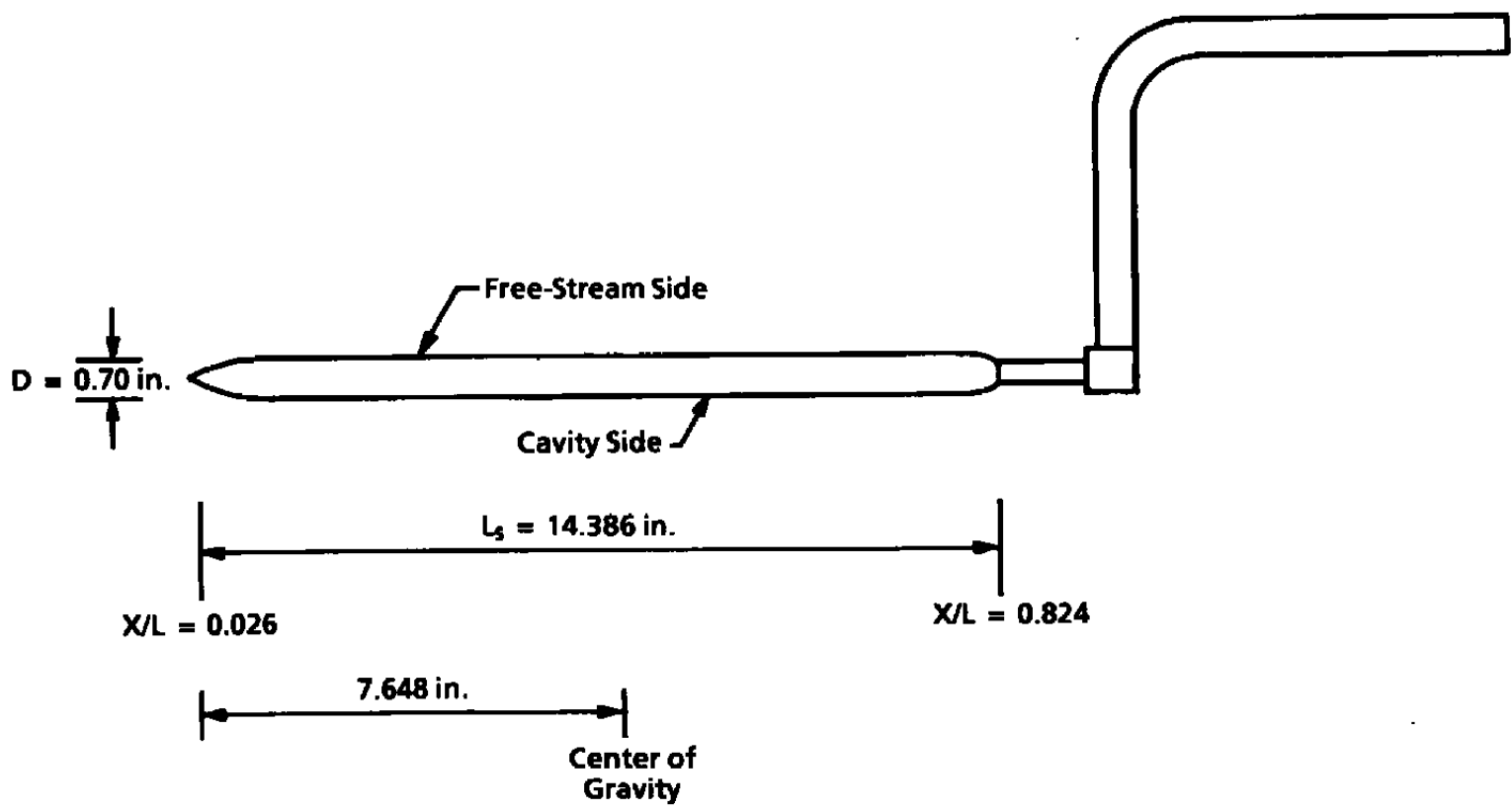
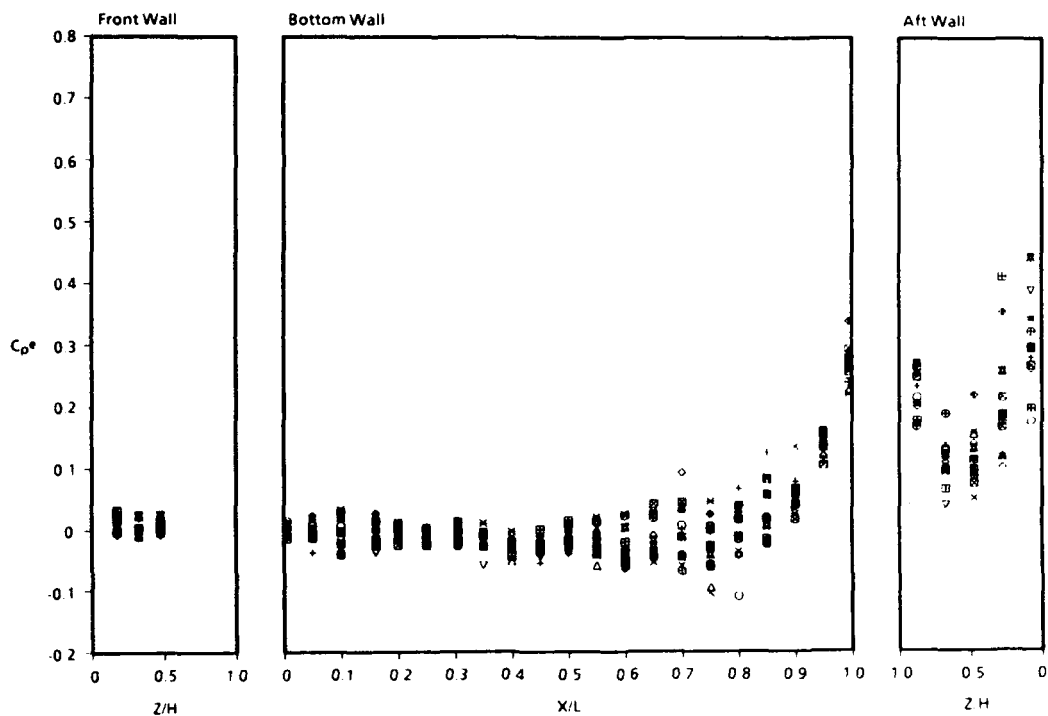
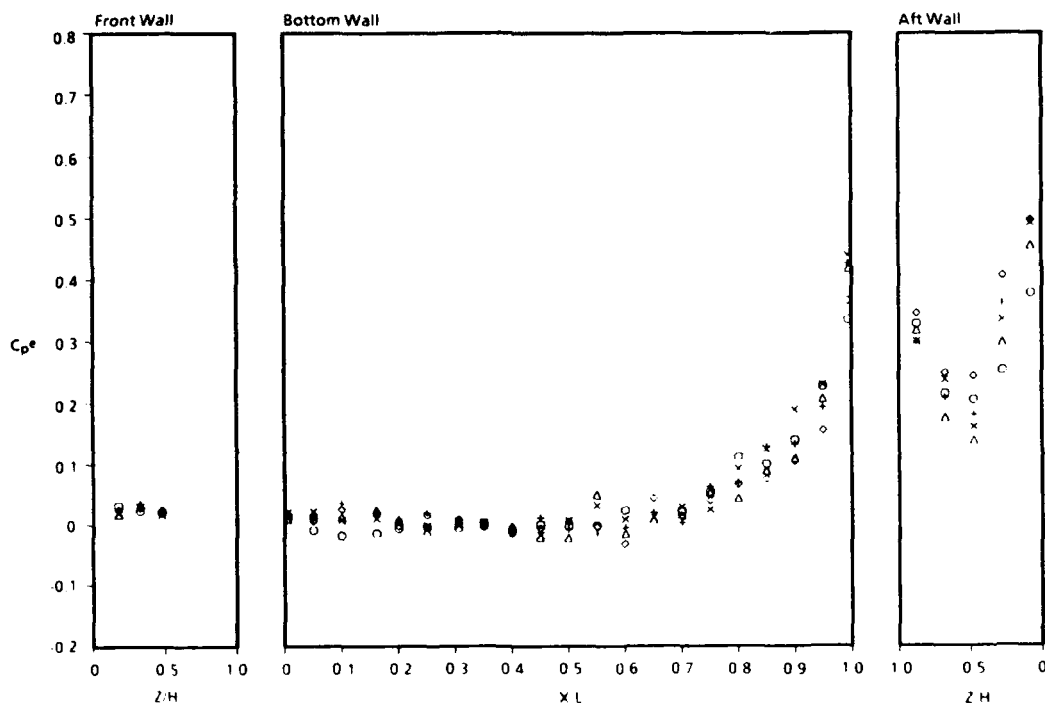


Figure 4. Store mounted on the bent sting.

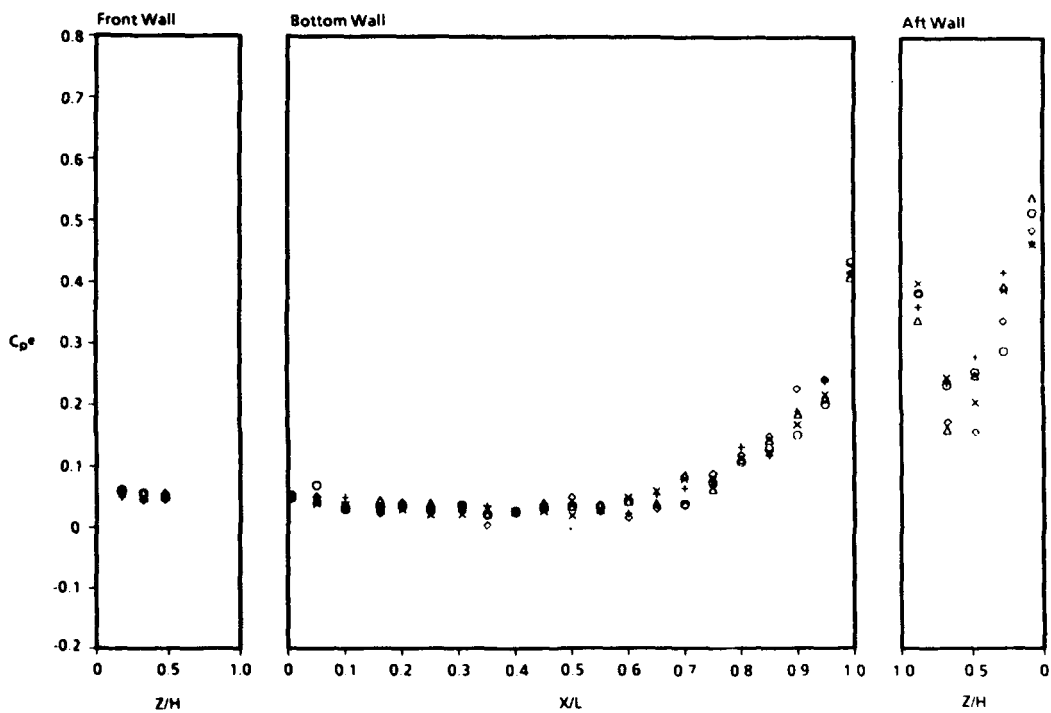


a. $M_\infty = 0.60$

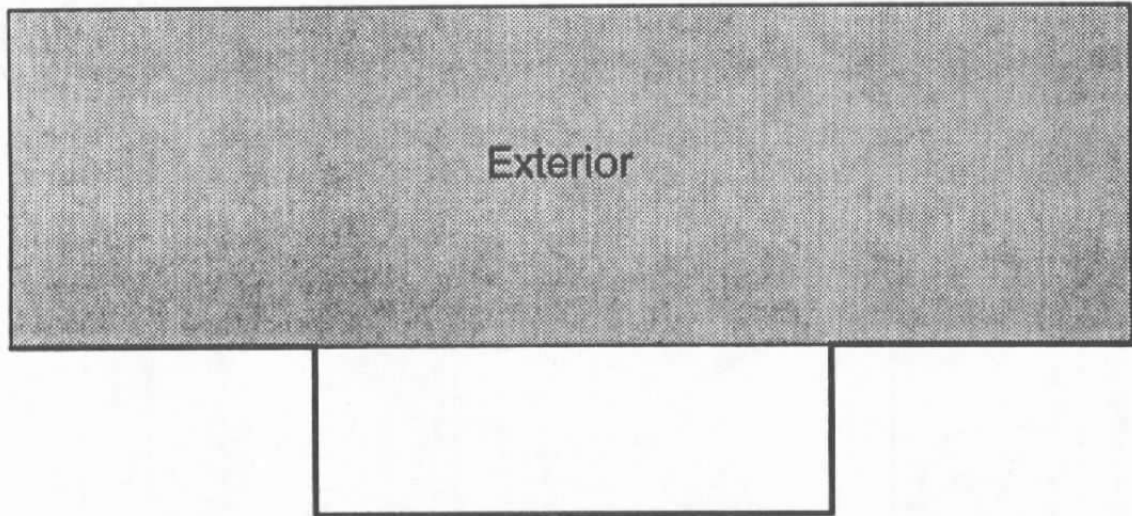


b. $M_\infty = 0.95$

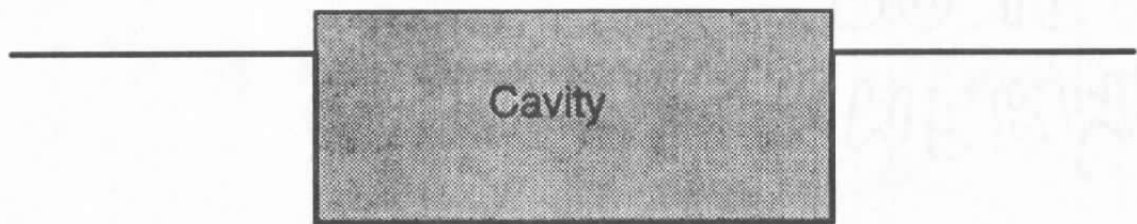
Figure 5. Experimental data samples along the centerline of the empty cavity walls.



c. $M_\infty = 1.20$
Figure 5. Concluded.



a. Exterior region



b. Cavity region

Figure 6. Computational regions for two-grid cavity configuration.

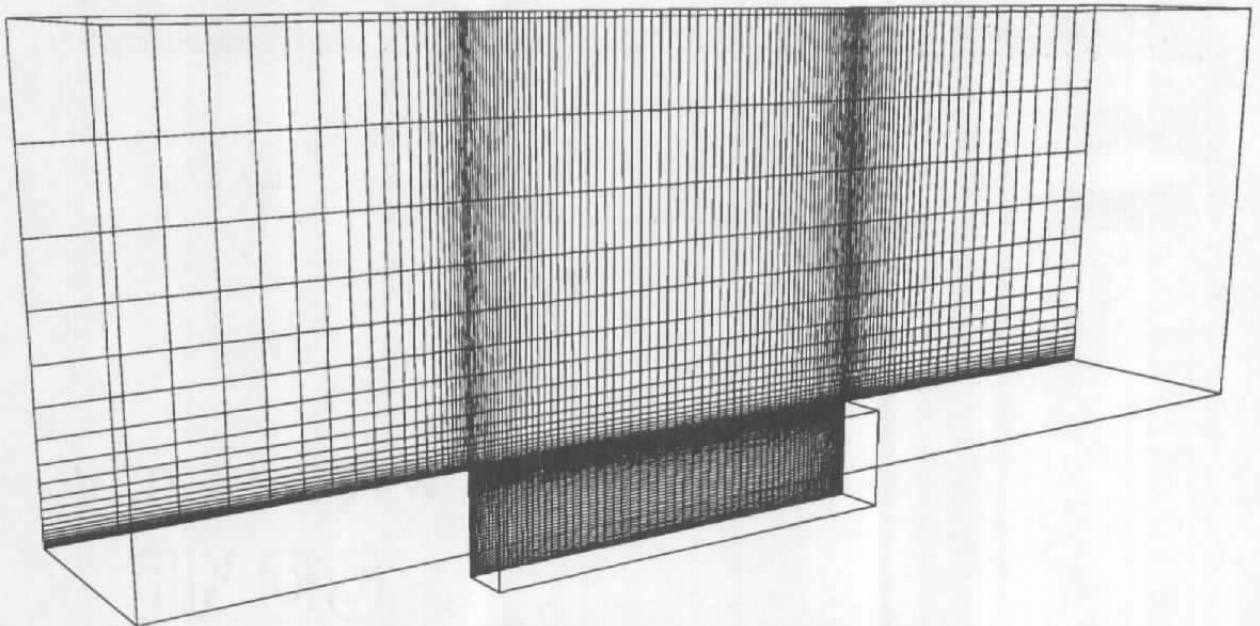
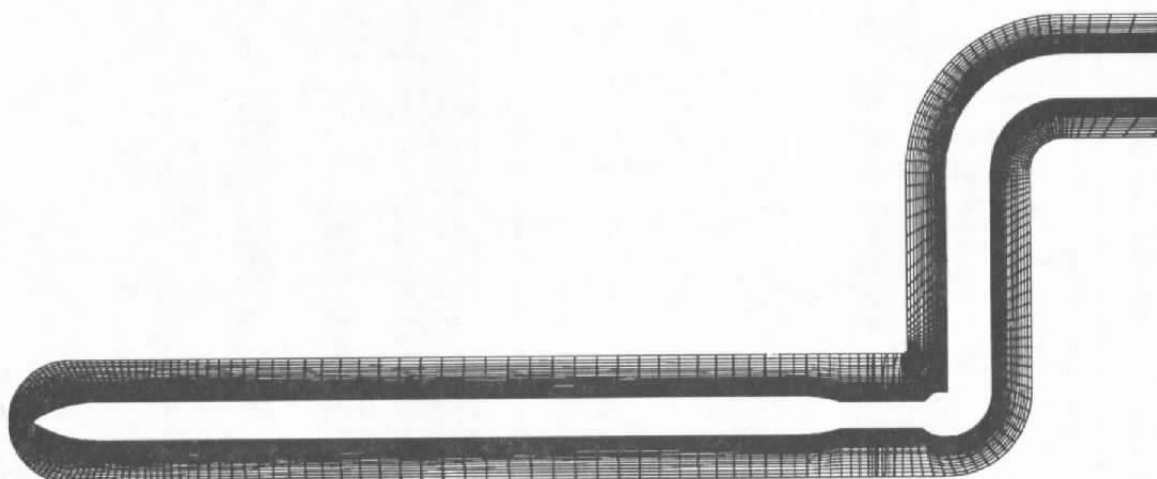
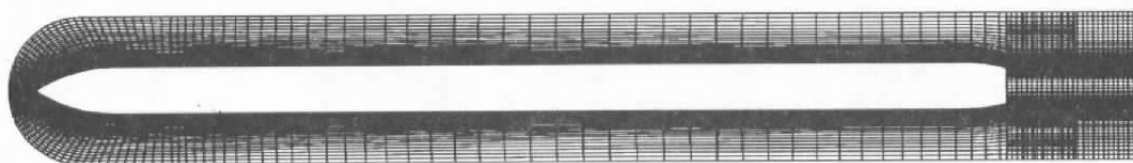


Figure 7. Symmetry plane grids of two-grid empty cavity configuration.

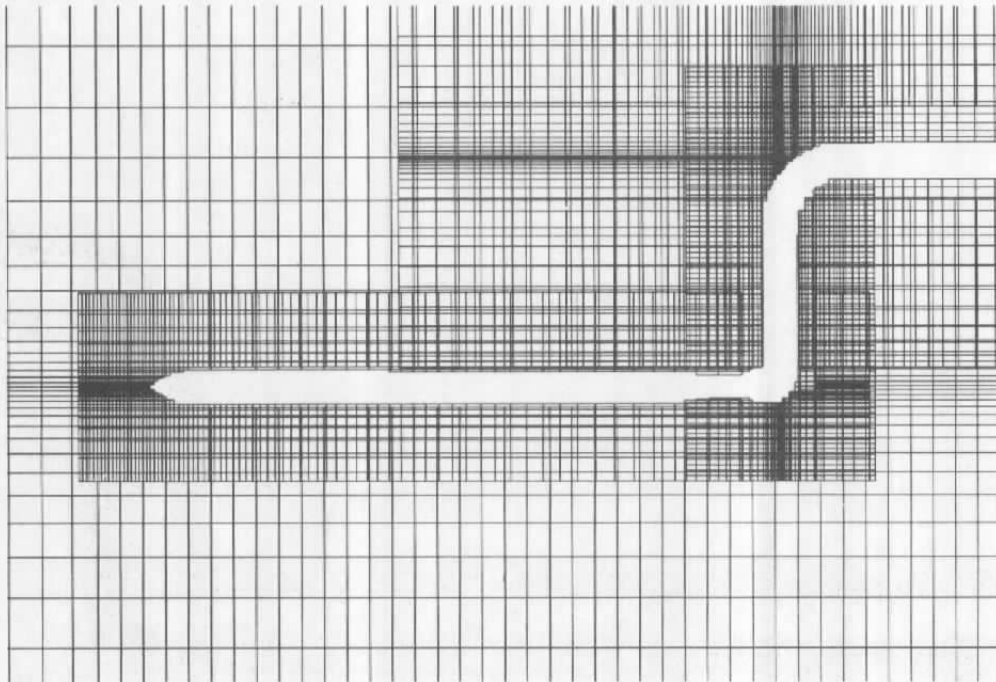


a. Store/sting

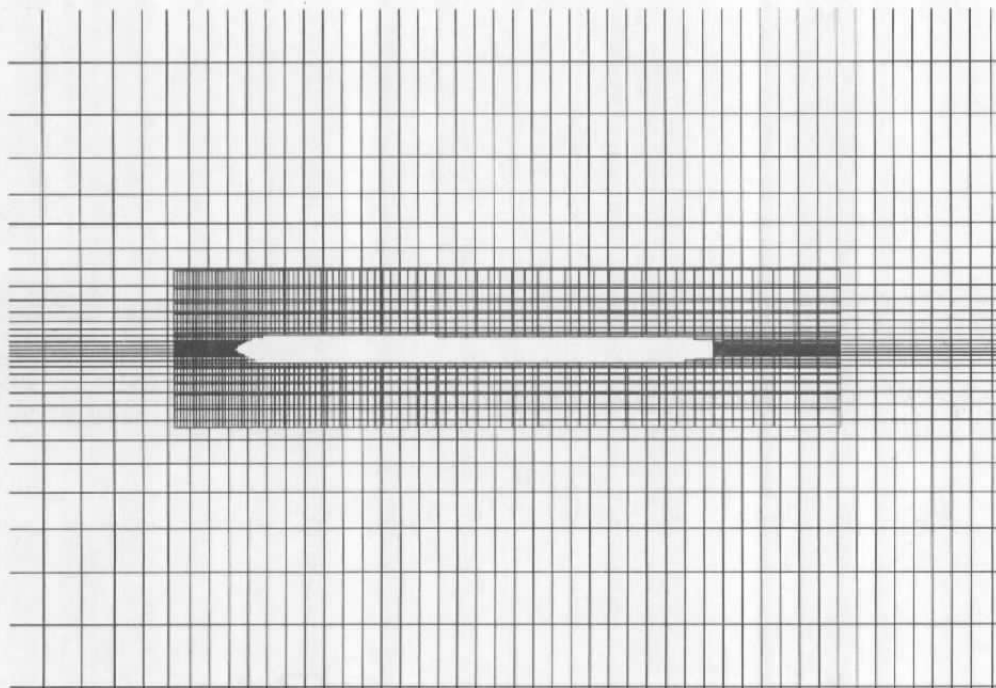


b. Store alone

Figure 8. Symmetry plane grids of the store/sting and store alone.

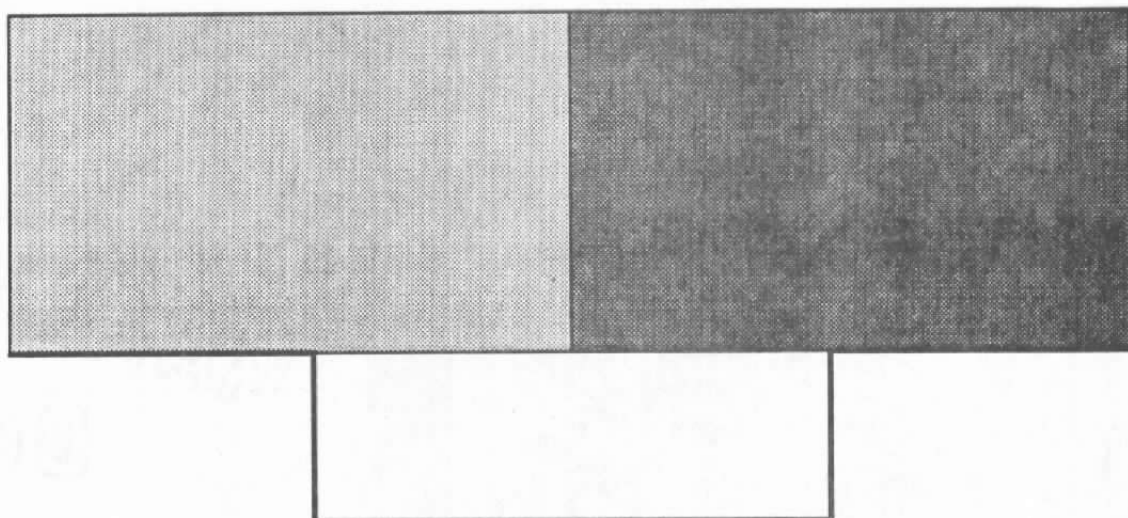


a. Store/sting

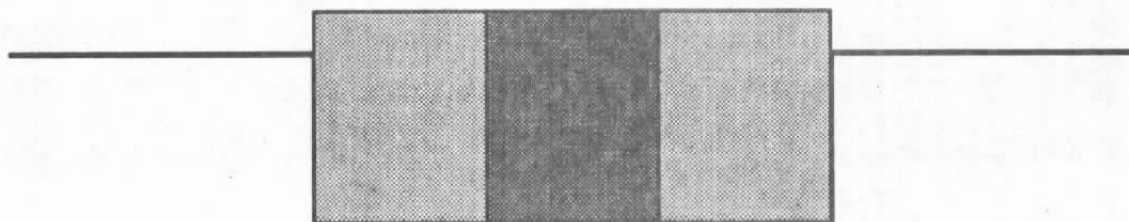


b. Store alone

Figure 9. Symmetry plane grids of the free-stream configuration with the store/sting and store alone.

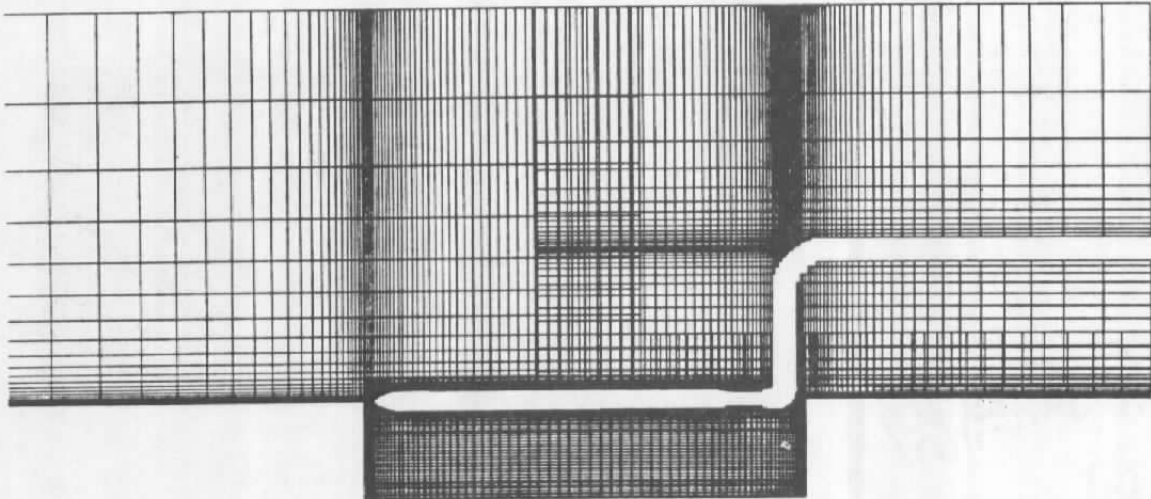


a. Exterior grids

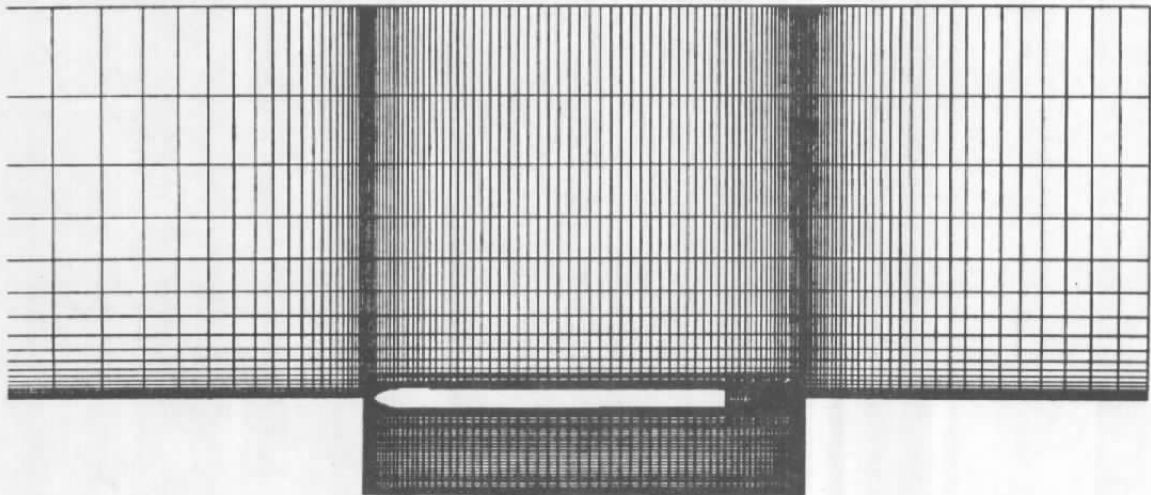


b. Cavity grids

Figure 10. Computational regions for the five-grid cavity configuration.



a. Store/sting



b. Store alone

Figure 11. Symmetry plane grids of the cavity configuration with the store/sting and store alone.

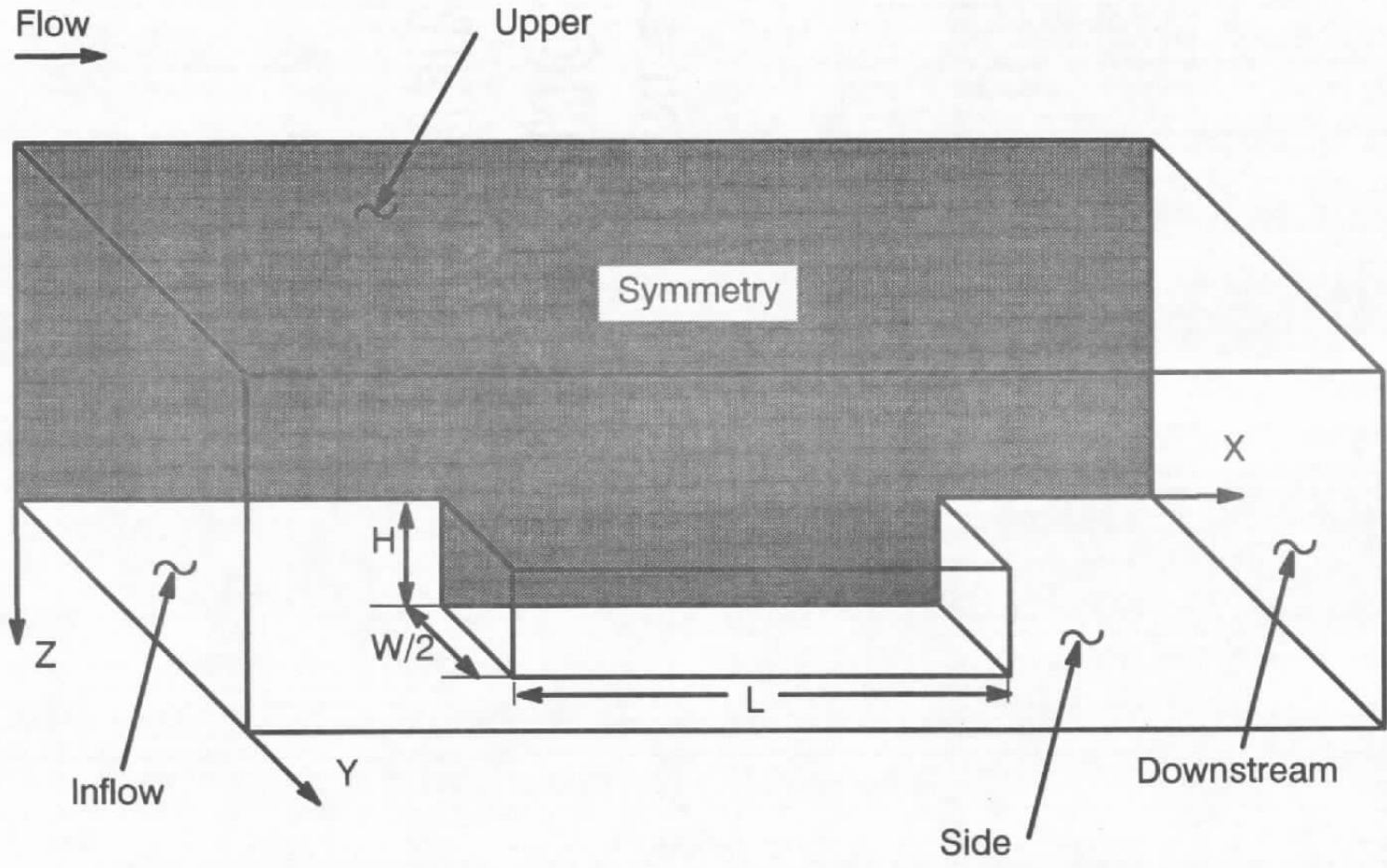
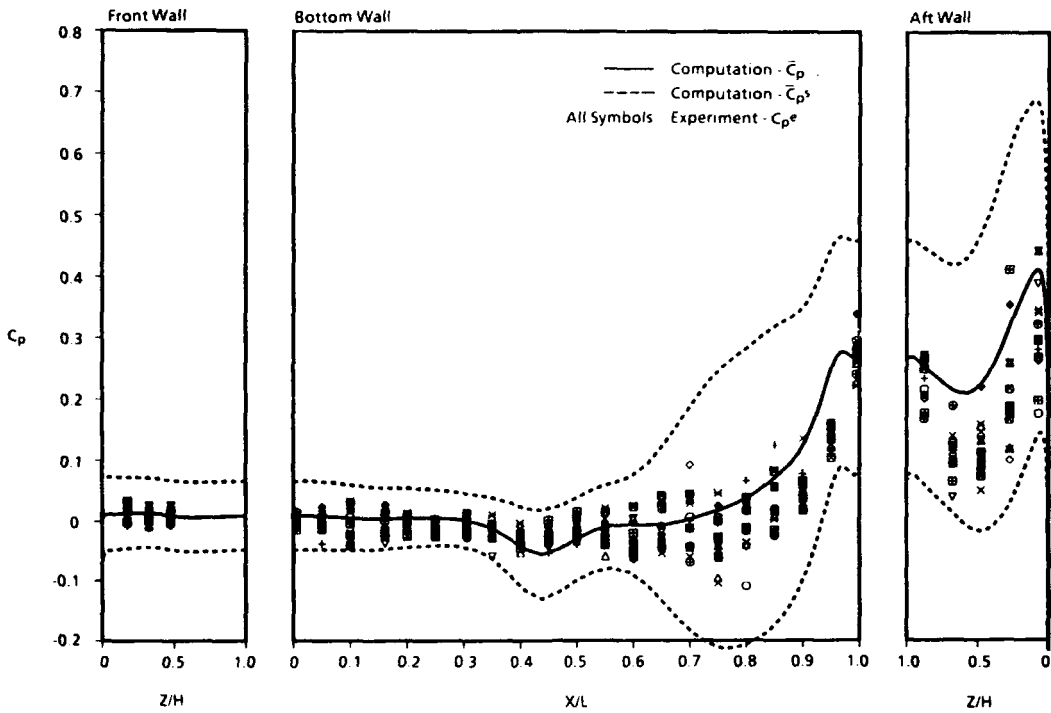
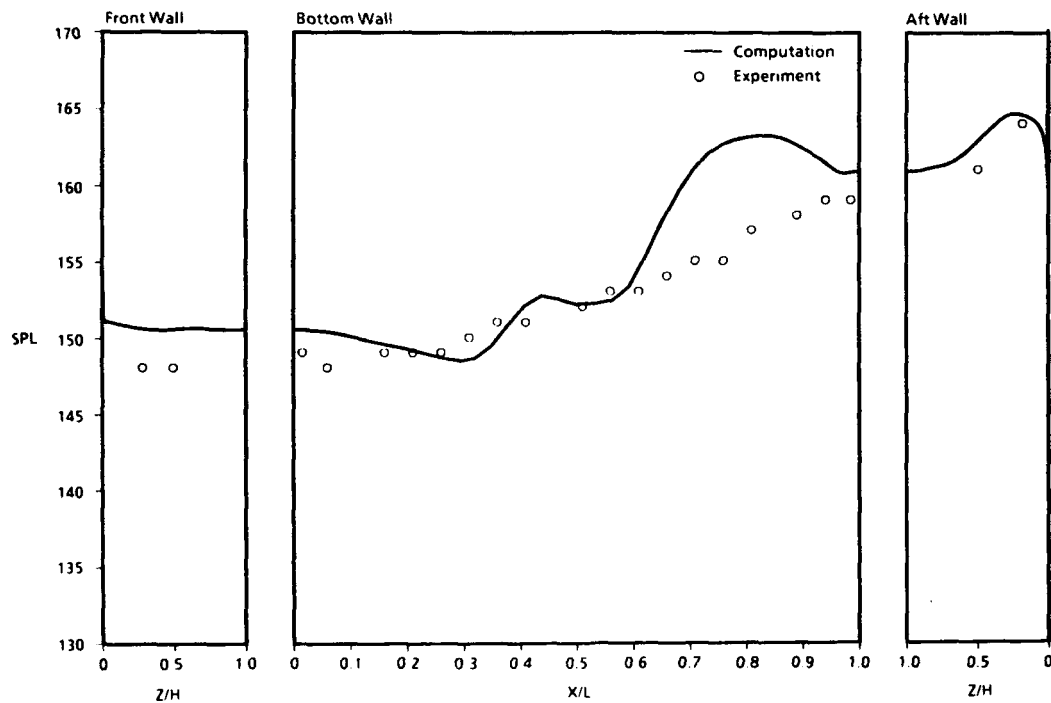


Figure 12. Diagram of the surfaces requiring boundary conditions.

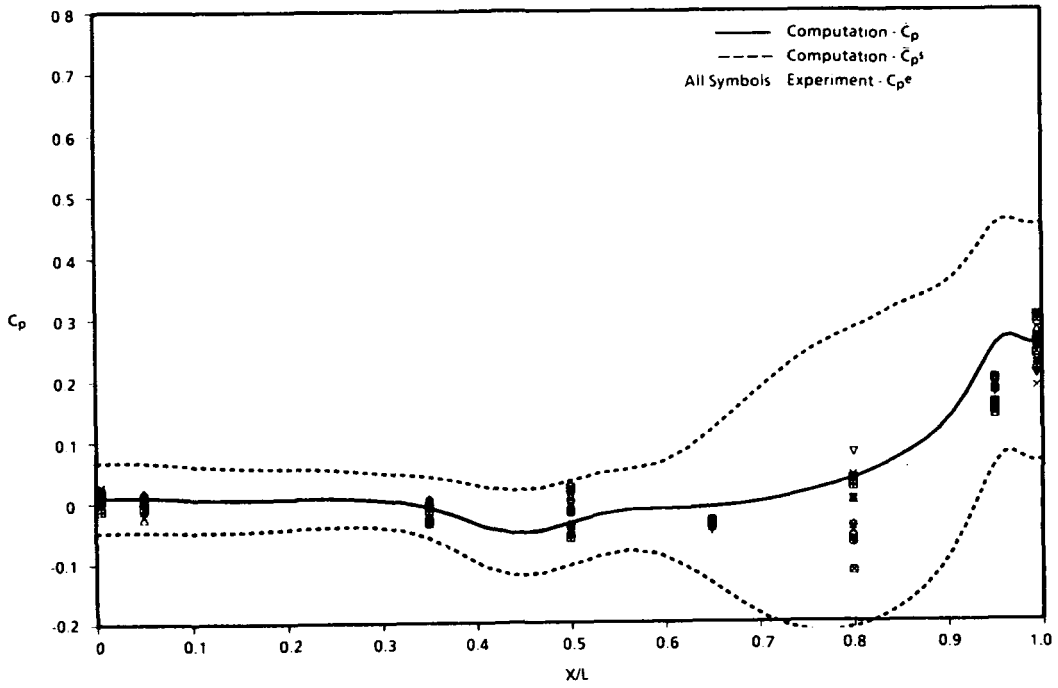


a. C_p on centerline, $Y/(W/2) = 0$

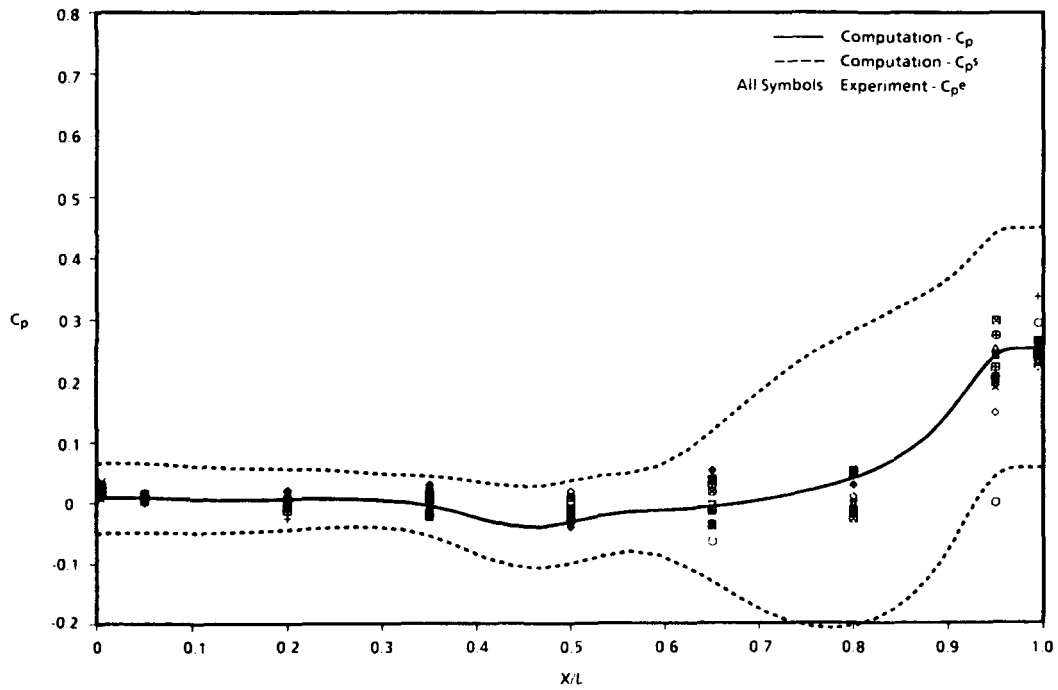


b. SPL on centerline, $Y/(W/2) = 0$

Figure 13. Comparison of computations and measurements on the empty cavity walls, $M_\infty = 0.60$.

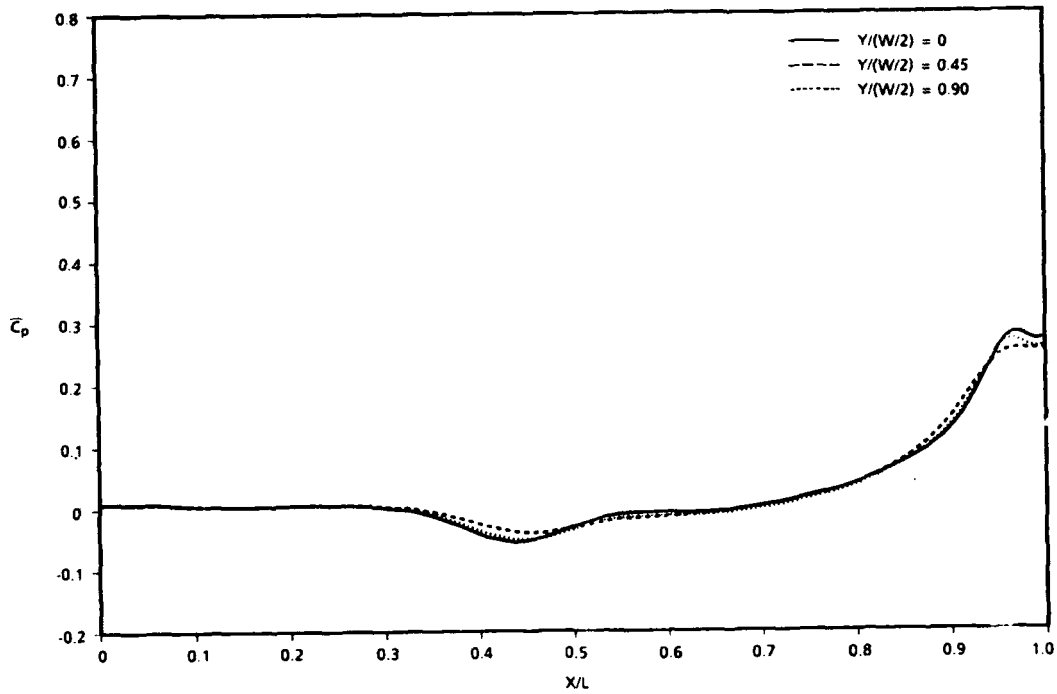


c. C_p on bottom wall, $Y/(W/2) = 0.45$

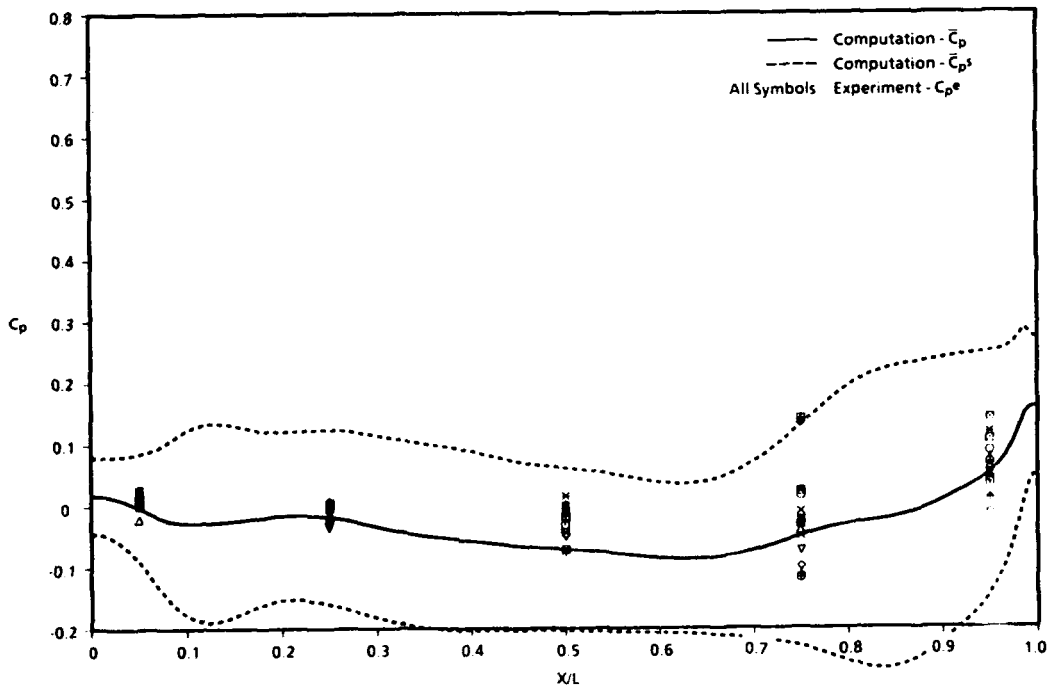


d. C_p on bottom wall, $Y/(W/2) = 0.9$

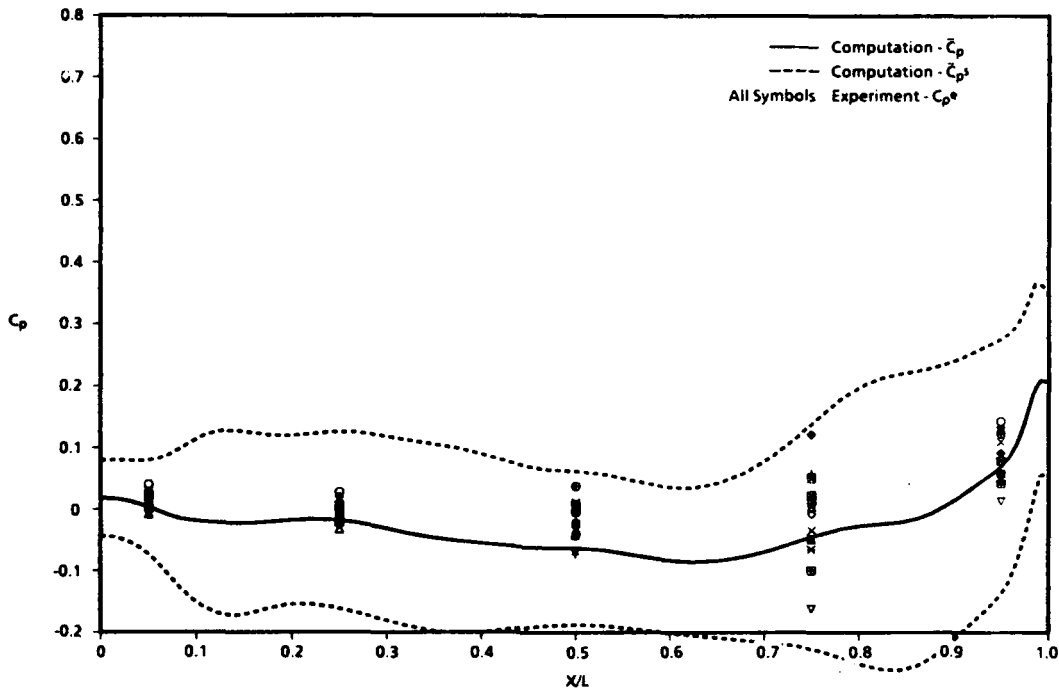
Figure 13. Continued.



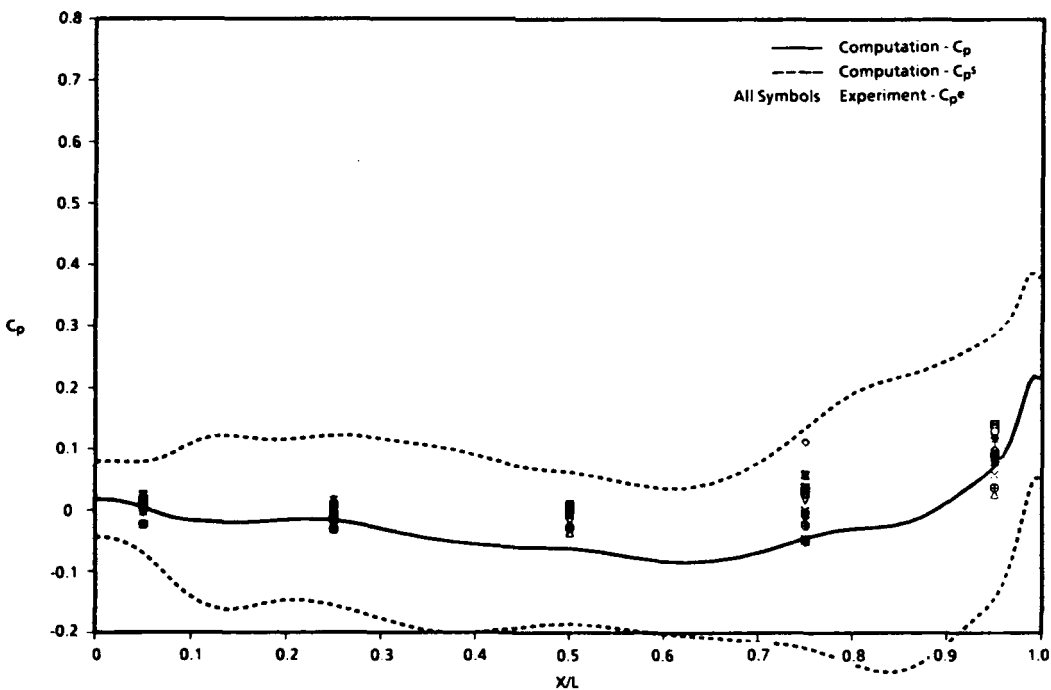
e. Computed \bar{C}_p on bottom wall, $Y/(W/2) = 0, 0.45, 0.9$



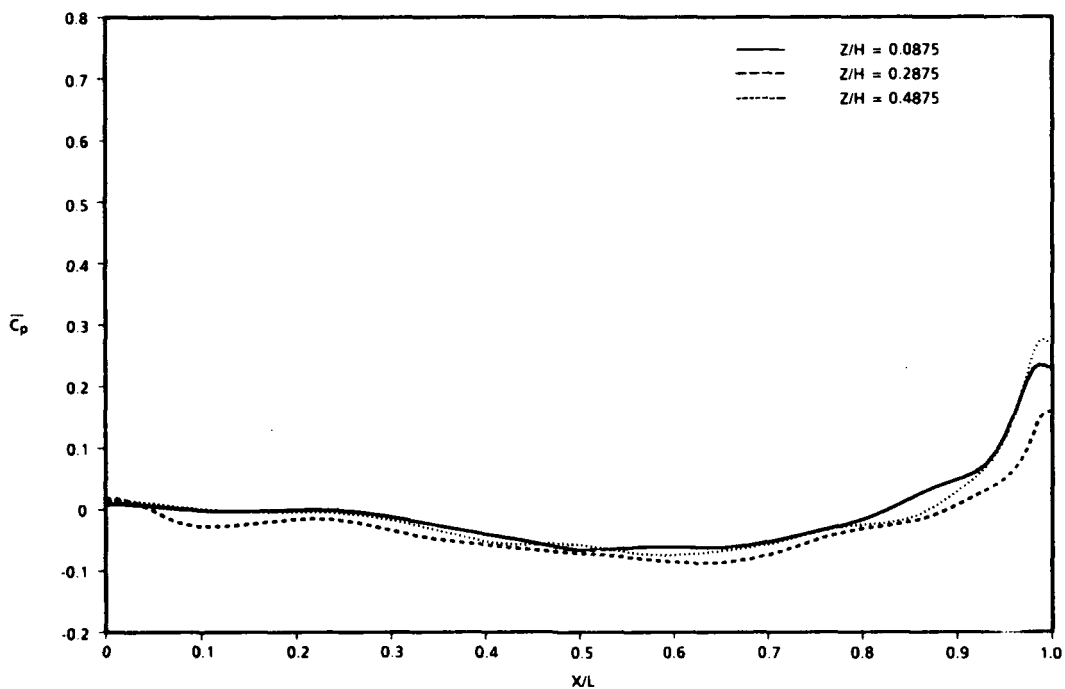
f. C_p on side wall, $Z/H = 0.0875$
Figure 13. Continued.



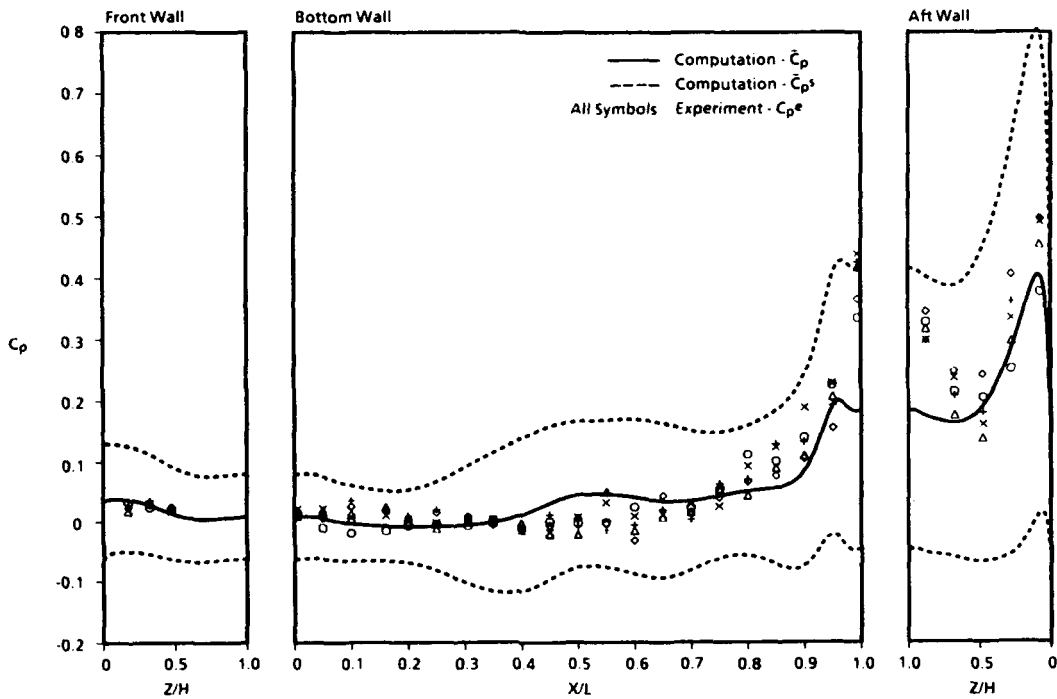
g. C_p on side wall, $Z/H = 0.2875$



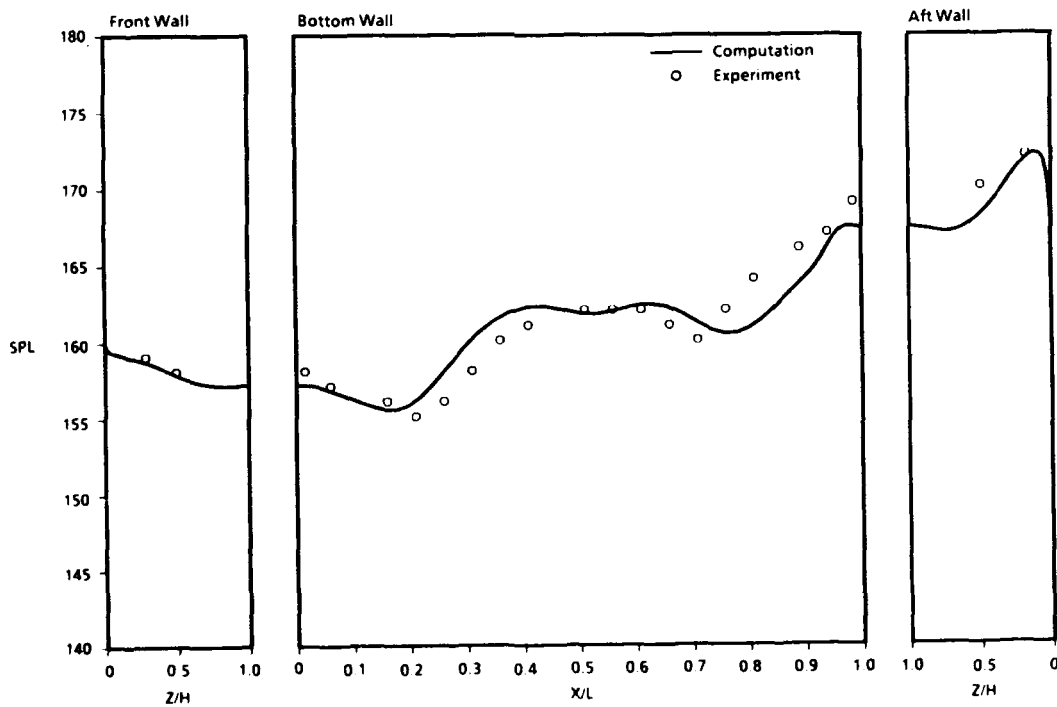
h. C_p on side wall, $Z/H = 0.4875$
 Figure 13. Continued.



i. Computed \bar{C}_p on bottom wall, $Z/H = 0.0875, 0.2875, 0.4875$
Figure 13. Concluded.

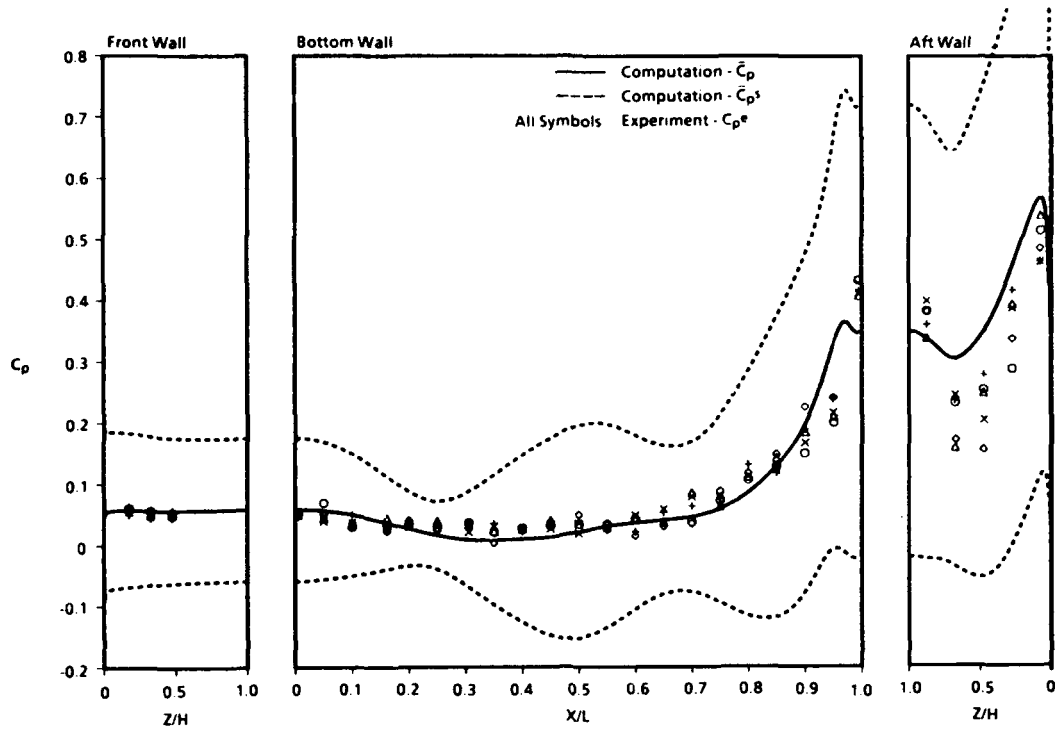


a. C_p on centerline, $Y/(W/2) = 0$

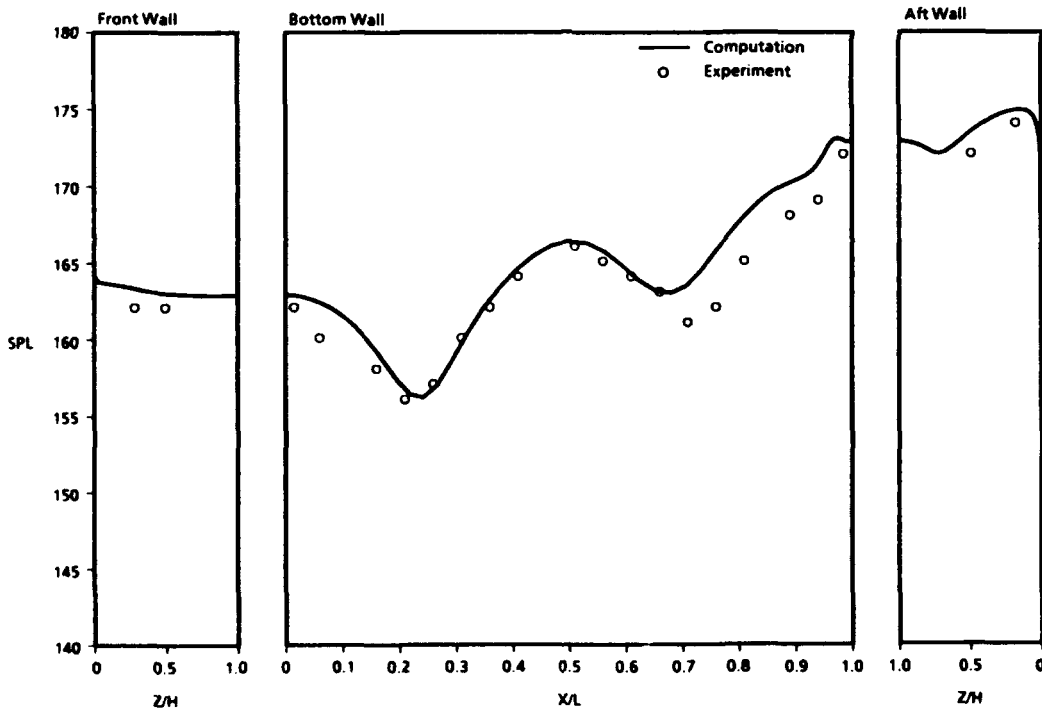


b. SPL on centerline, $Y/(W/2) = 0$

Figure 14. Comparisons of computations and measurements on the empty cavity walls, $M_\infty = 0.95$.

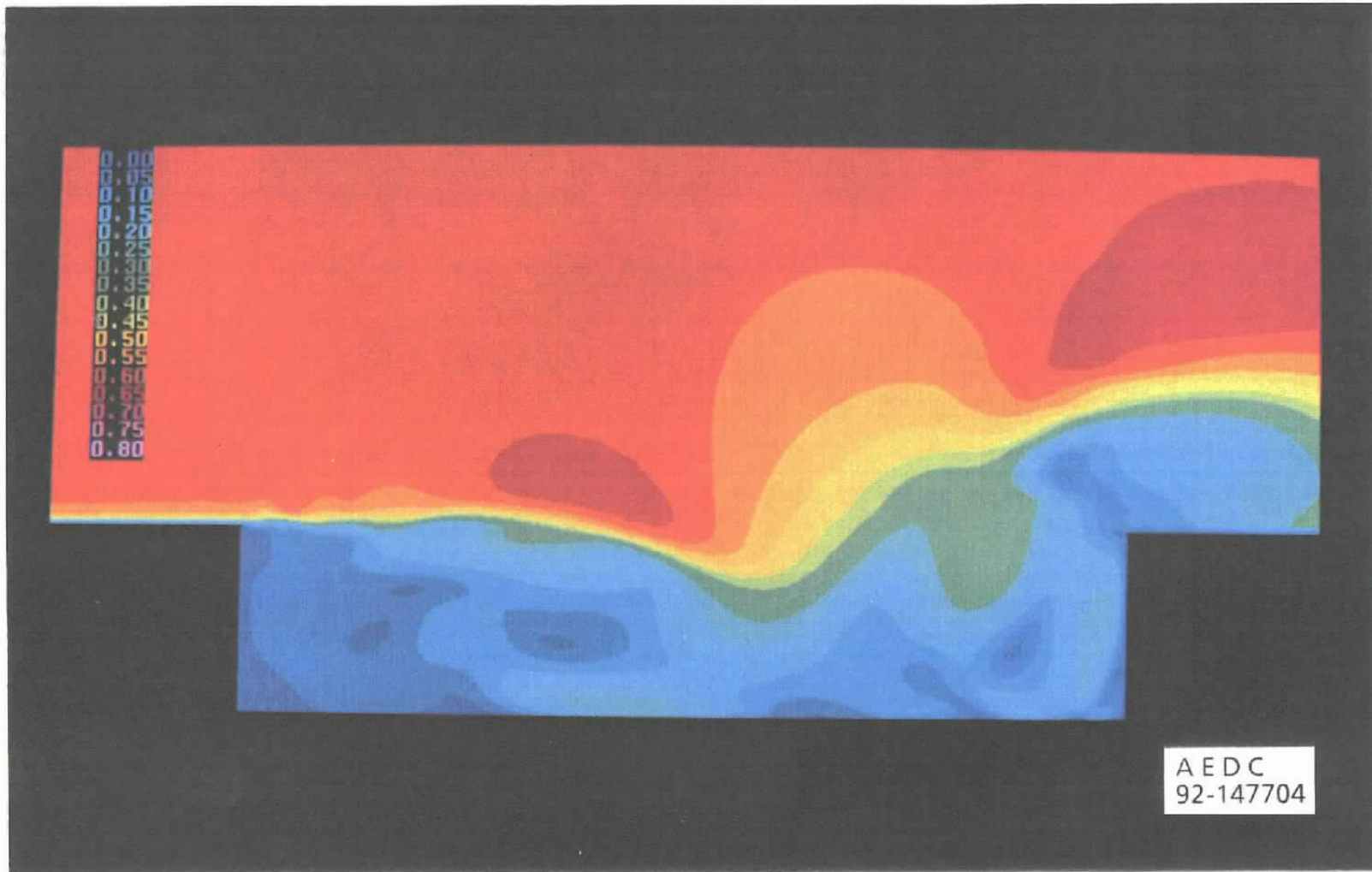


a. C_p on centerline, $Y/(W/2) = 0$



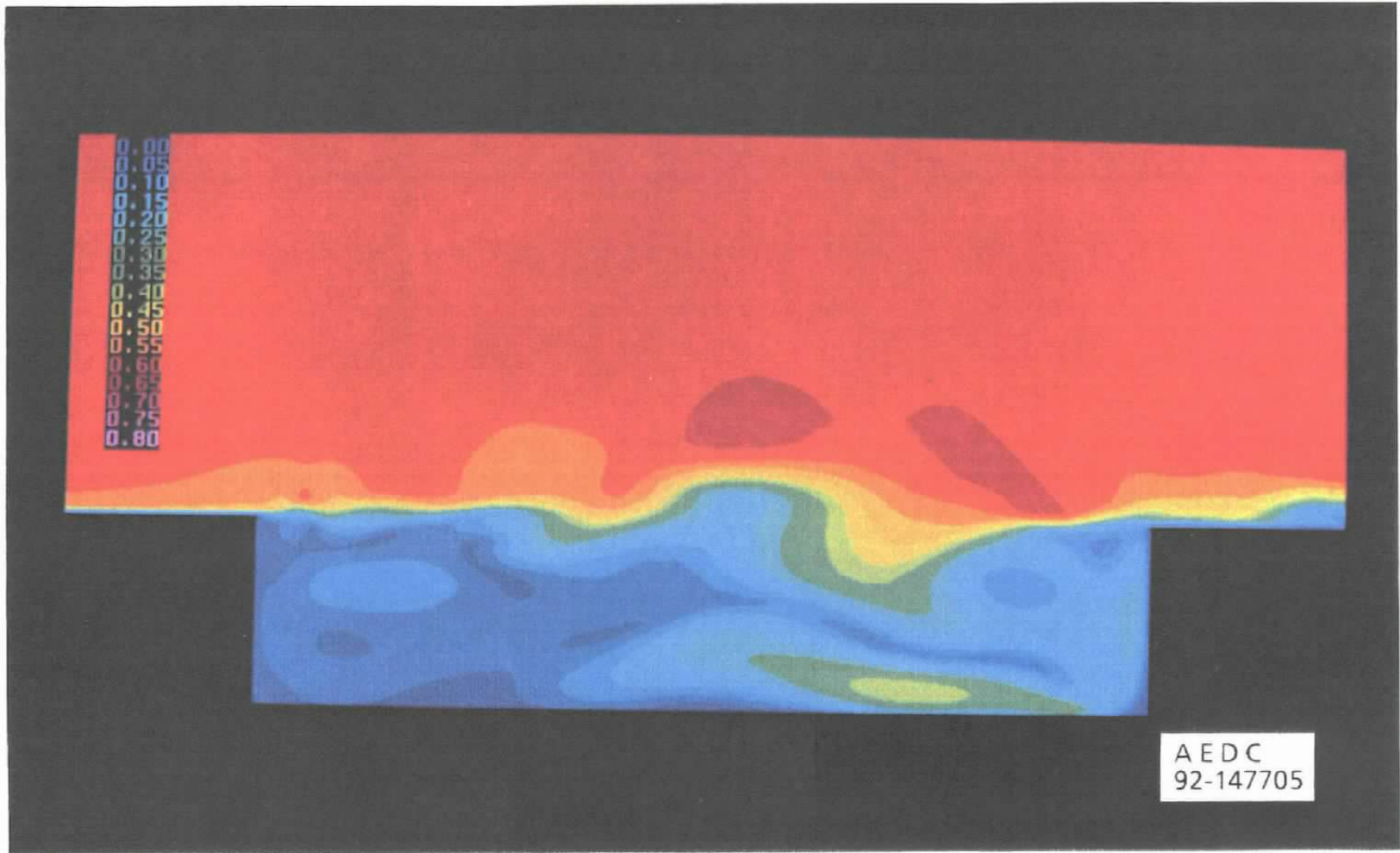
b. SPL on centerline, $Y/(W/2) = 0$

Figure 15. Comparisons of computations and measurements on the empty cavity walls, $M_\infty = 1.20$.

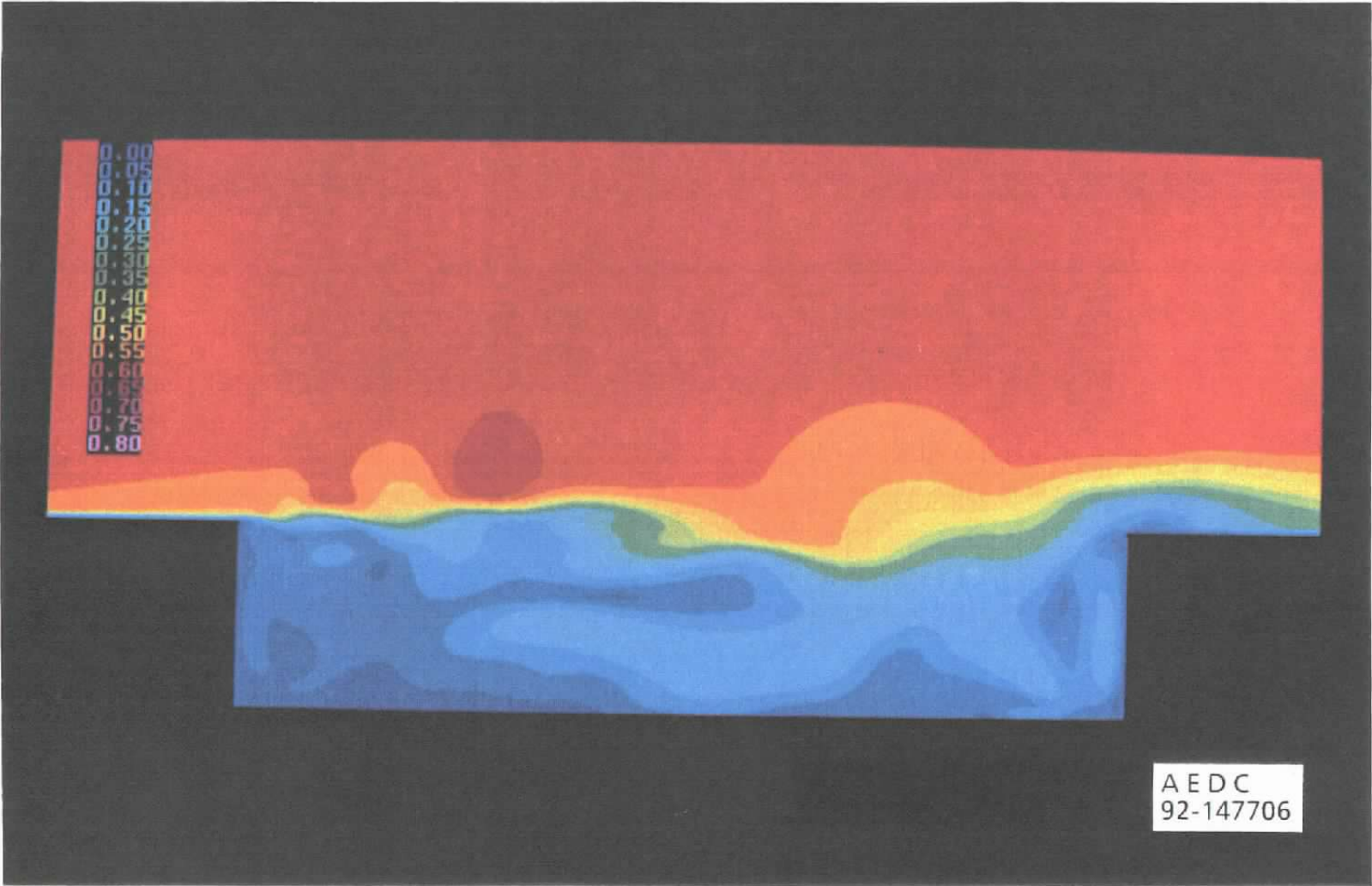


a. $t = 5.0t_c$

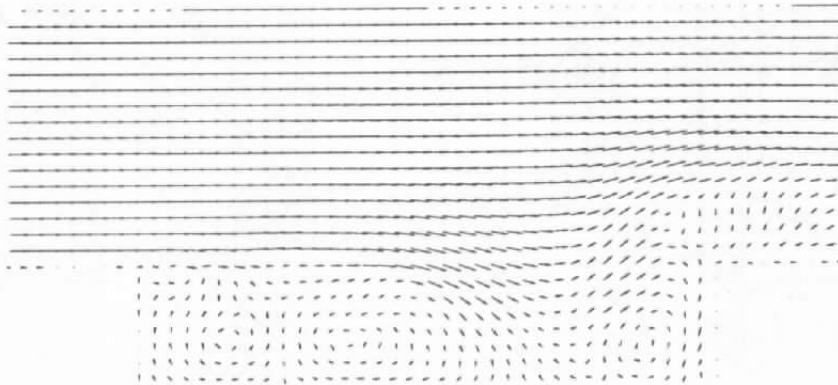
Figure 16. Mach number contours in the symmetry plane of the empty cavity, $M_\infty = 0.60$.



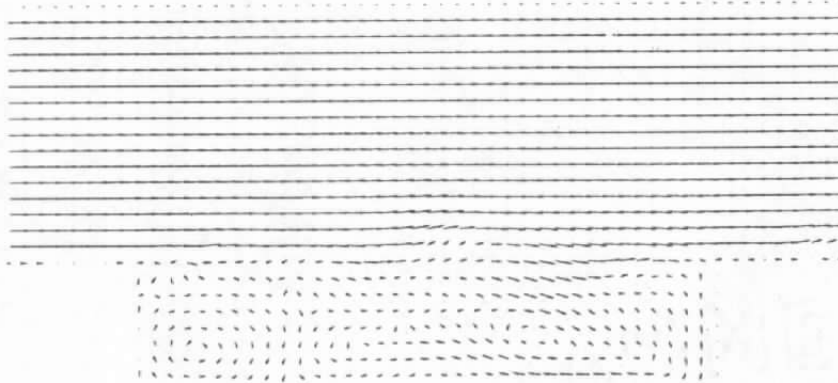
b. $t = 8.0t_c$
Figure 16. Continued.



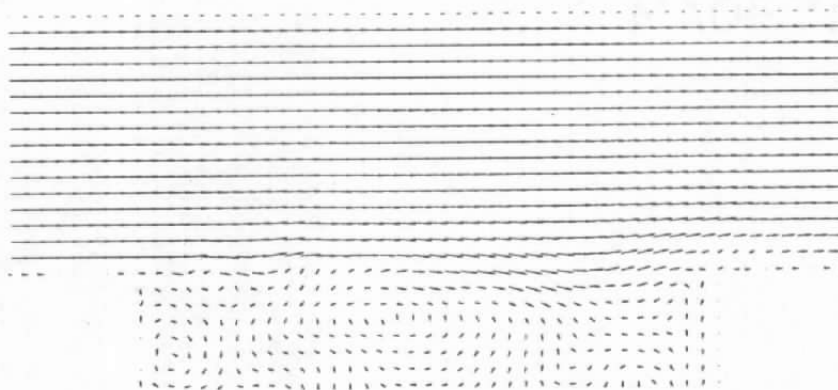
c. $t = 11.0t_c$
Figure 16. Concluded.



a. $t = 5.0t_c$

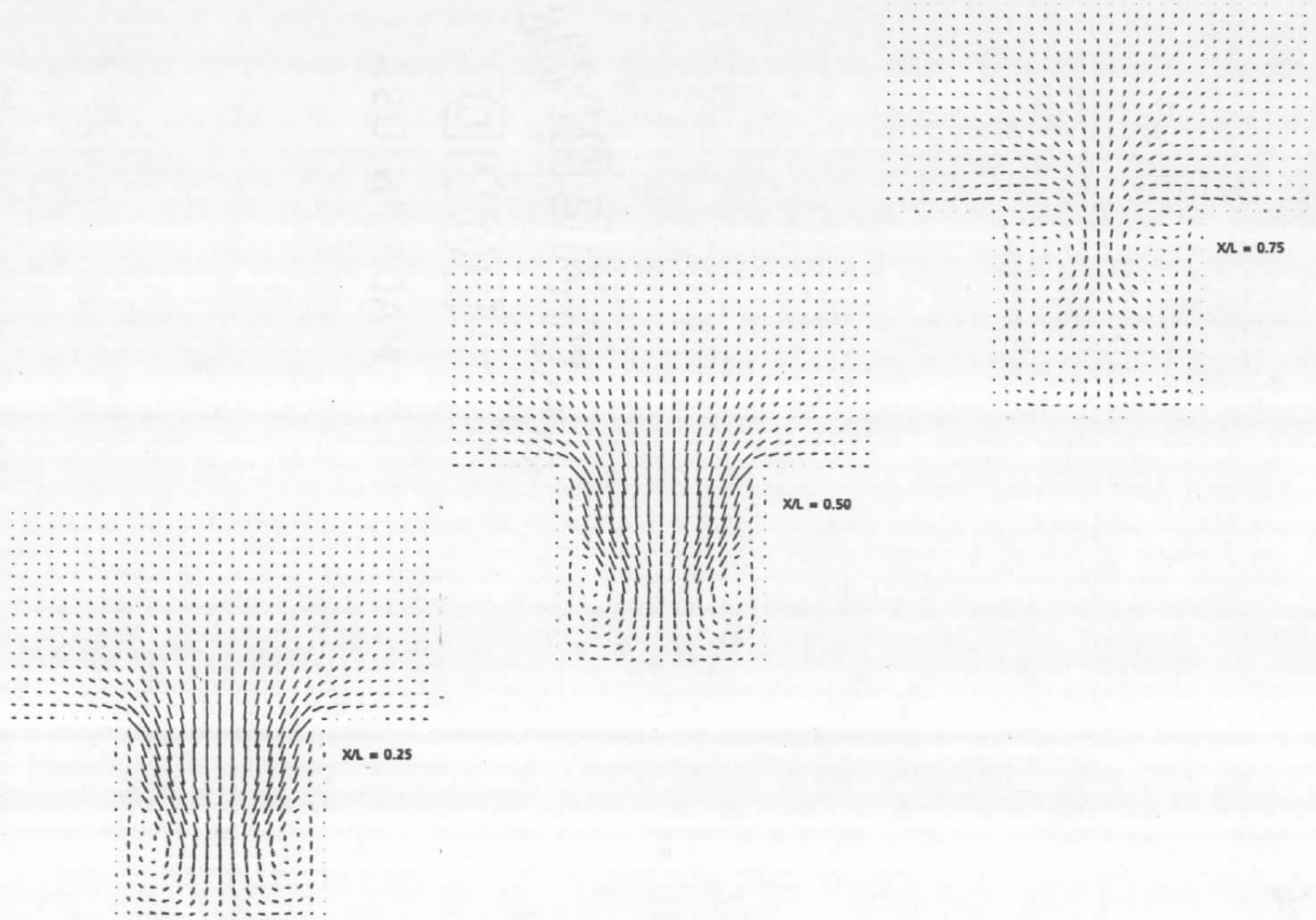


b. $t = 8.0t_c$



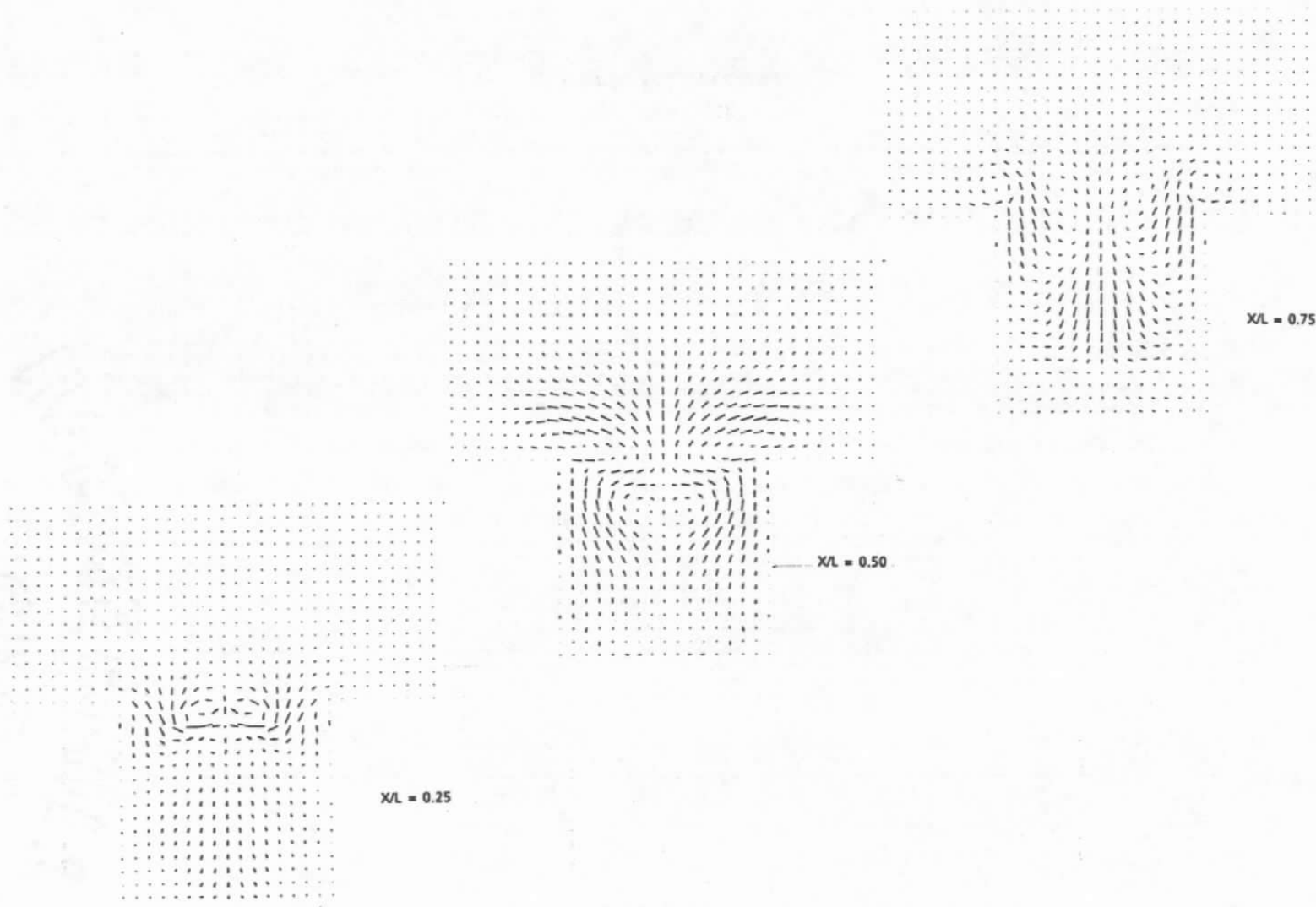
c. $t = 11.0t_c$

Figure 17. Velocity vectors in the symmetry plane of the empty cavity, $M_\infty = 0.60$.

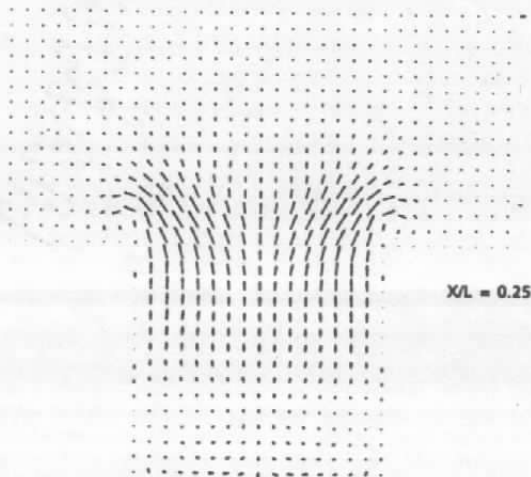
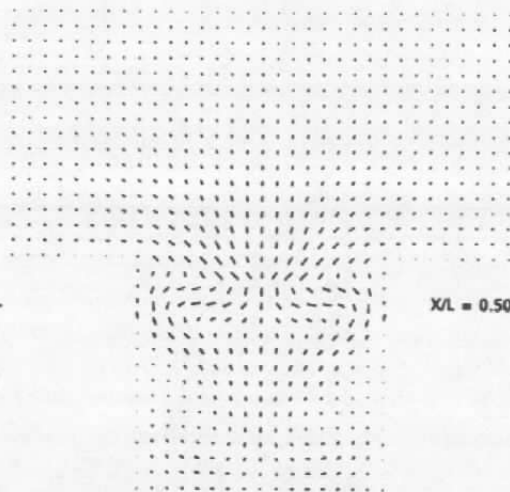
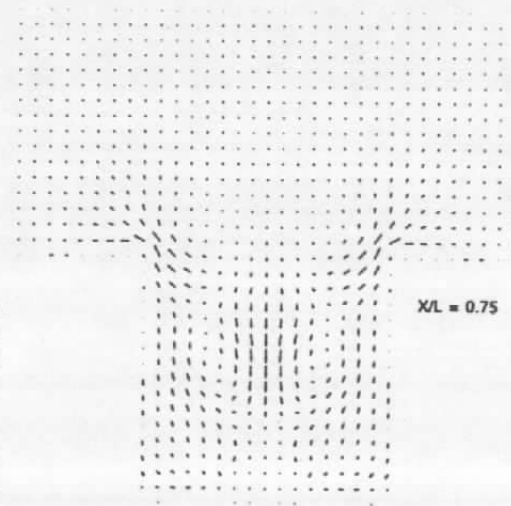


a. $t = 5.0t_c$

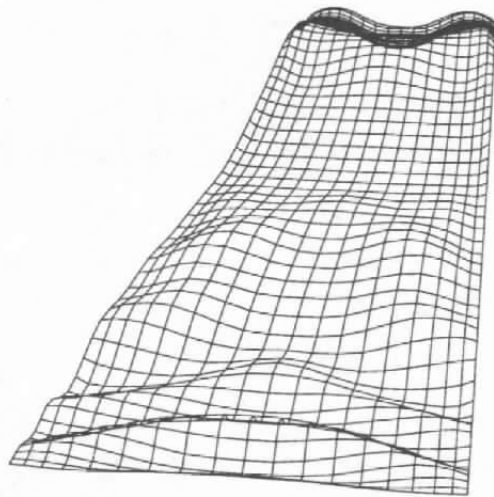
Figure 18. Velocity vectors in cross flow planes of the empty cavity, $M_\infty = 0.60$.



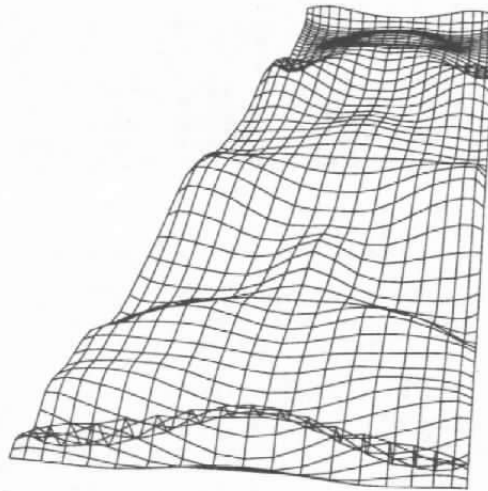
b. $t = 8.0t_c$
Figure 18. Continued.

 $X/L = 0.25$  $X/L = 0.50$  $X/L = 0.75$

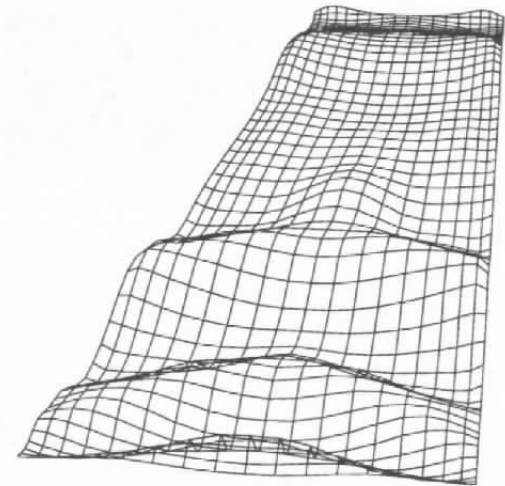
$c. t = 11.0t_c$
Figure 18. Concluded.



a. $t = 5.0t_c$

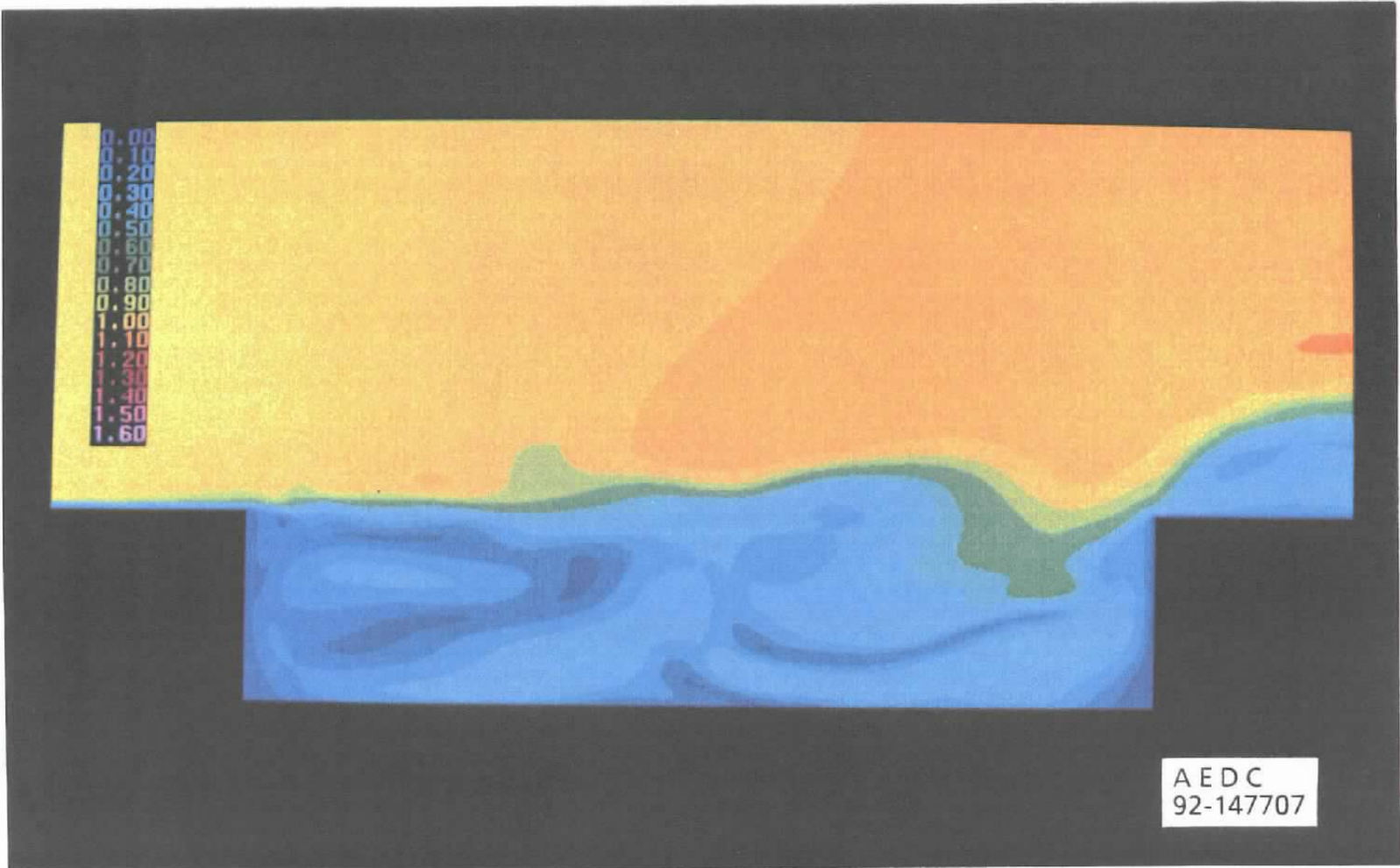


b. $t = 8.0t_c$



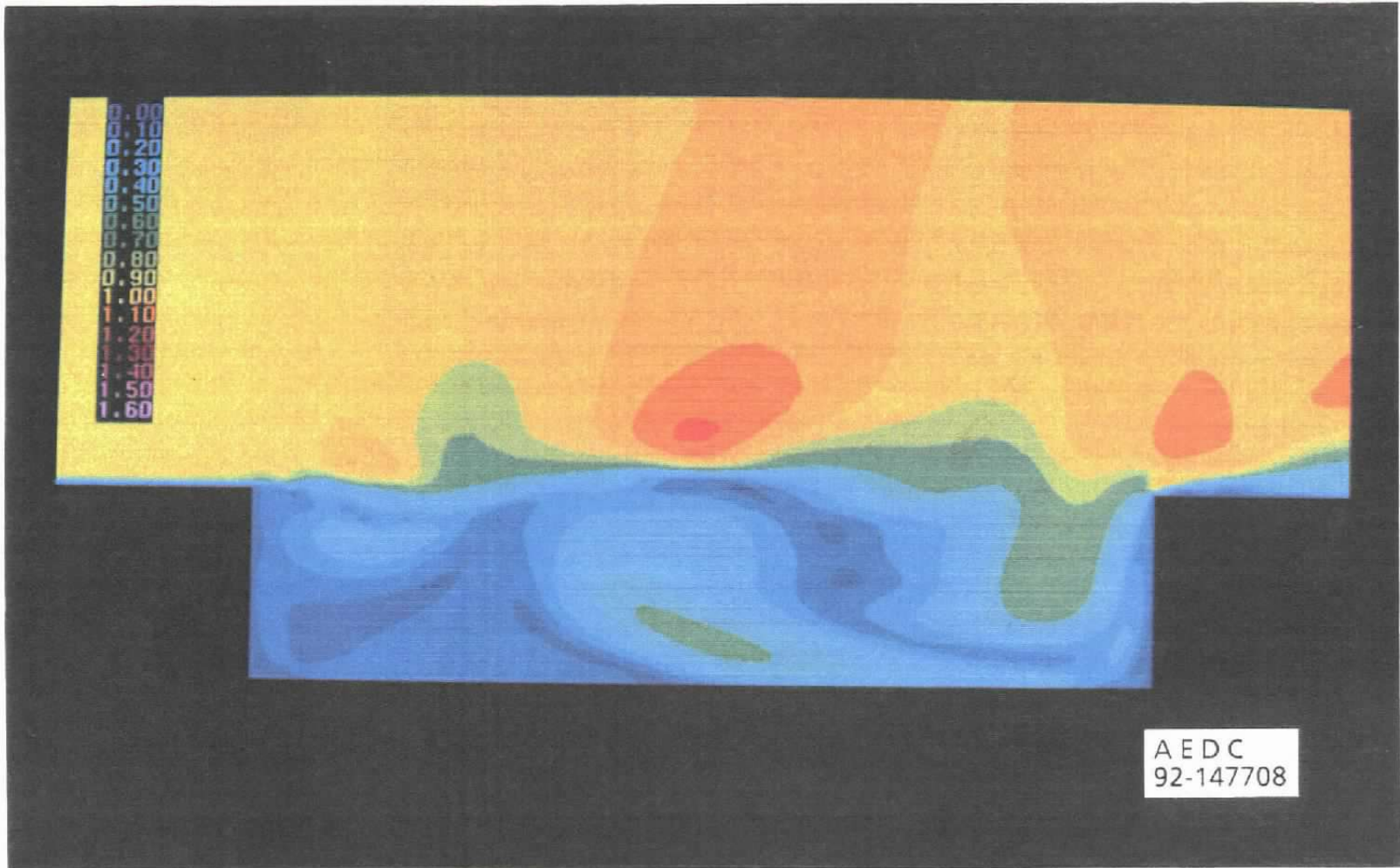
c. $t = 11.0t_c$

Figure 19. Mass flow through the opening of the empty cavity, $M_\infty = 0.60$.

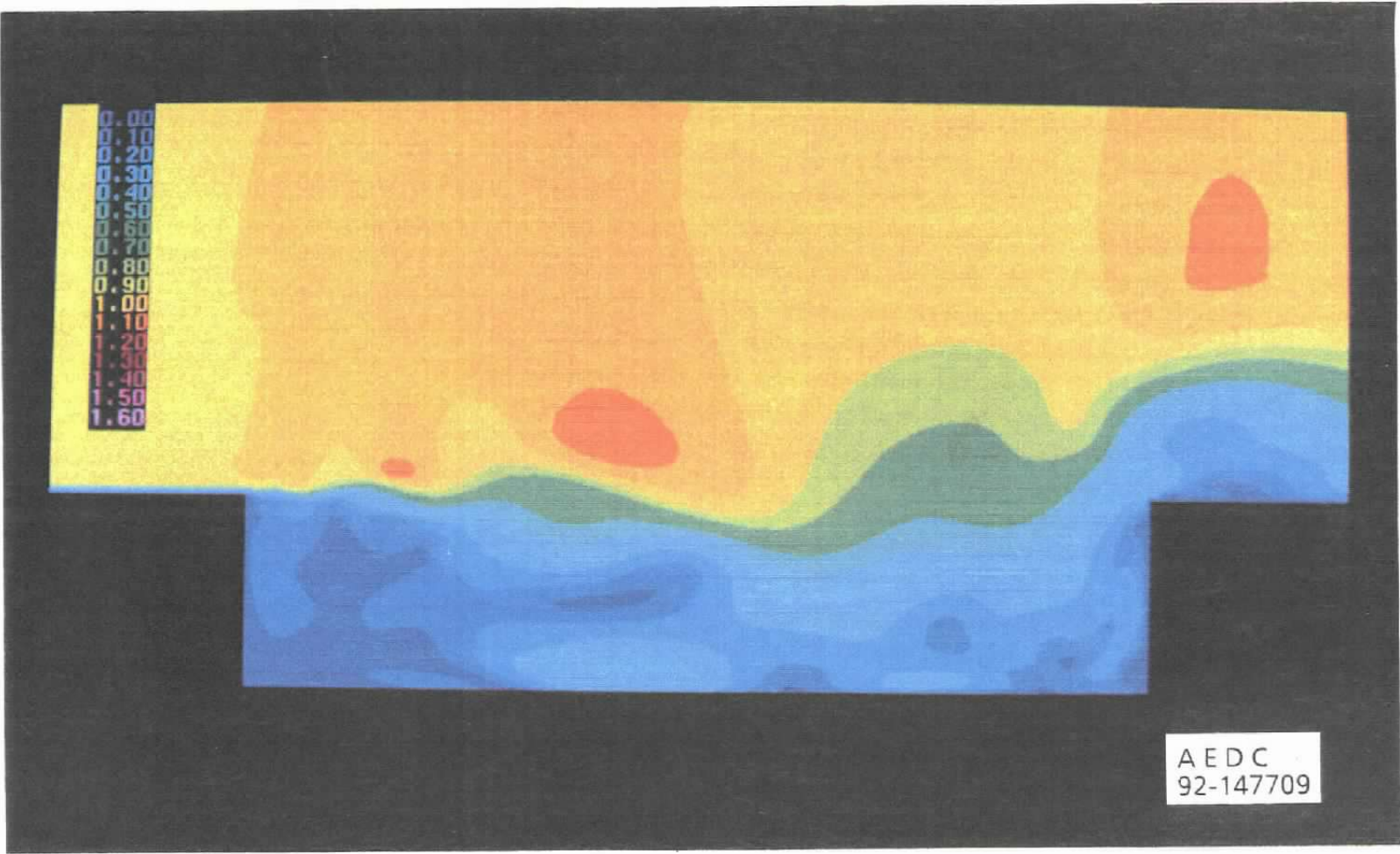


a. $t = 5.0t_c$

Figure 20. Mach number contours in the symmetry plane of the empty cavity, $M_\infty = 0.95$.

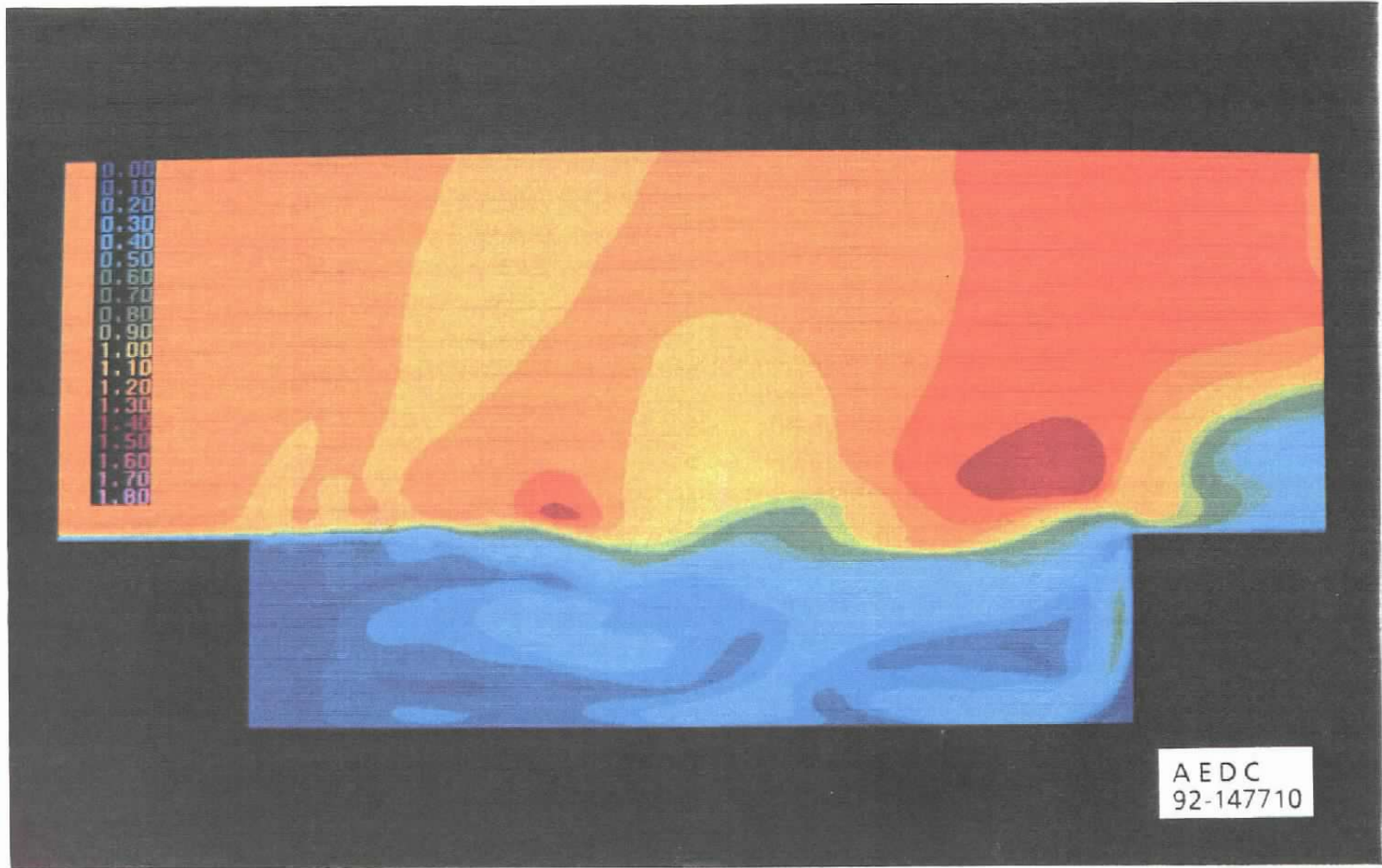


b. $t = 8.0t_c$
Figure 20. Continued.



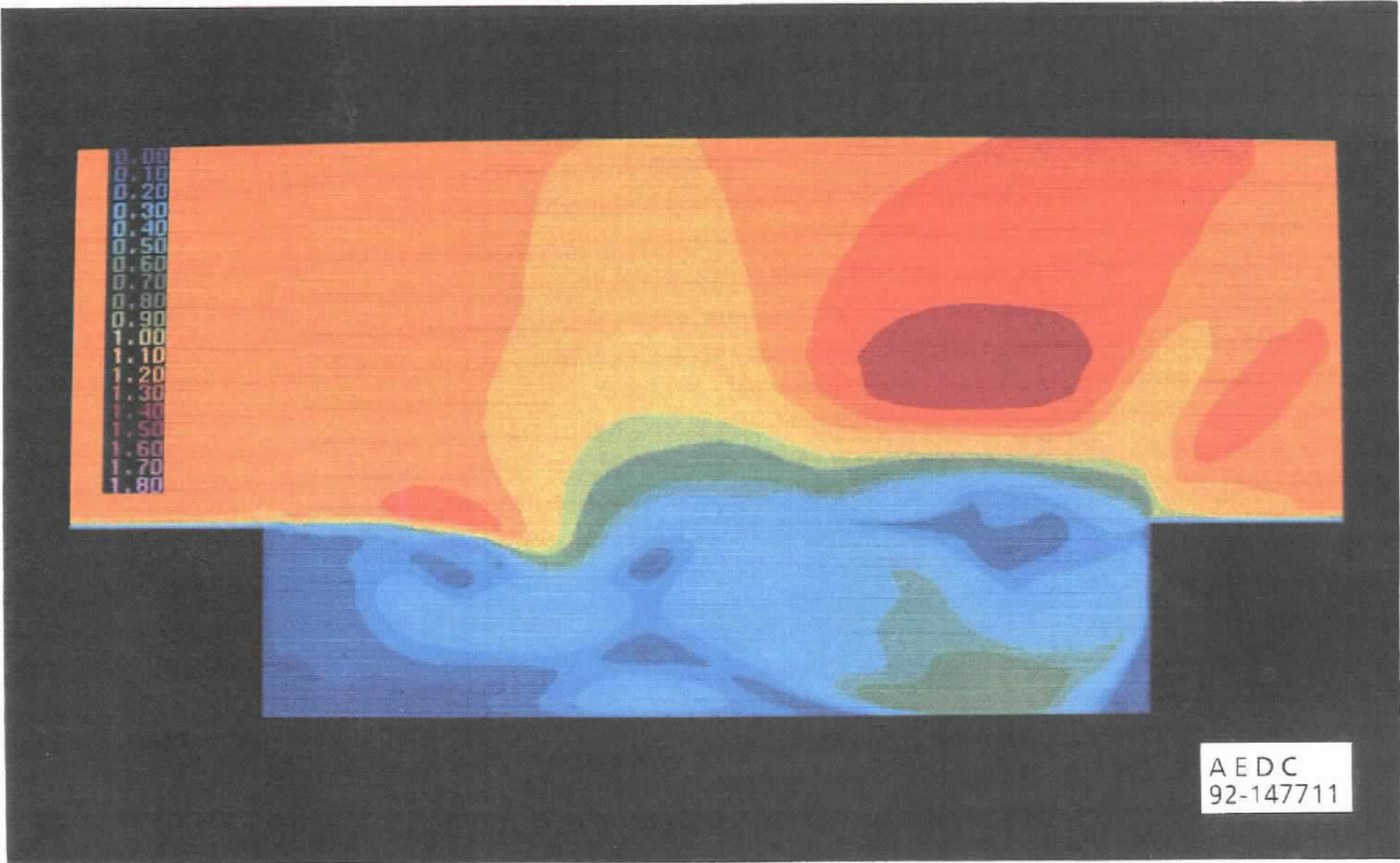
A E D C
92-147709

c. $t = 11.0t_c$
Figure 20. Concluded.

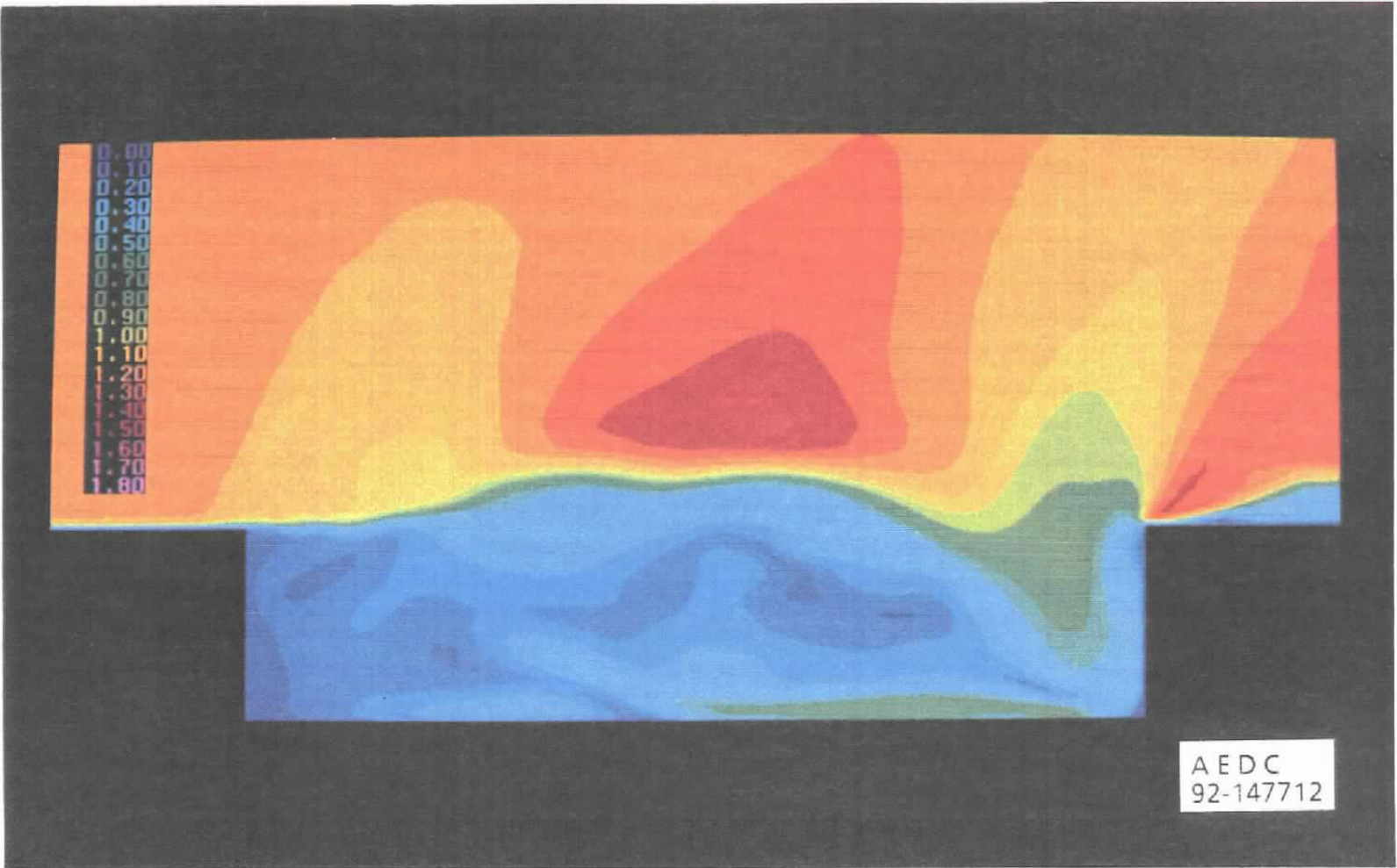


a. $t = 5.0t_c$

Figure 21. Mach number contours in the symmetry plane of the empty cavity, $M_\infty = 1.20$.



b. $t = 8.0t_c$
Figure 21. Continued.



c. $t = 11.0t_c$
Figure 21. Concluded.

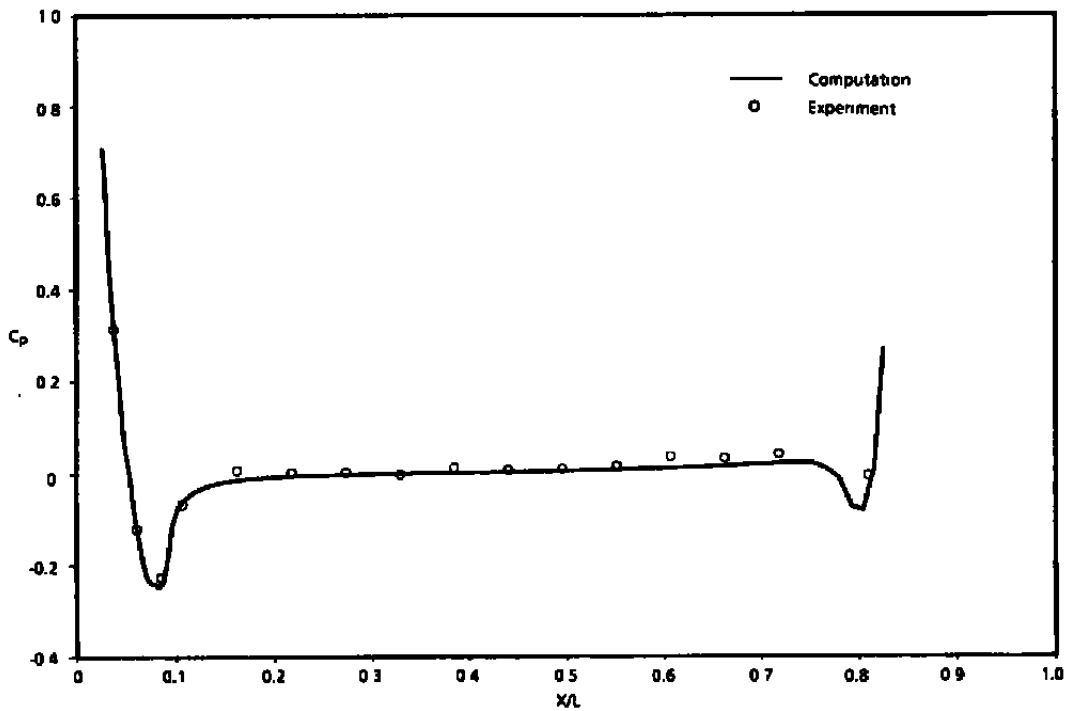
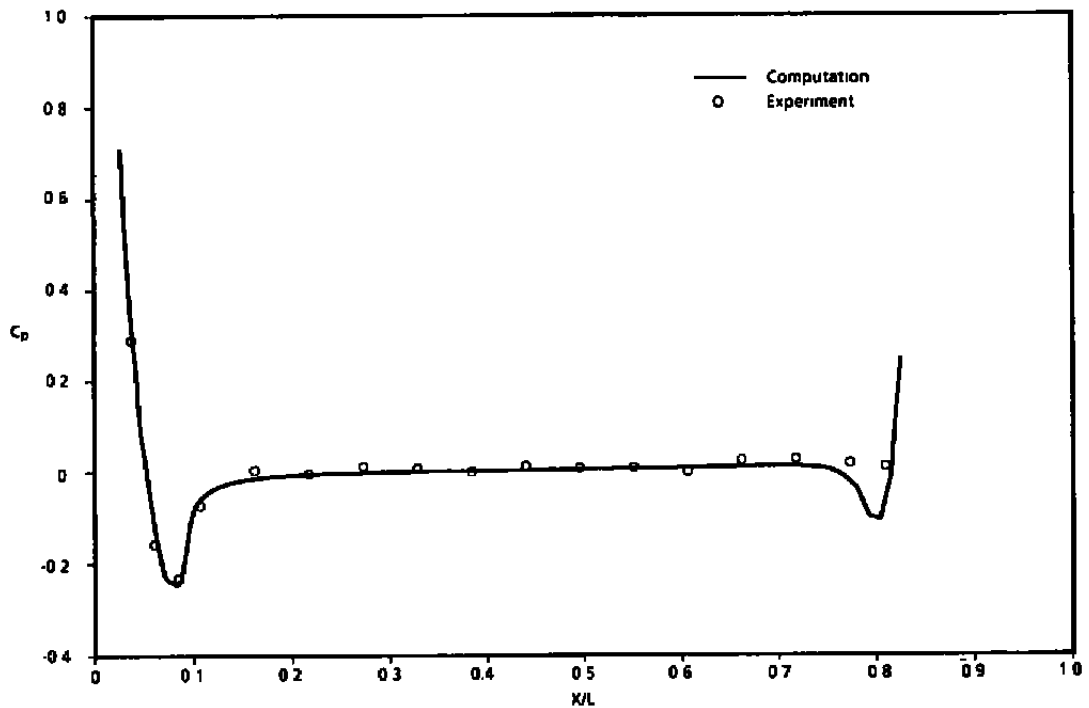
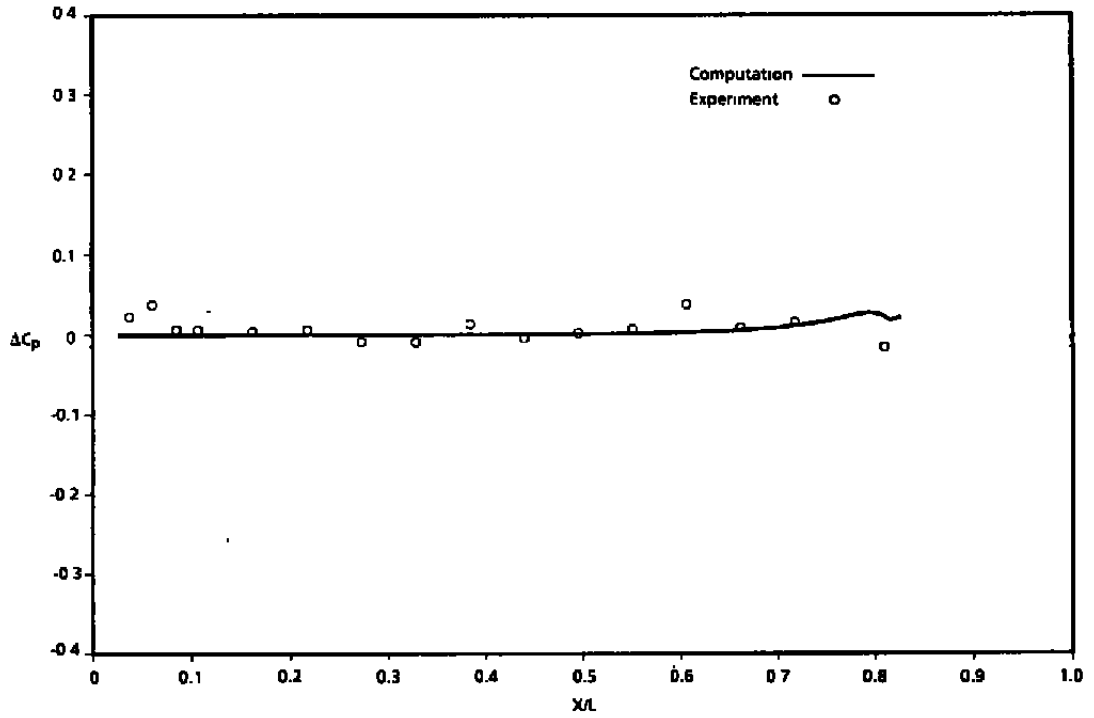
a. C_p on free-stream sideb. C_p on cavity side

Figure 22. Comparisons of computations and measurements on the store/sting in a free-stream flow, $M_\infty = 0.60$.



c. ΔC_p
Figure 22. Concluded.

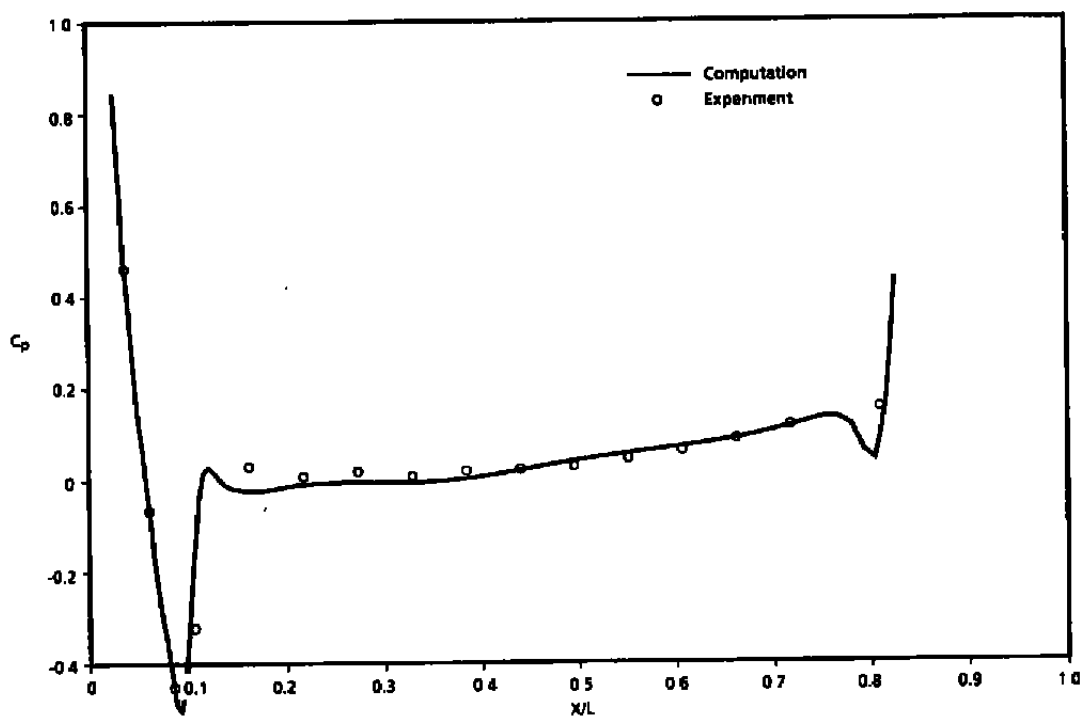
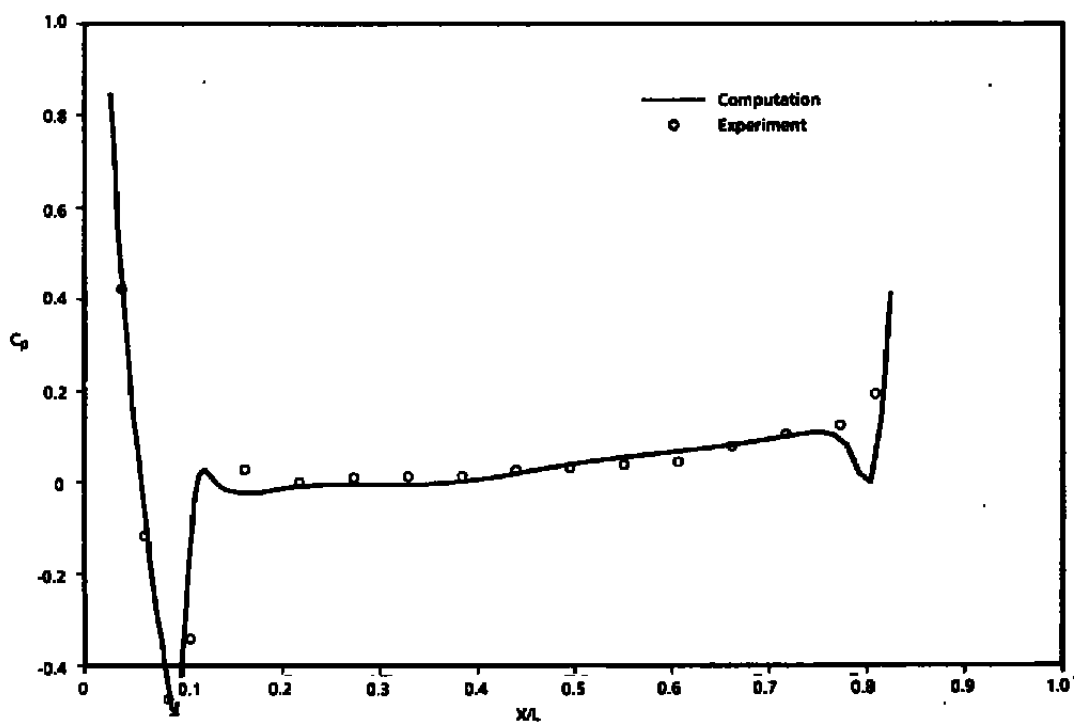
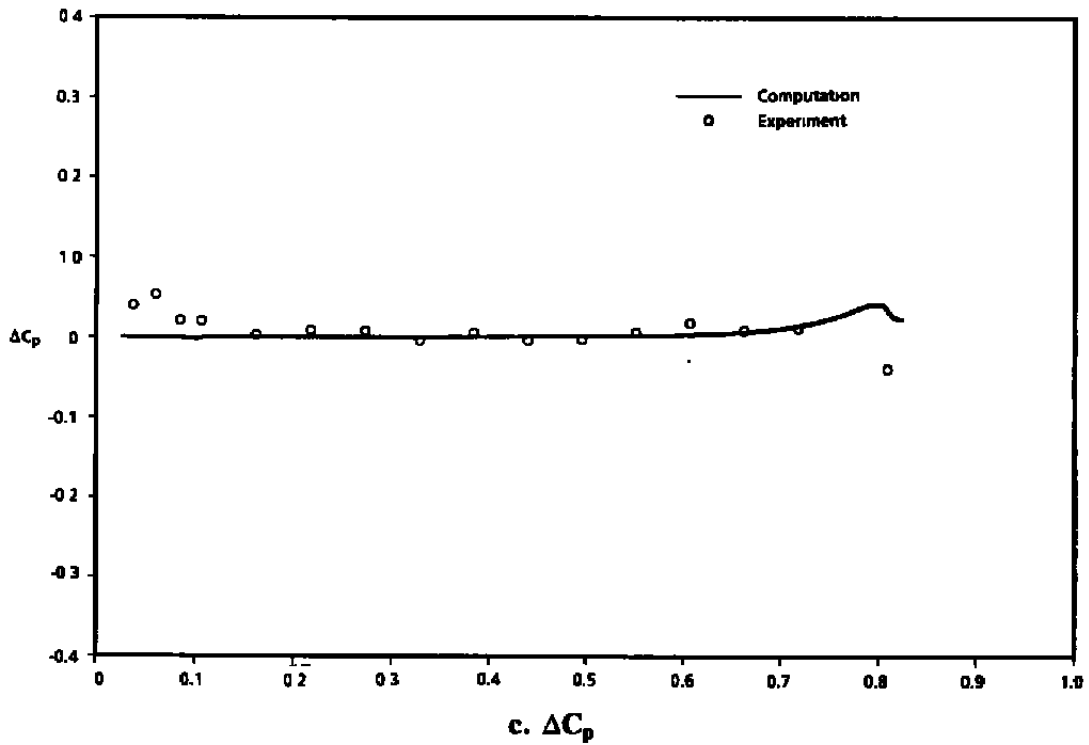
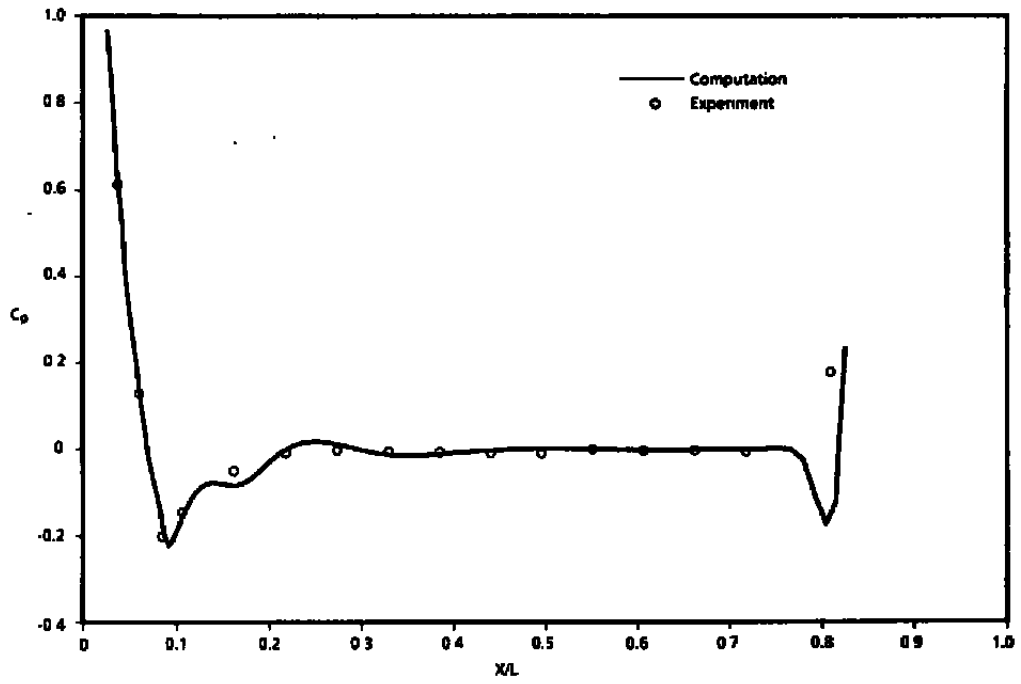
a. C_p on free-stream sideb. C_p on cavity side

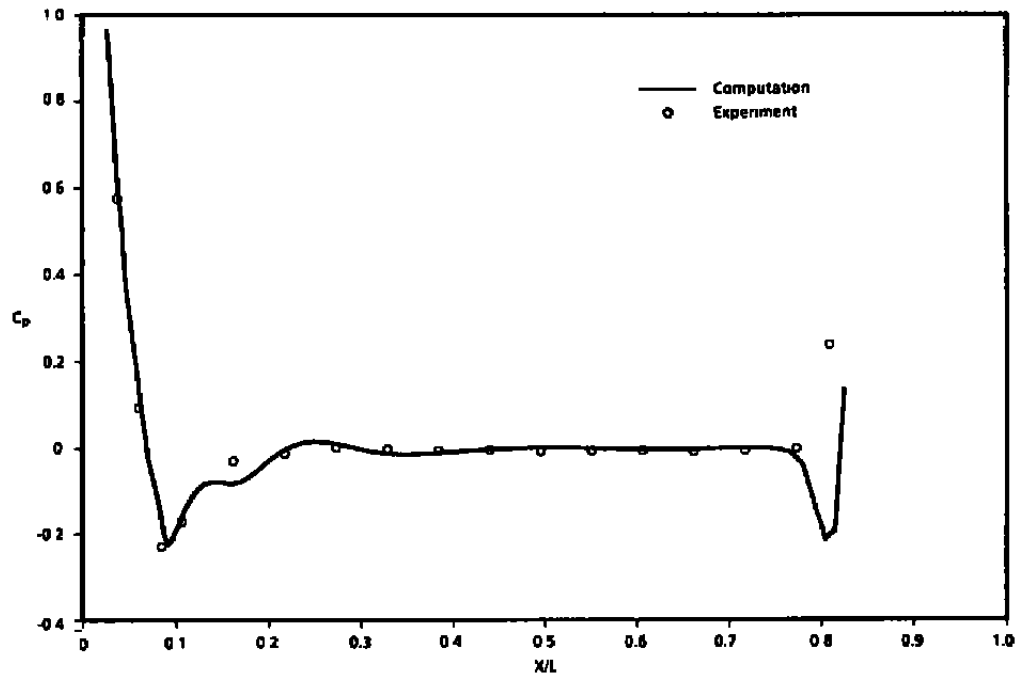
Figure 23. Comparisons of computations and measurements on the store/sting in a free-stream flow, $M_\infty = 0.95$.



$c. \Delta C_p$
Figure 23. Concluded.

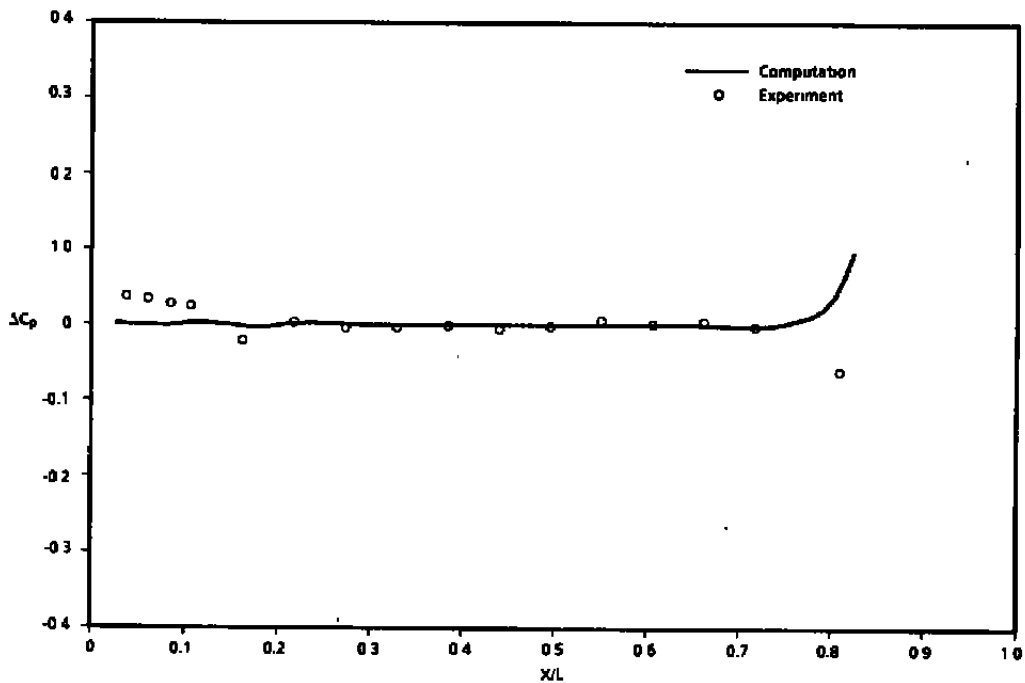


a. C_p on free-stream side



b. C_p on cavity side

Figure 24. Comparisons of computations and measurements on the store/sting in a free-stream flow, $M_\infty = 1.20$.



c. ΔC_p
Figure 24. Concluded.

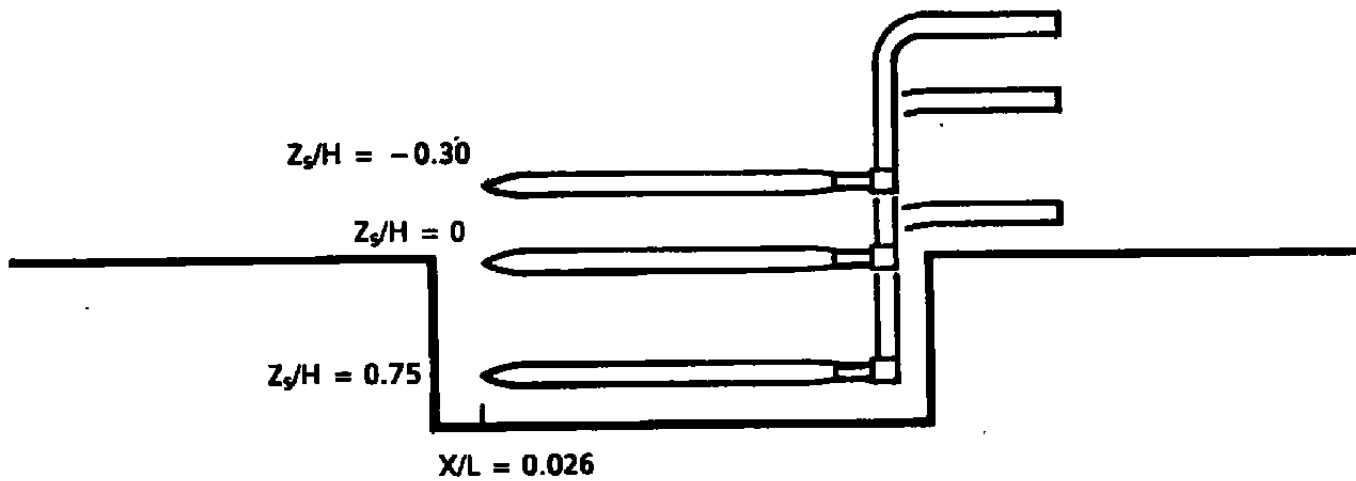
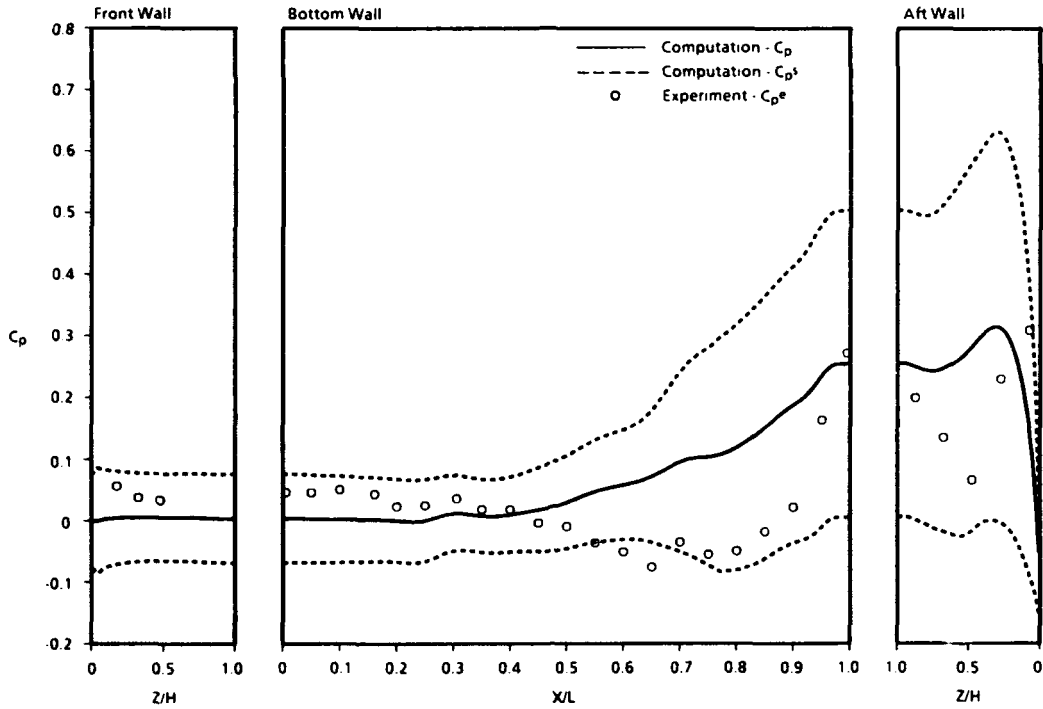
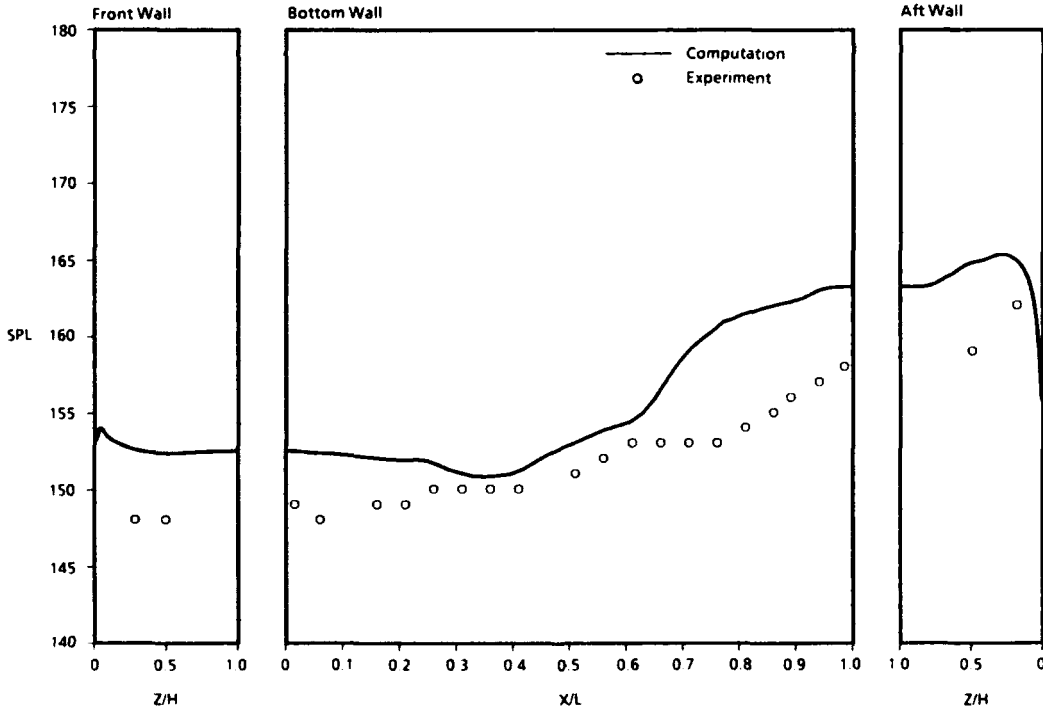


Figure 25. Store/sting locations within the cavity.

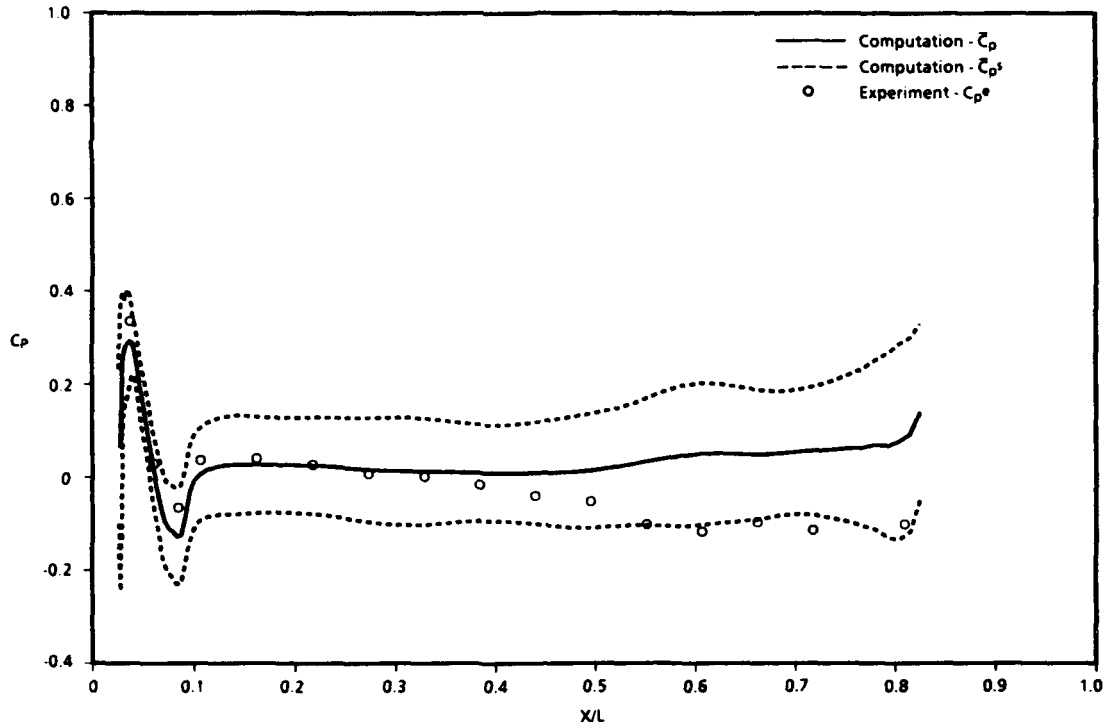


a. C_p on centerline, $Y/(W/2) = 0$

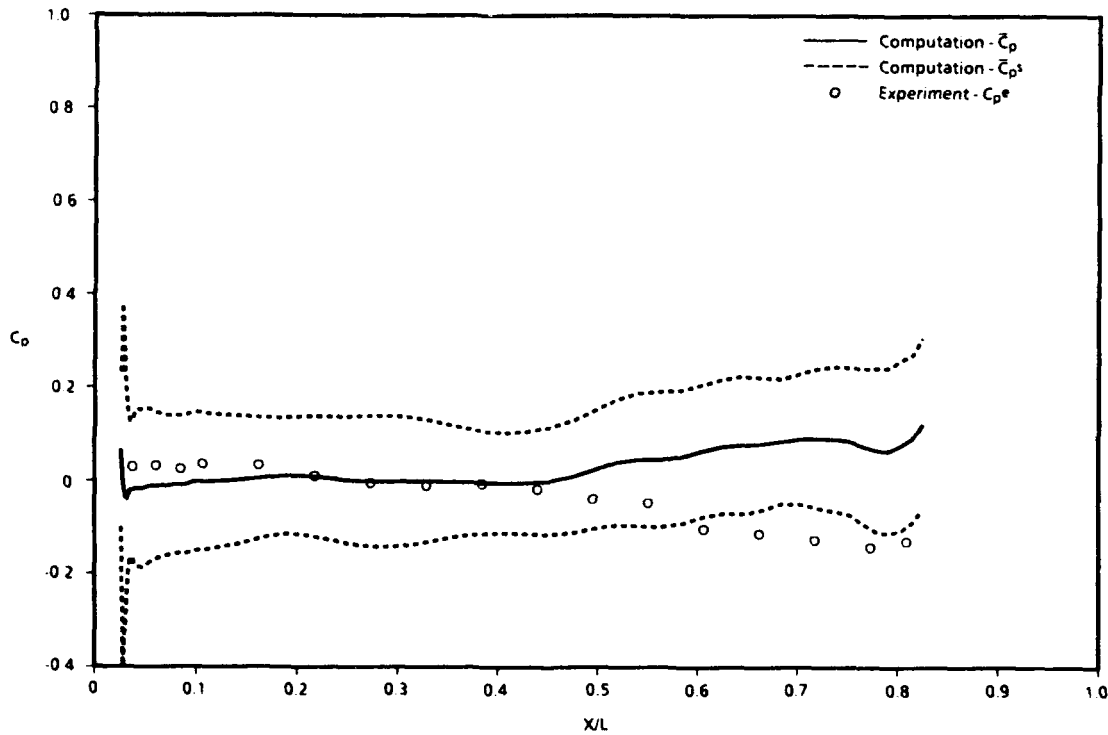


b. SPL on centerline, $Y/(W/2) = 0$

Figure 26. Comparisons of computations and measurements on the cavity walls with the store/sting present, $M_\infty = 0.60$, $Z_s/H = 0$.

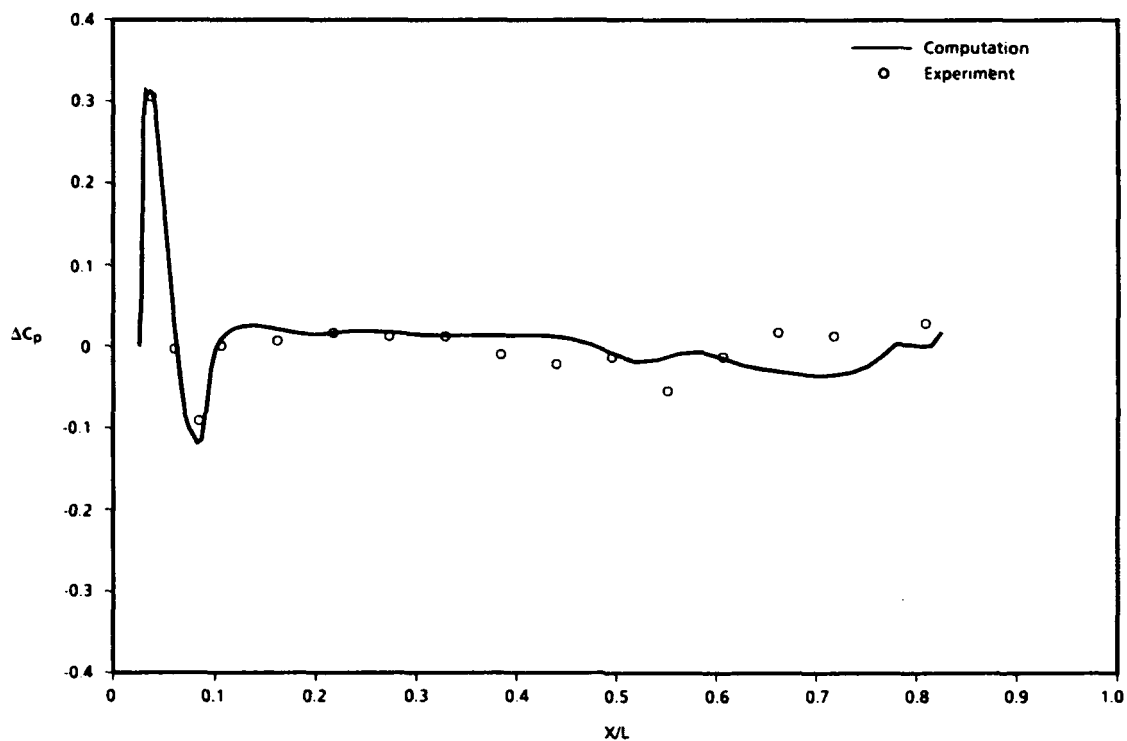


a. C_p on free-stream side

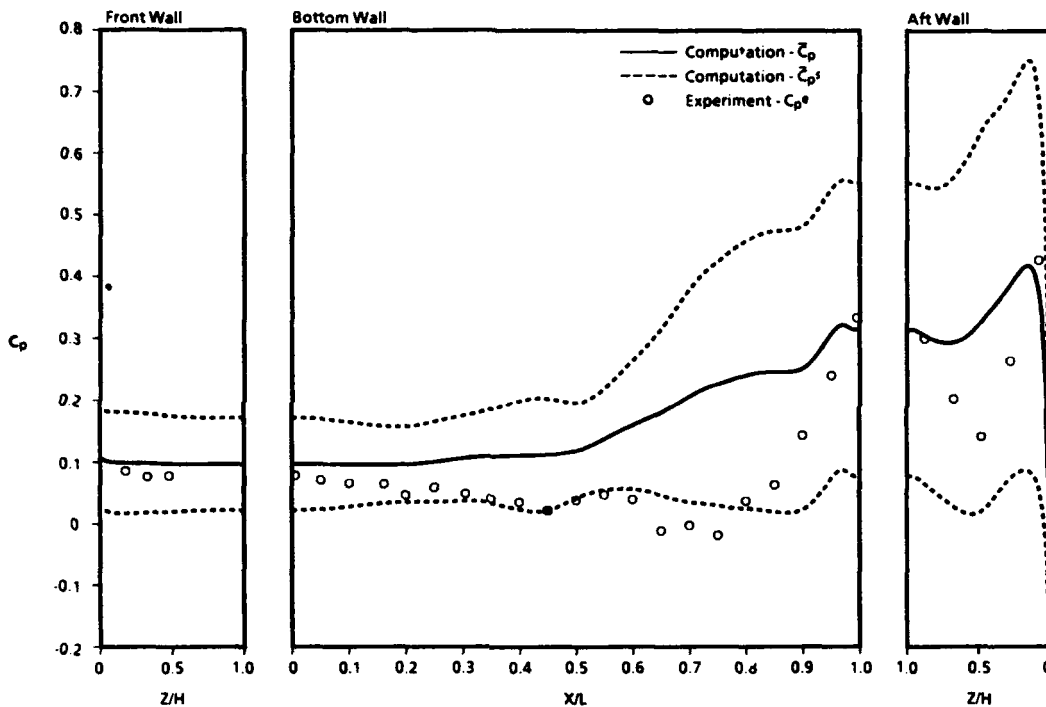


b. C_p on cavity side

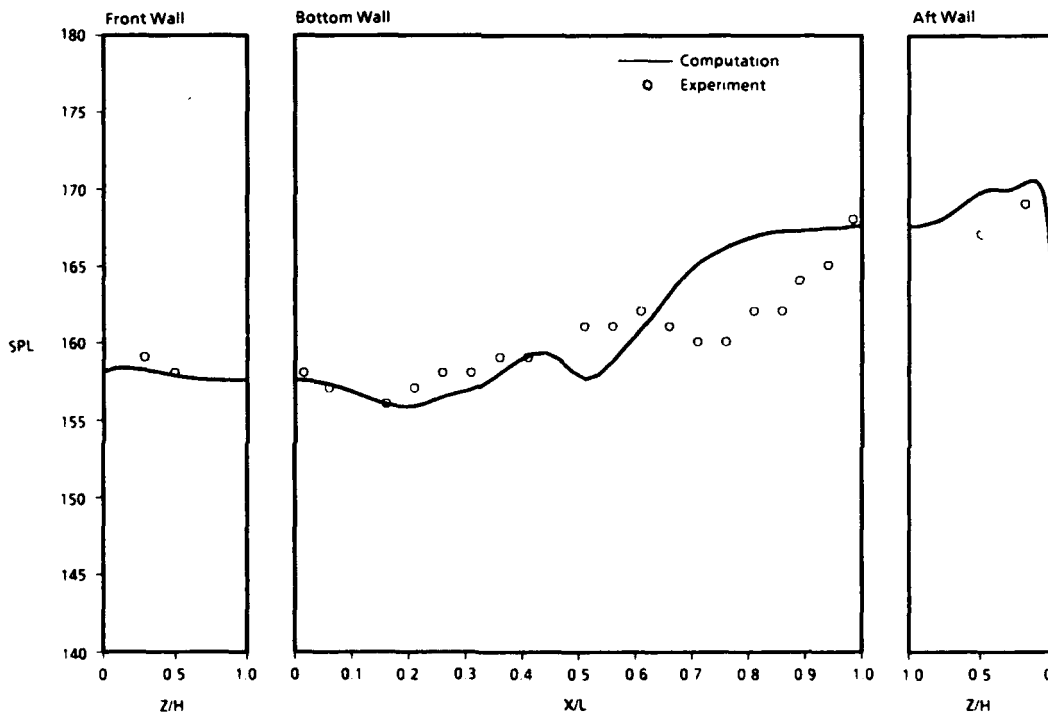
Figure 27. Comparisons of computations and measurements on the store/sting in the cavity, $M_\infty = 0.60$, $Z_s/H = 0$.



c. ΔC_p
Figure 27. Concluded.

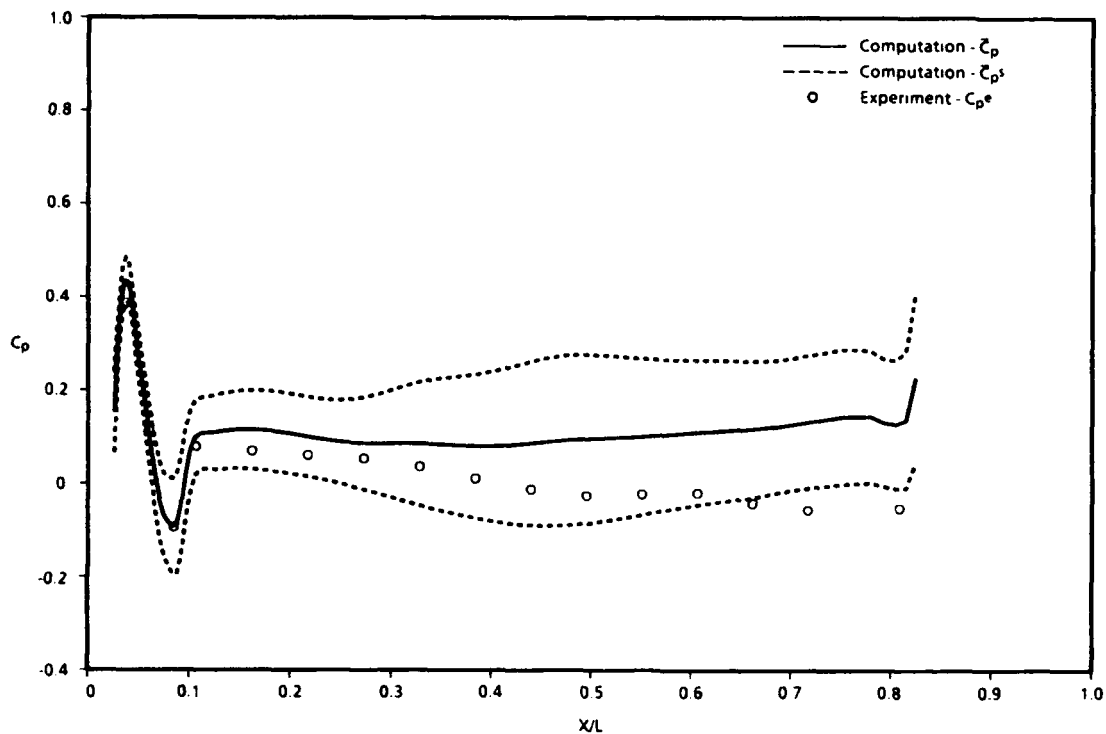


a. C_p on centerline, $Y/(W/2) = 0$

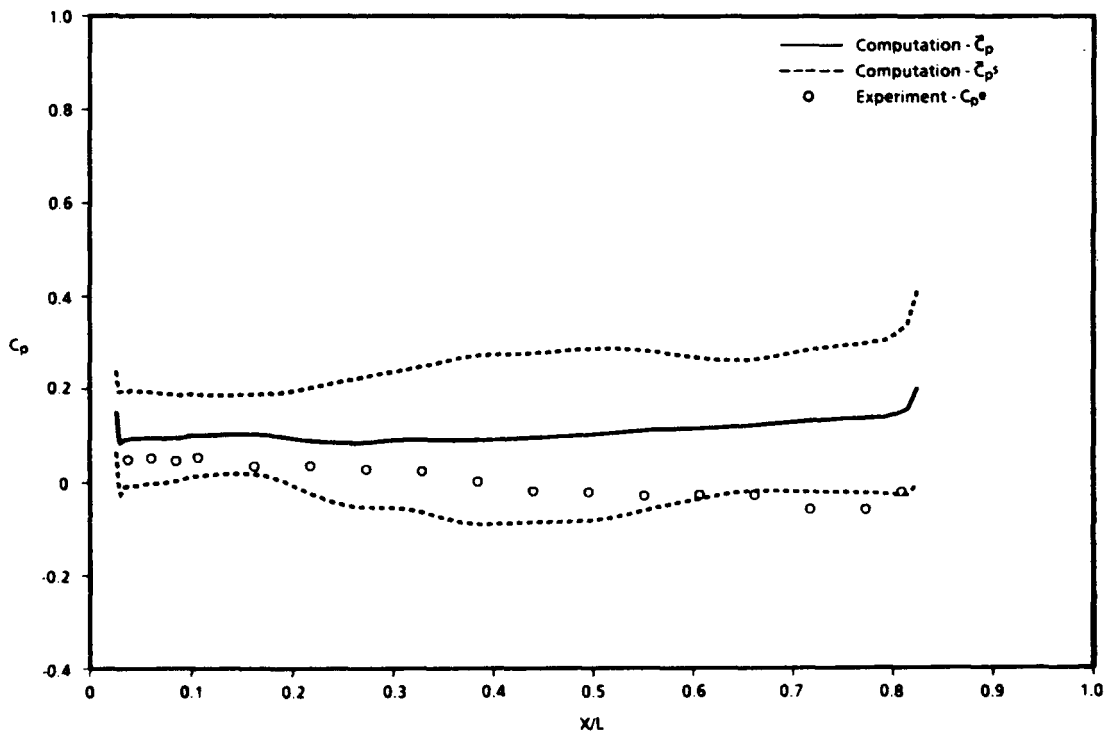


b. SPL on centerline, $Y/(W/2) = 0$

Figure 28. Comparisons of computations and measurements on the cavity walls with the store/sling present, $M_\infty = 0.95$, $Z_s/H = 0$.

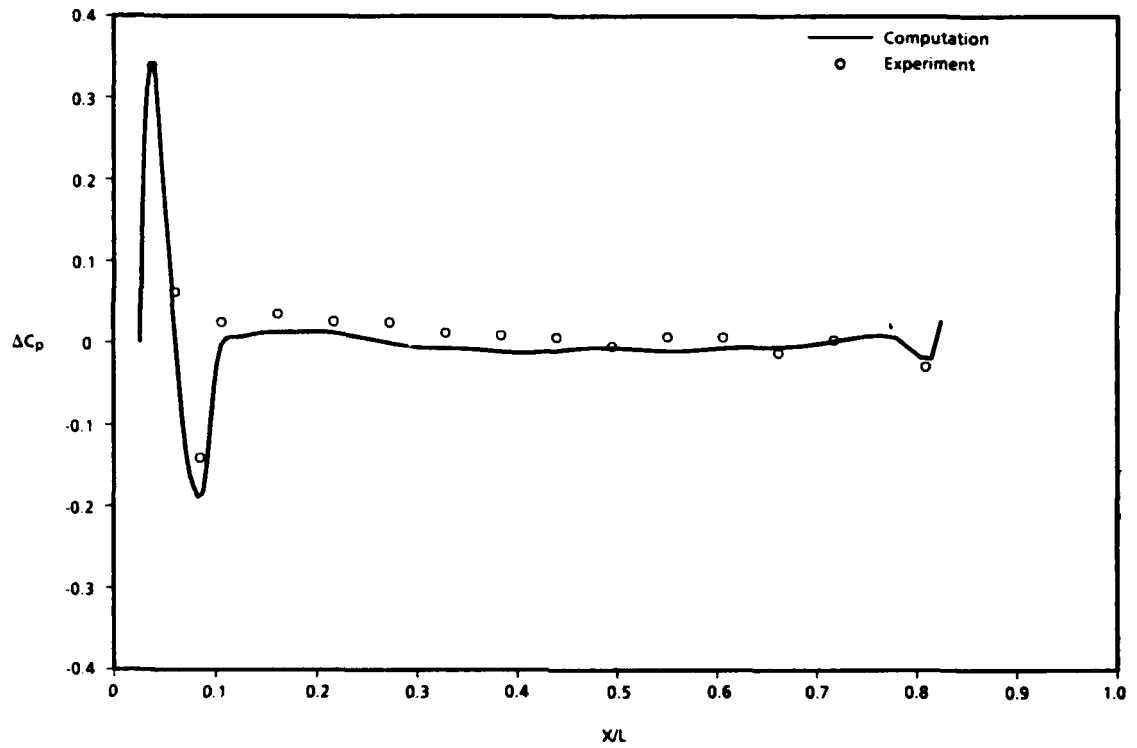


a. C_p on free-stream side

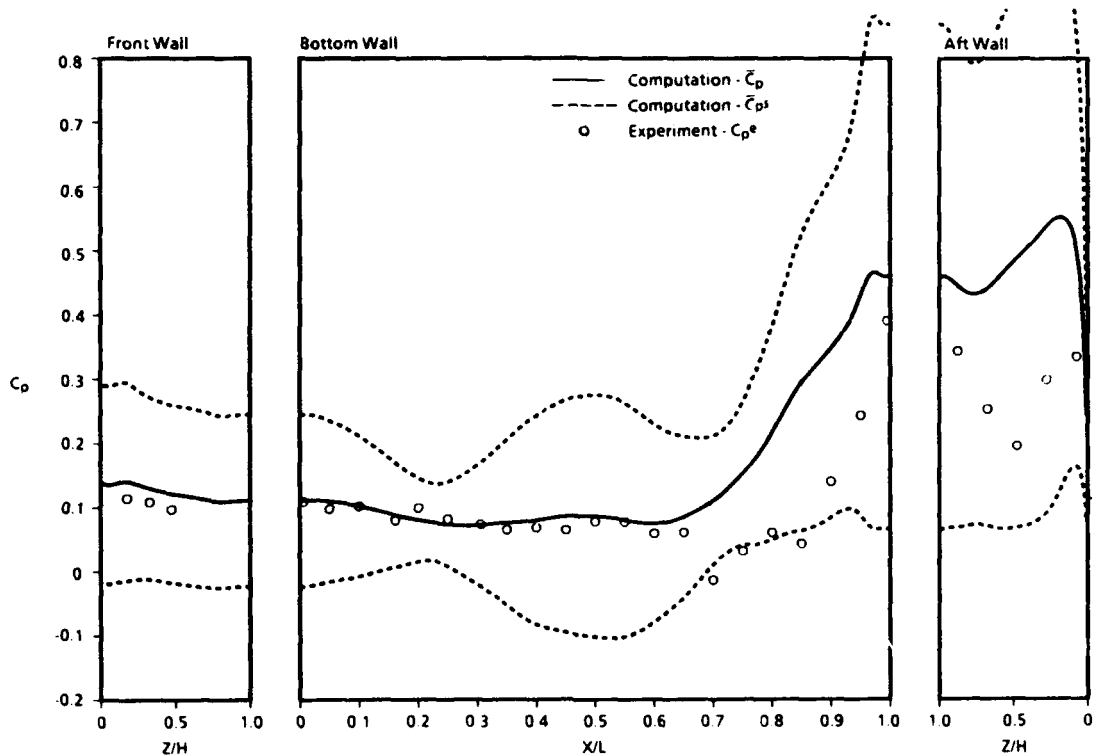


b. C_p on cavity side

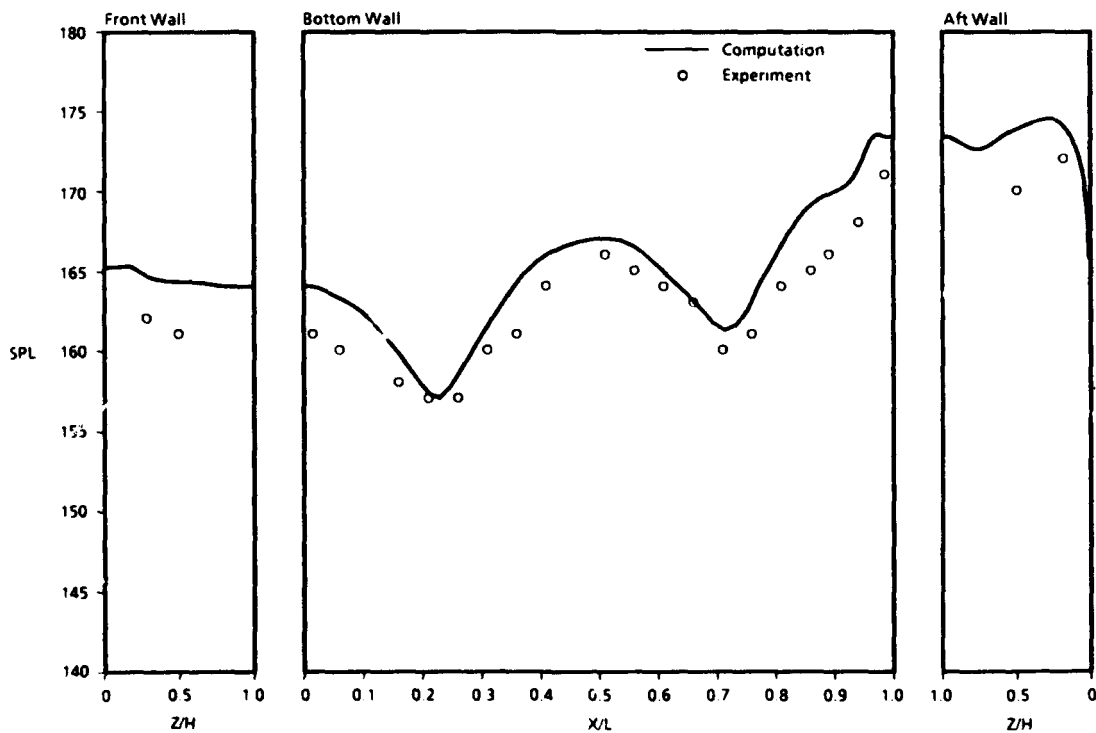
Figure 29. Comparisons of computations and measurements on the store/sting in the cavity, $M_\infty = 0.95$, $Z_s/H = 0$.



c. ΔC_p
Figure 29. Concluded.

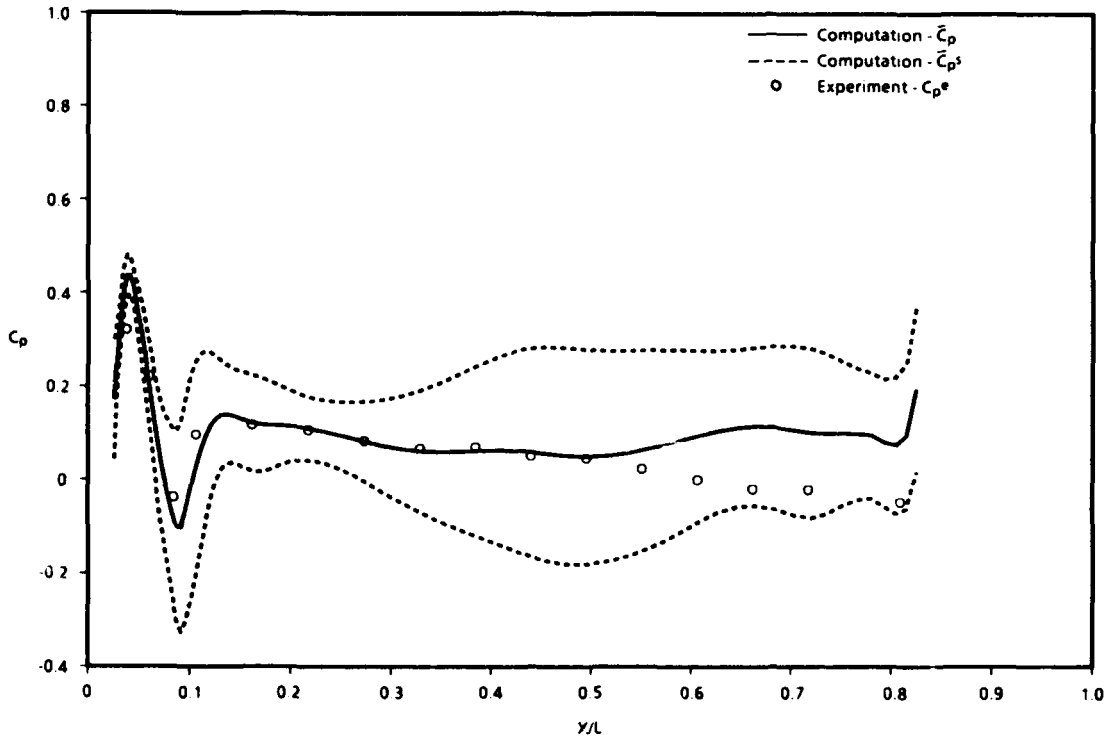


a. C_p on centerline, $Y/(W/2) = 0$

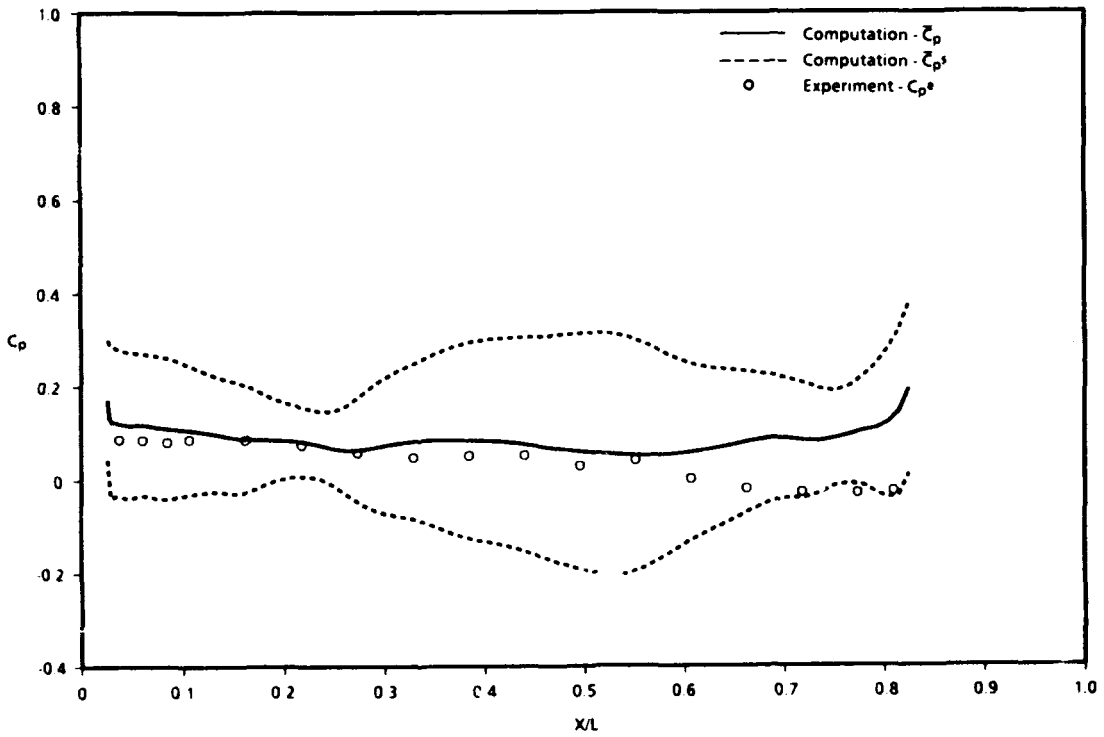


b. SPL on centerline, $Y/(W/2) = 0$

Figure 30. Comparisons of computations and measurements on the cavity walls with the store/sting present, $M_\infty = 1.20$, $Z_s/H = 0$.

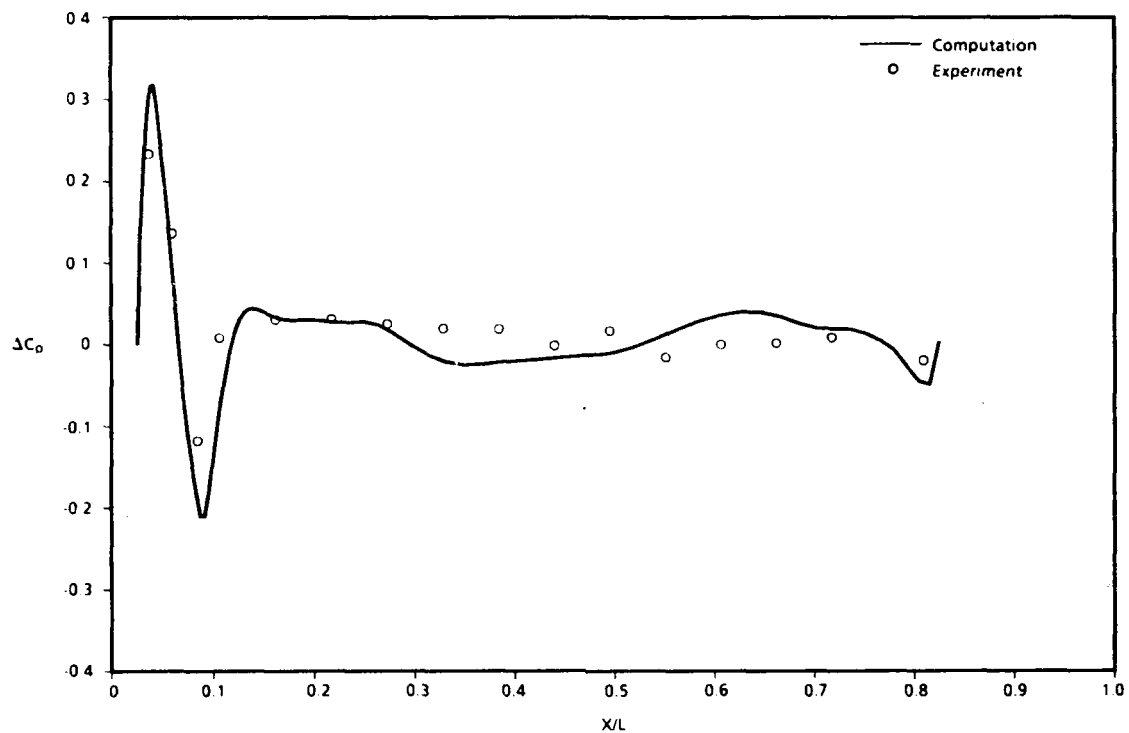


a. C_p on free-stream side

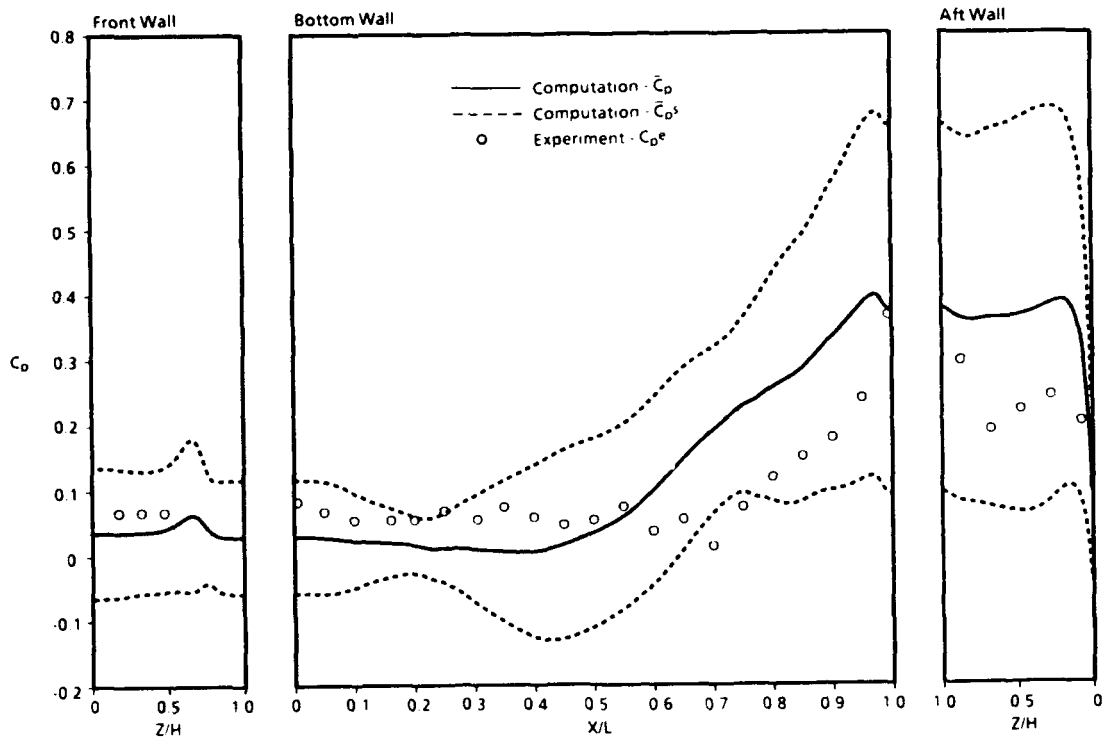


b. C_p on cavity side

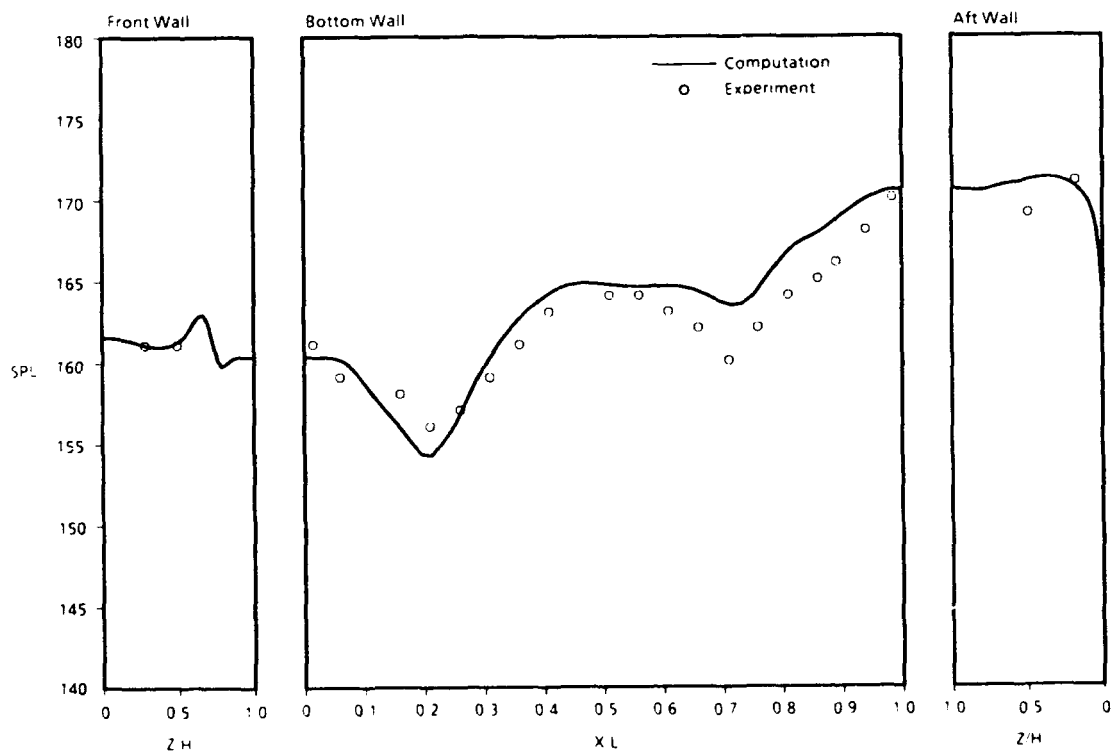
Figure 31. Comparisons of computations and measurements on the store/sting in the cavity, $M_\infty = 1.20$, $Z_s/H = 0$.



c. ΔC_p
Figure 31. Concluded.

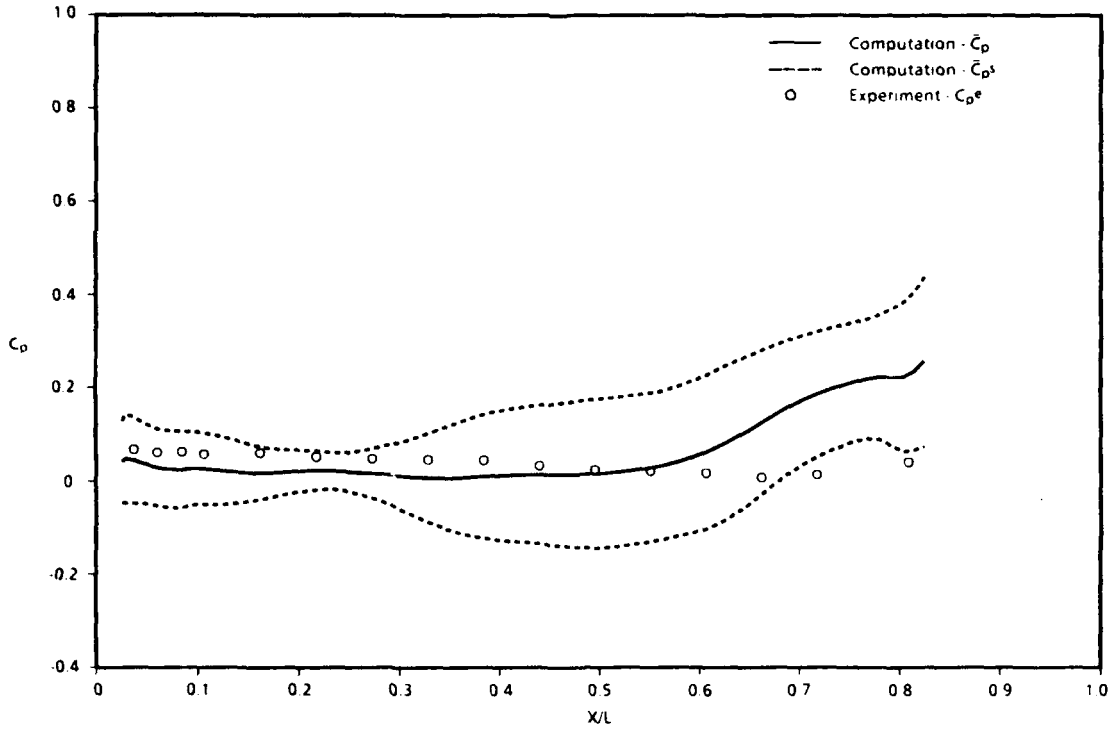


a. C_p on centerline, $Y/(W/2) = 0$

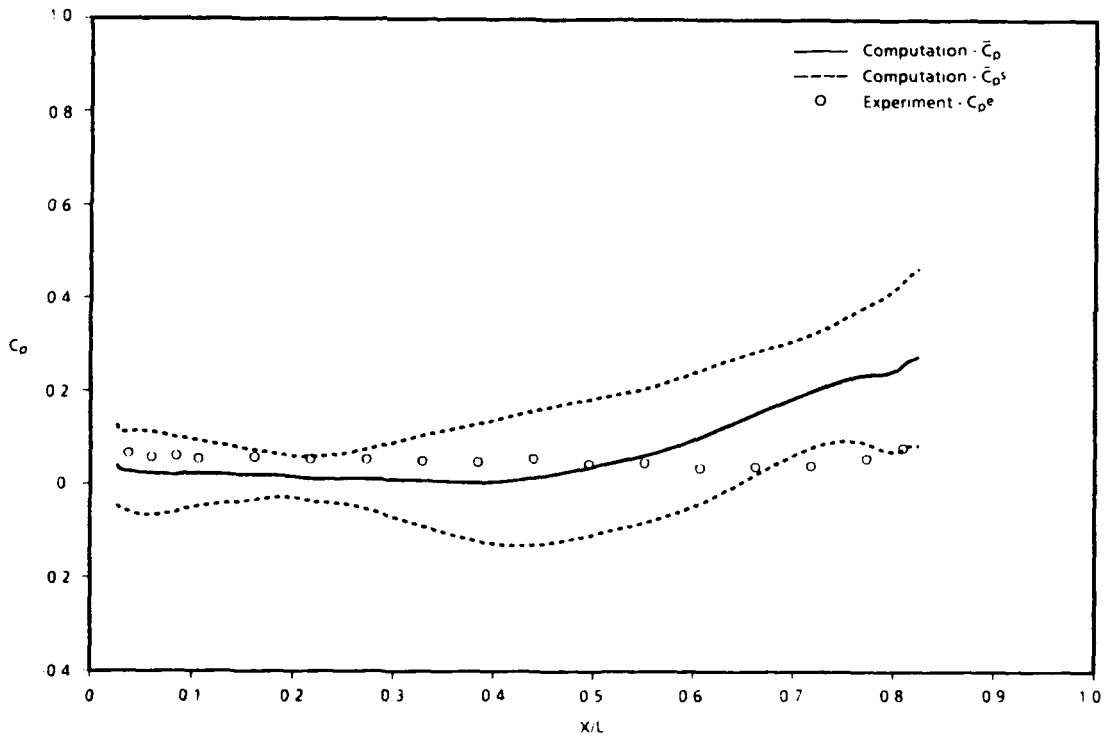


b. SPL on centerline, $Y/(W/2) = 0$

Figure 32. Comparisons of computations and measurements on the cavity walls with the store/sting present, $M_\infty = 1.20$, $Z_c/H = 0.75$.

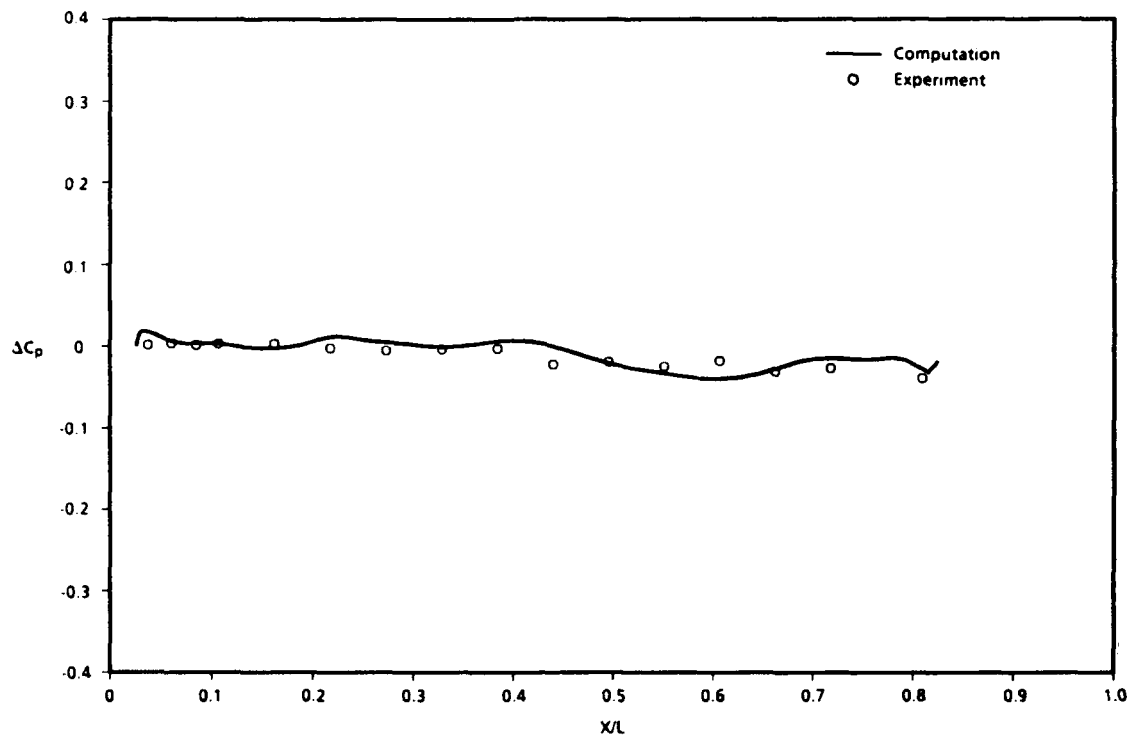


a. C_p on free-stream side

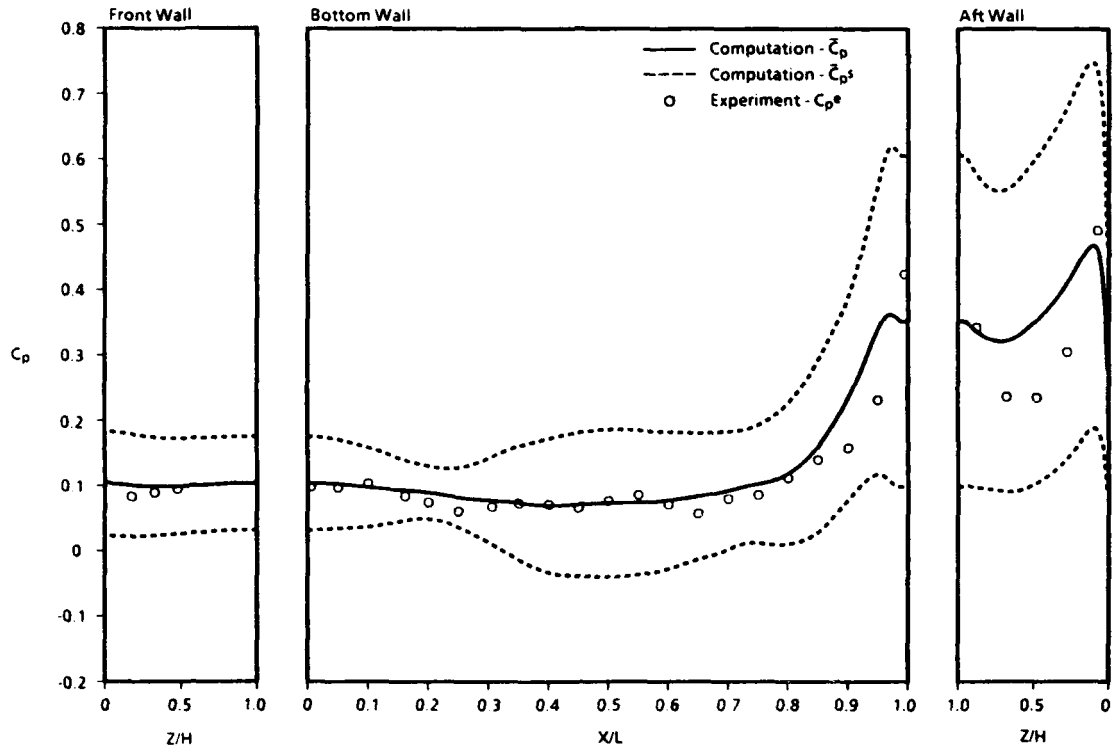


b. C_p on cavity side

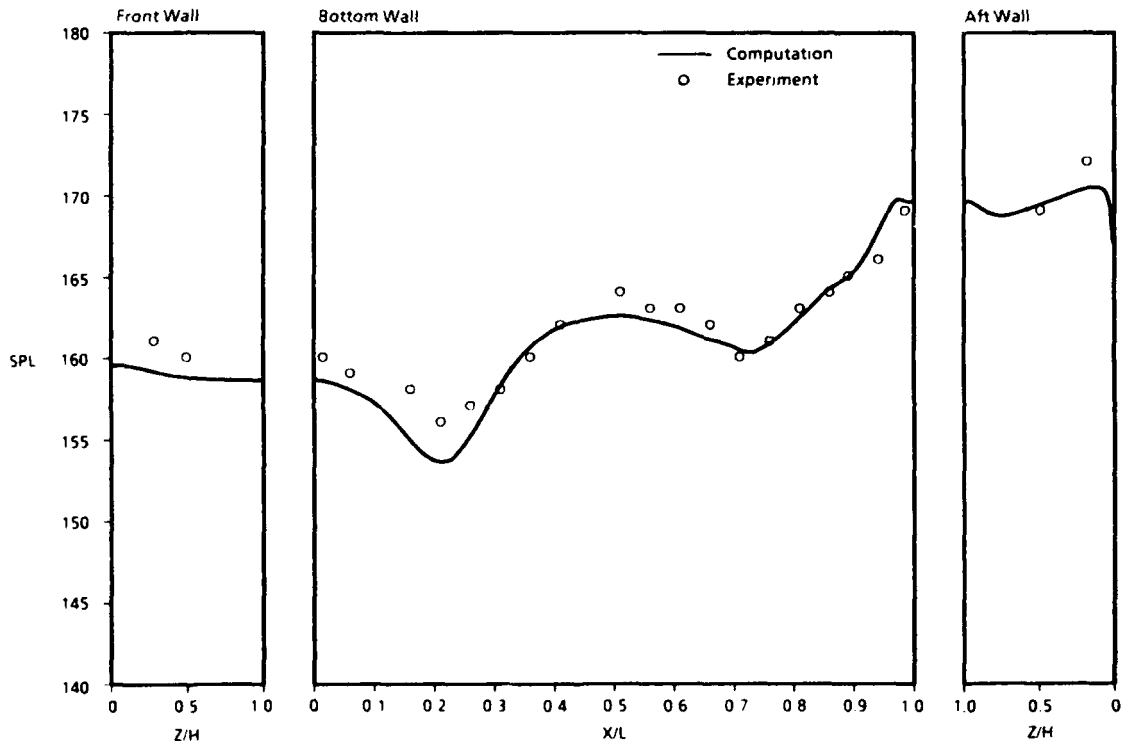
Figure 33. Comparisons of computations and measurements on the store/sting in the cavity, $M_\infty = 1.20$, $Z_s/H = 0.75$.



c. ΔC_p
Figure 33. Concluded.

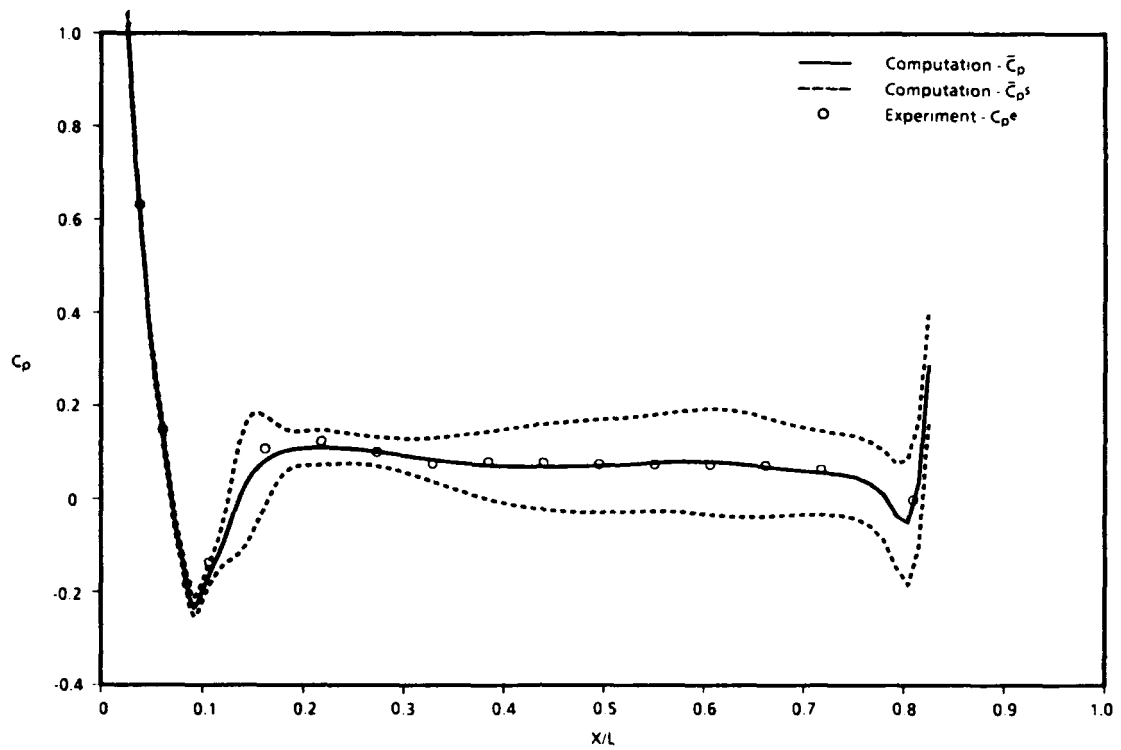


a. C_p on centerline, $Y/(W/2) = 0$

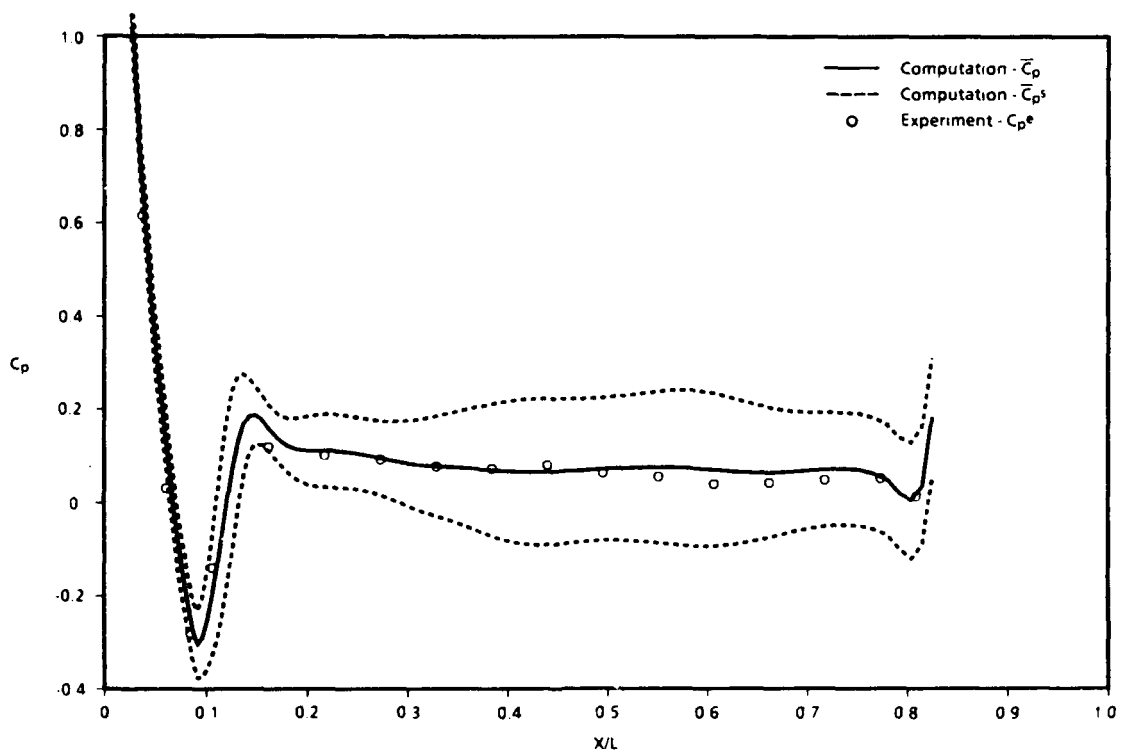


b. SPL on centerline, $Y/(W/2) = 0$

Figure 34. Comparisons of computations and measurements on the cavity walls with the store/sting present, $M_\infty = 1.20$, $Z_s/H = -0.30$.

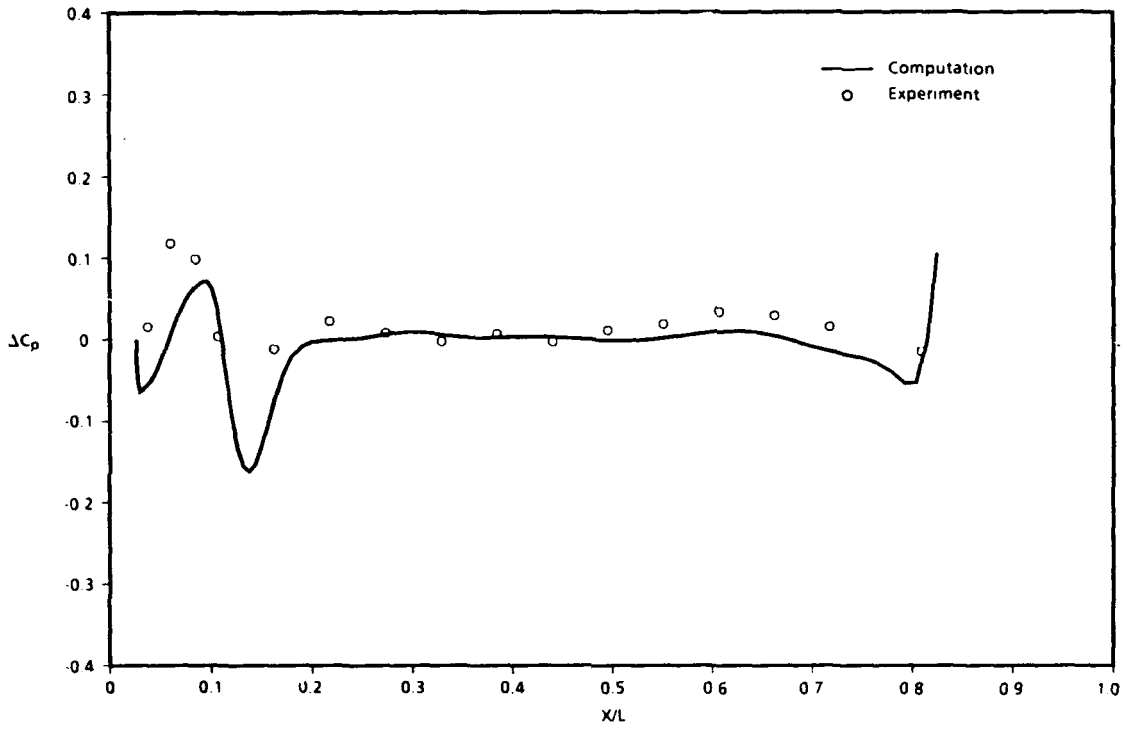


a. C_p on free-stream side



b. C_p on cavity side

Figure 35. Comparisons of computations and measurements on the store/sting in the cavity, $M_\infty = 1.20$, $Z_s/H = -0.30$.

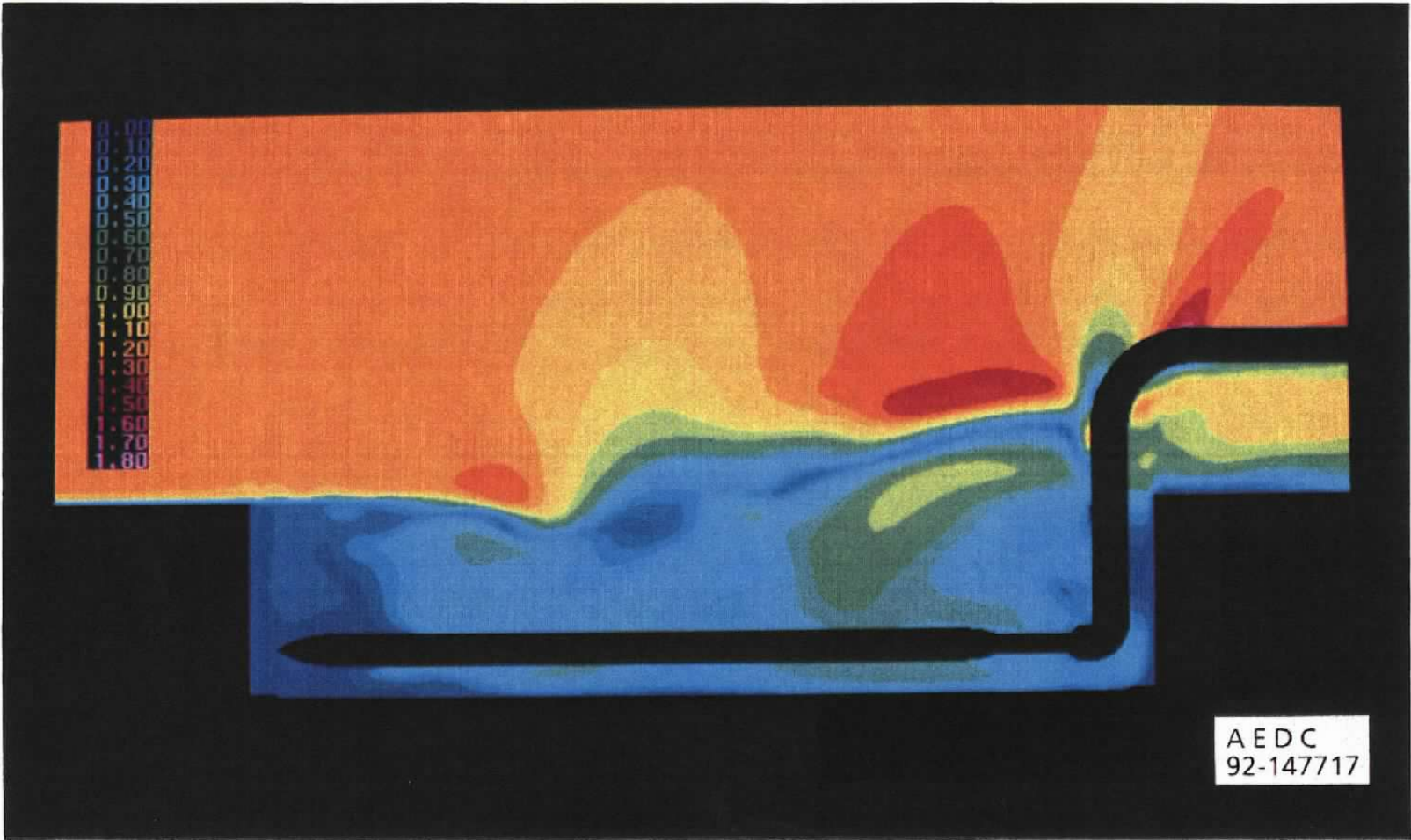


c. ΔC_p
Figure 35. Concluded.

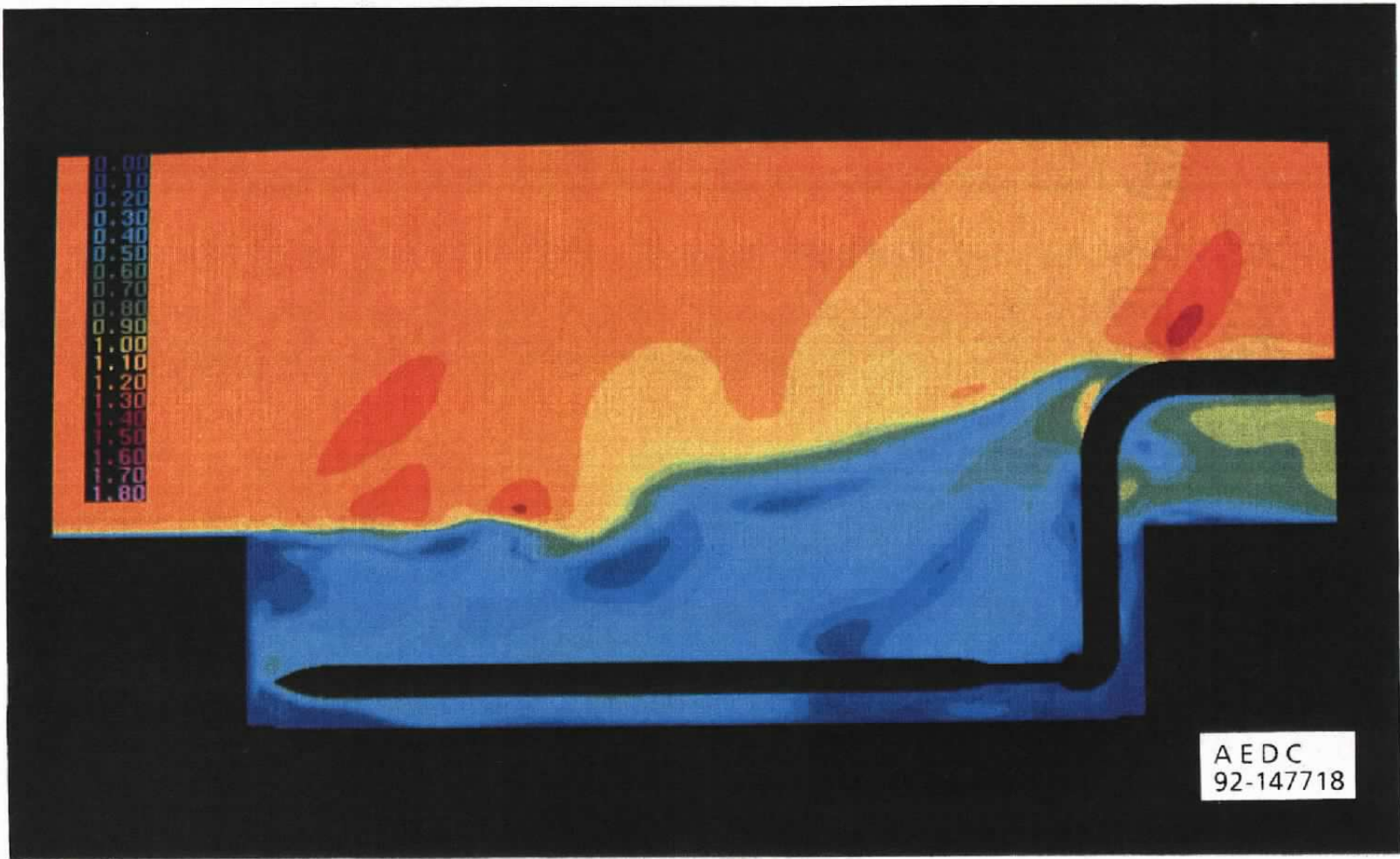


$$a. t = 6.0t_c$$

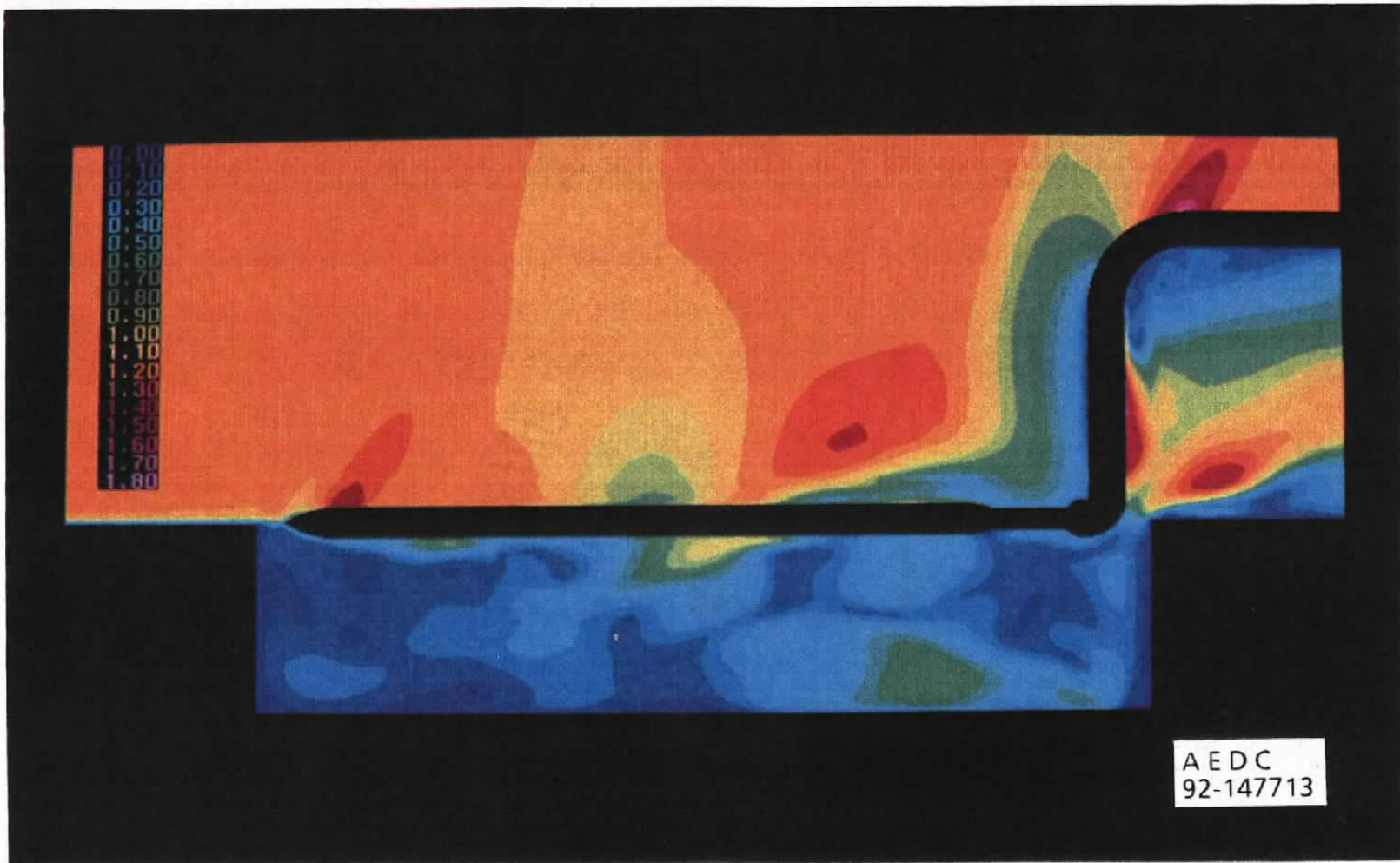
Figure 36. Mach number contours in the symmetry plane of the cavity with the store/sting, $M_\infty = 1.20$, $Z_s/H = 0.75$.



b. $t = 8.0t_c$
Figure 36. Continued.

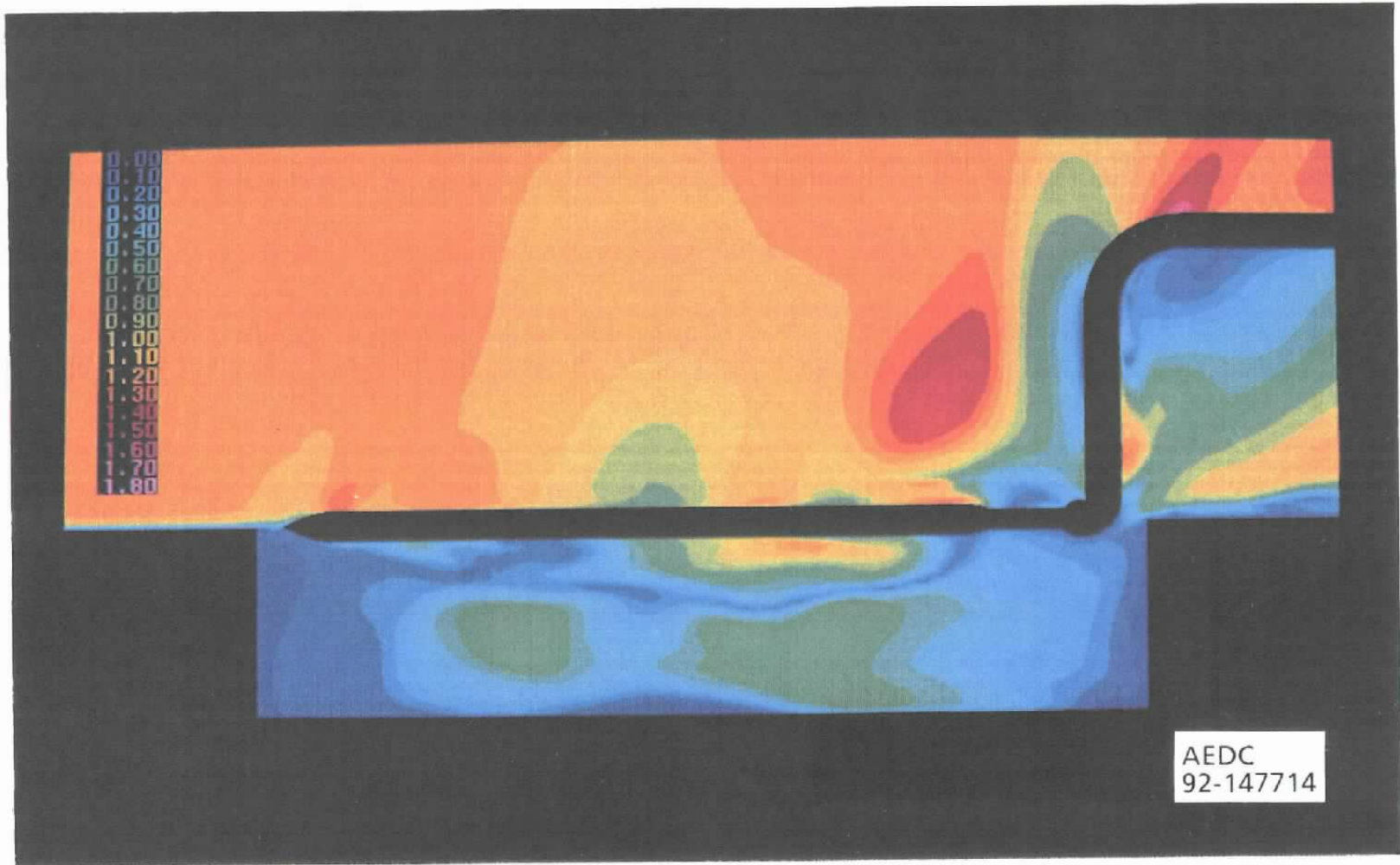


c. $t = 10.0t_c$
Figure 36. Concluded.

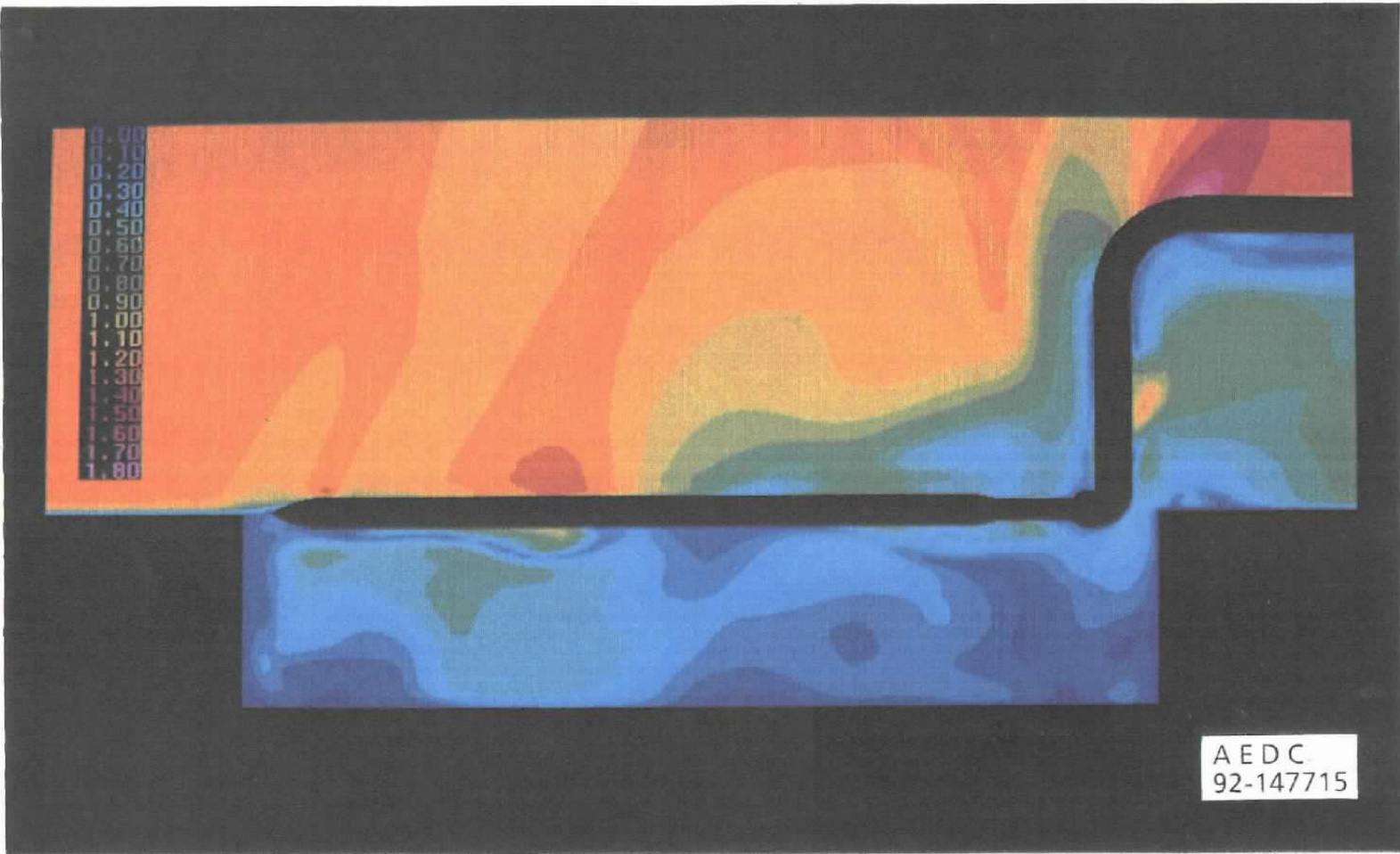


a. $t = 6.0t_c$

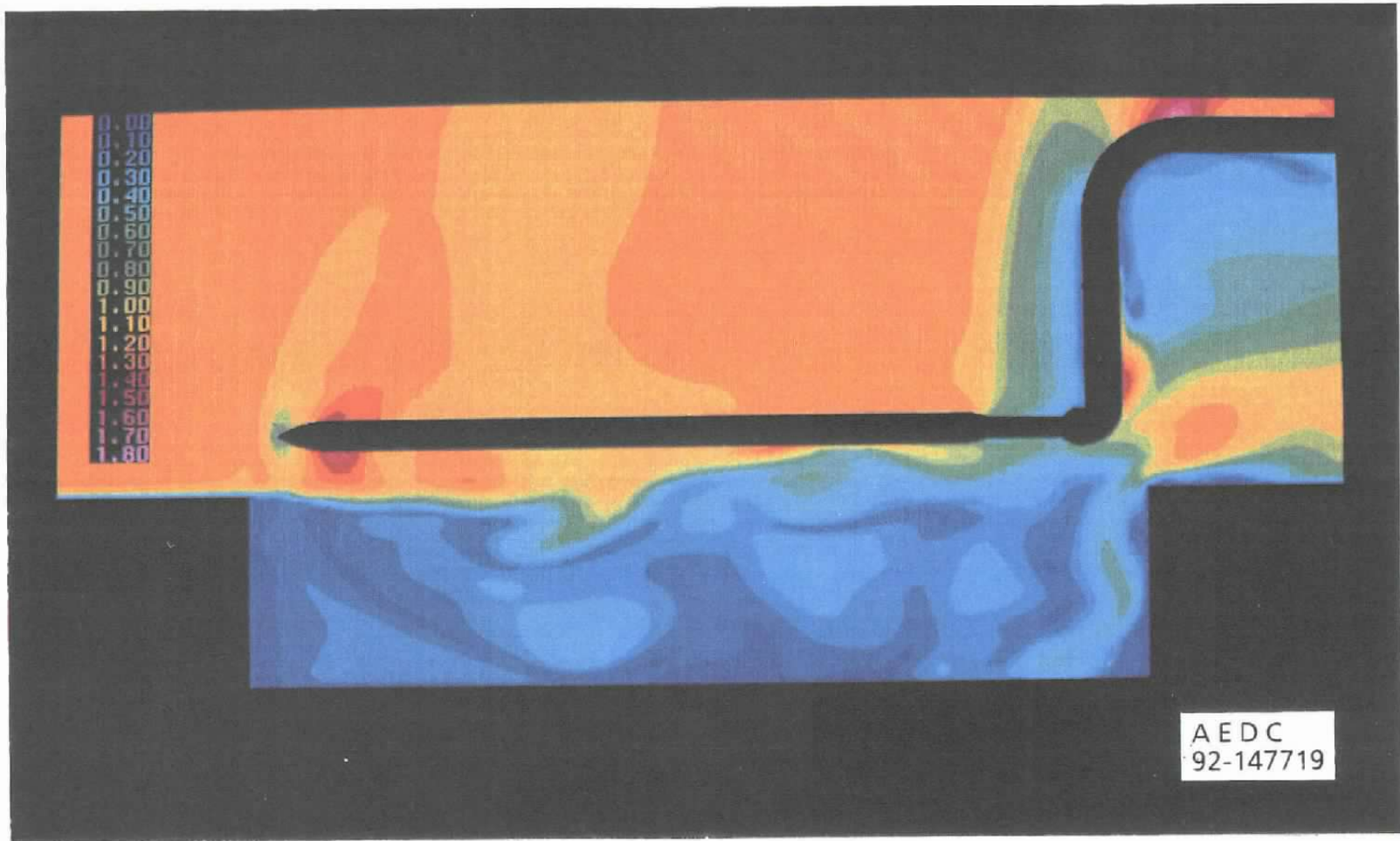
Figure 37. Mach number contours in the symmetry plane of the cavity with the store/sting, $M_\infty = 1.20$, $Z_s/H = 0$.



b. $t = 8.0t_c$
Figure 37. Continued.

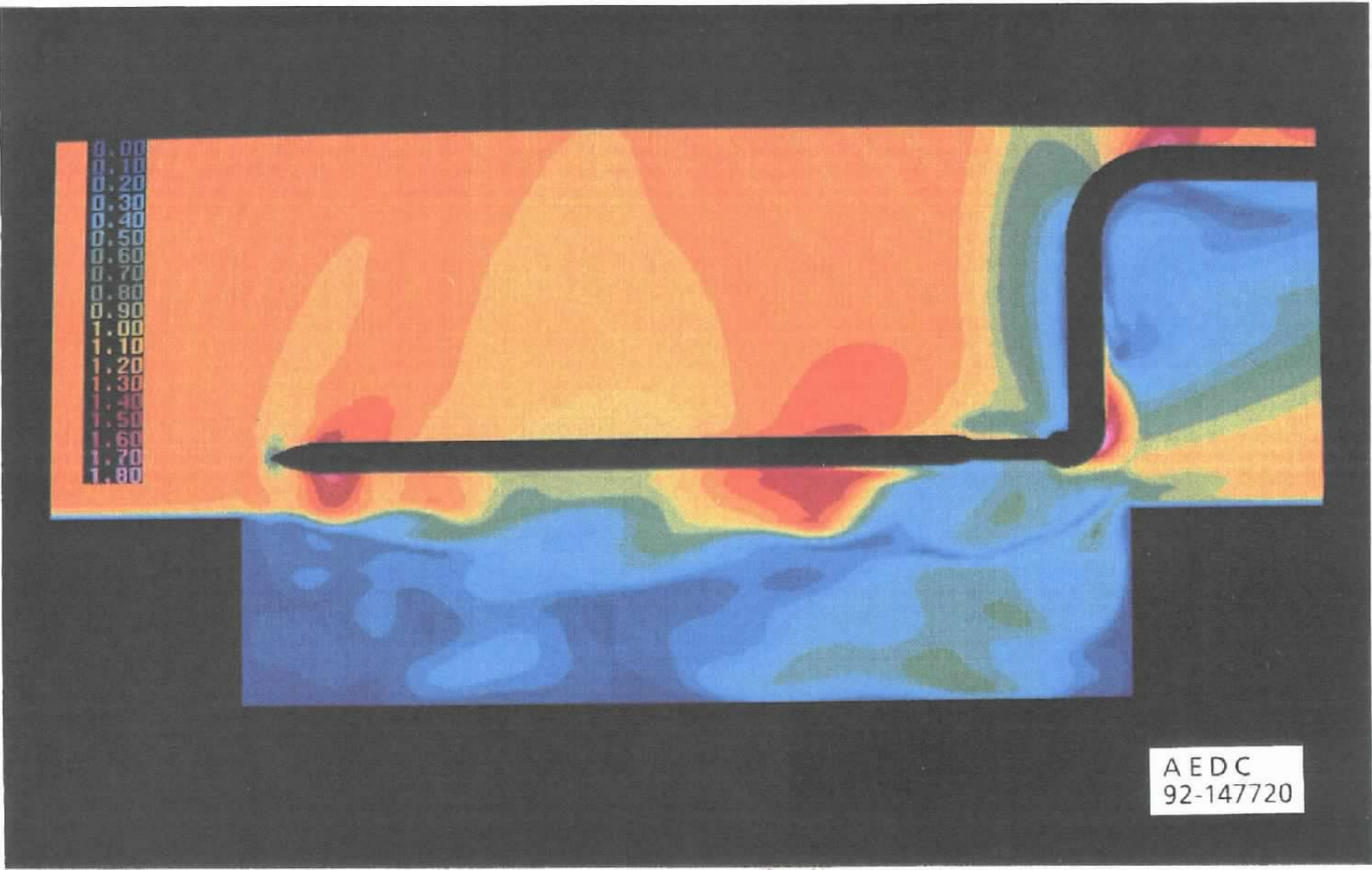


c. $t = 10.0t_c$
Figure 37. Concluded.

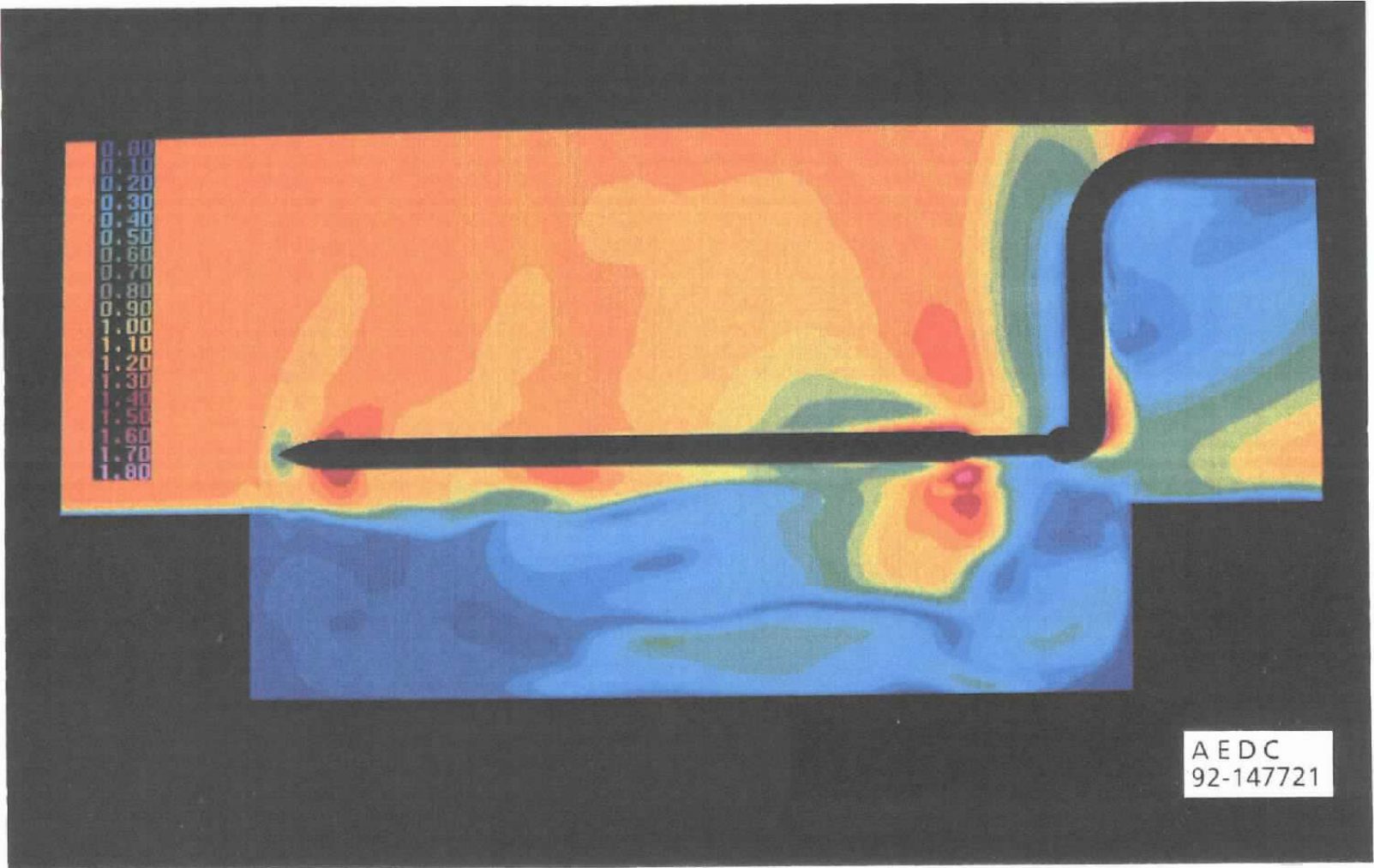


a. $t = 6.0t_c$

Figure 38. Mach number contours in the symmetry plane of the cavity with the store/sting, $M_\infty = 1.20$, $Z_s/H = -0.30$.



b. $t = 8.0t_c$
Figure 38. Continued.



c. $t = 10.0t_c$
Figure 38. Concluded.

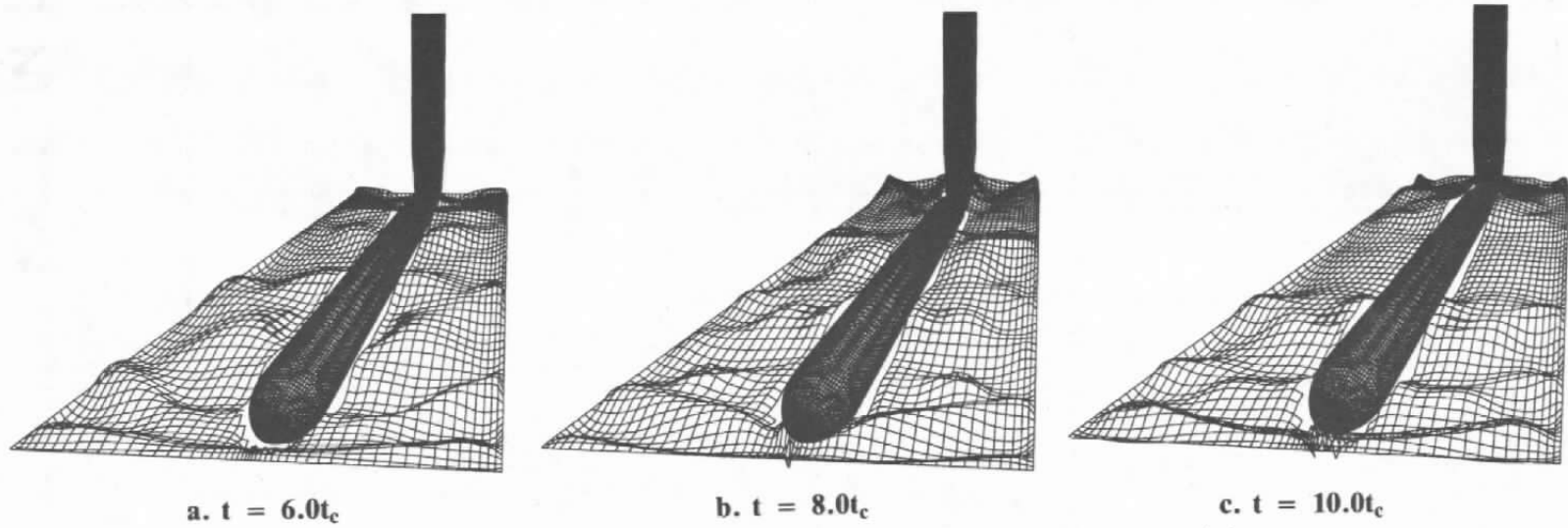
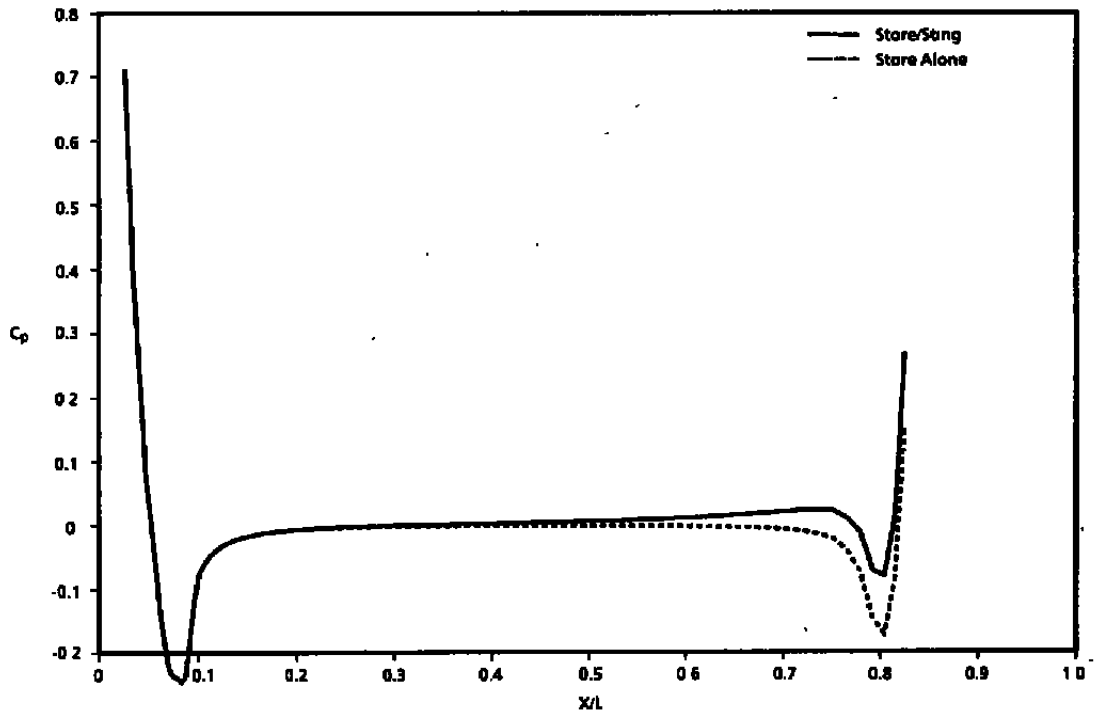
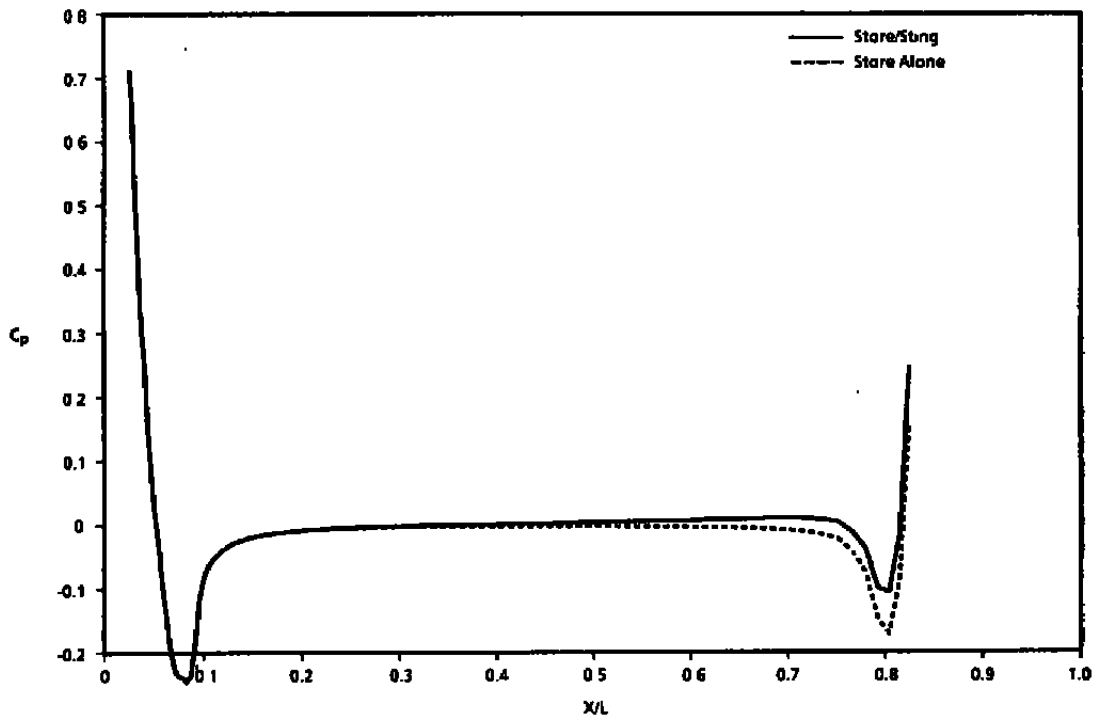


Figure 39. Mass flow through the opening of the cavity with the store/sting,
 $M_\infty = 0.60$, $Z_s/H = 0$.

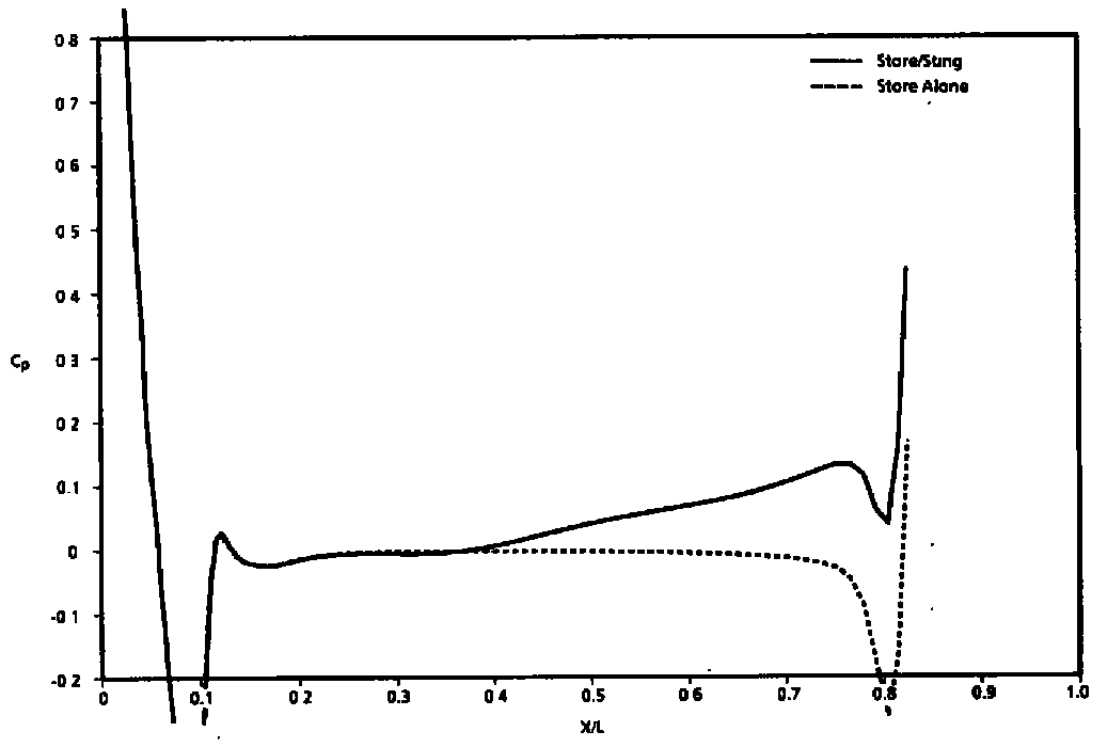


a. C_p on free-stream side

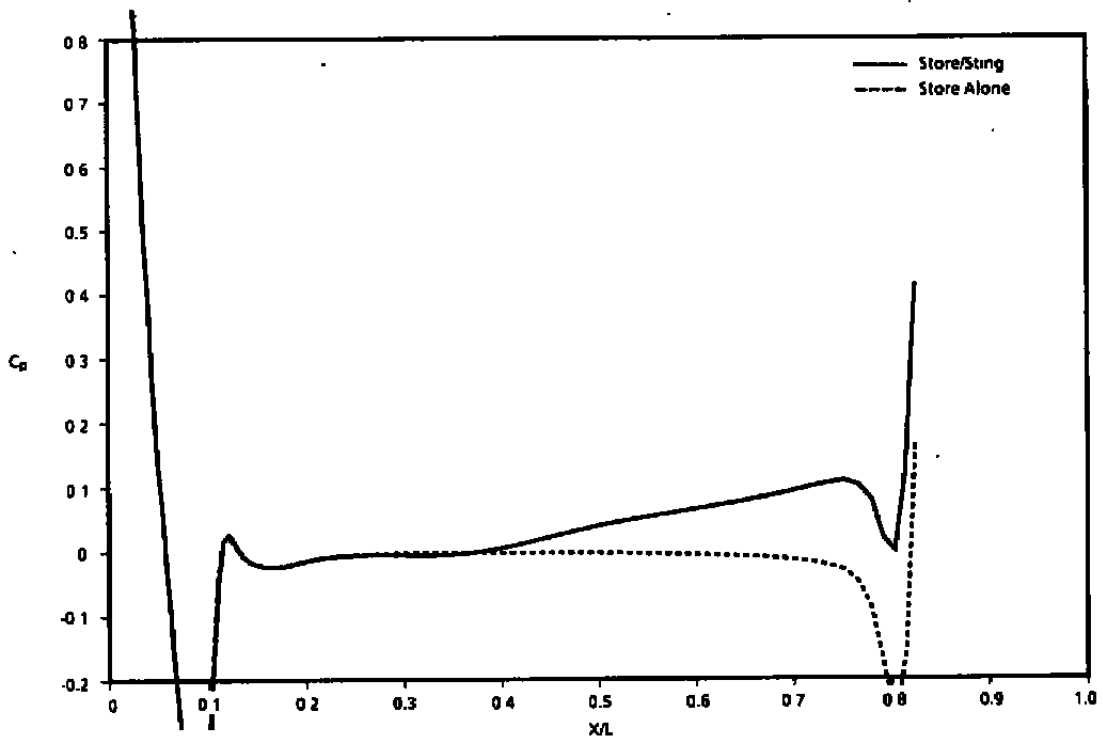


b. C_p on cavity side

Figure 40. Comparisons of computations for the store/sting and store alone in a free-stream flow, $M_\infty = 0.60$.

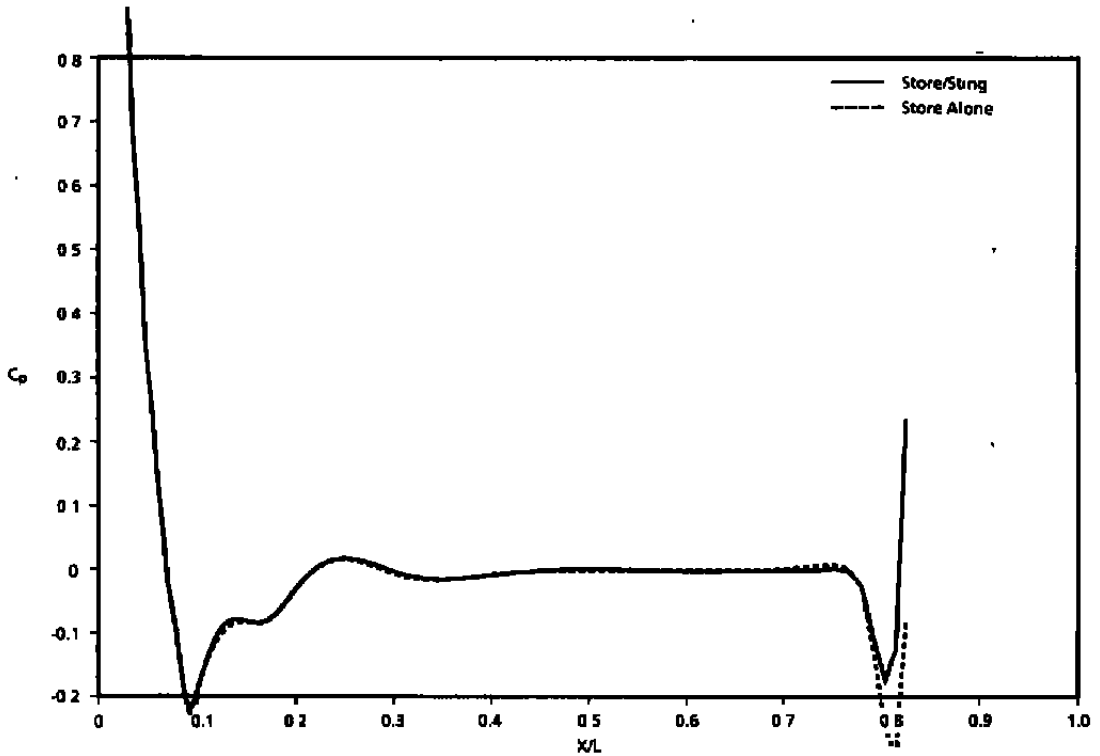


a. C_p on free-stream side

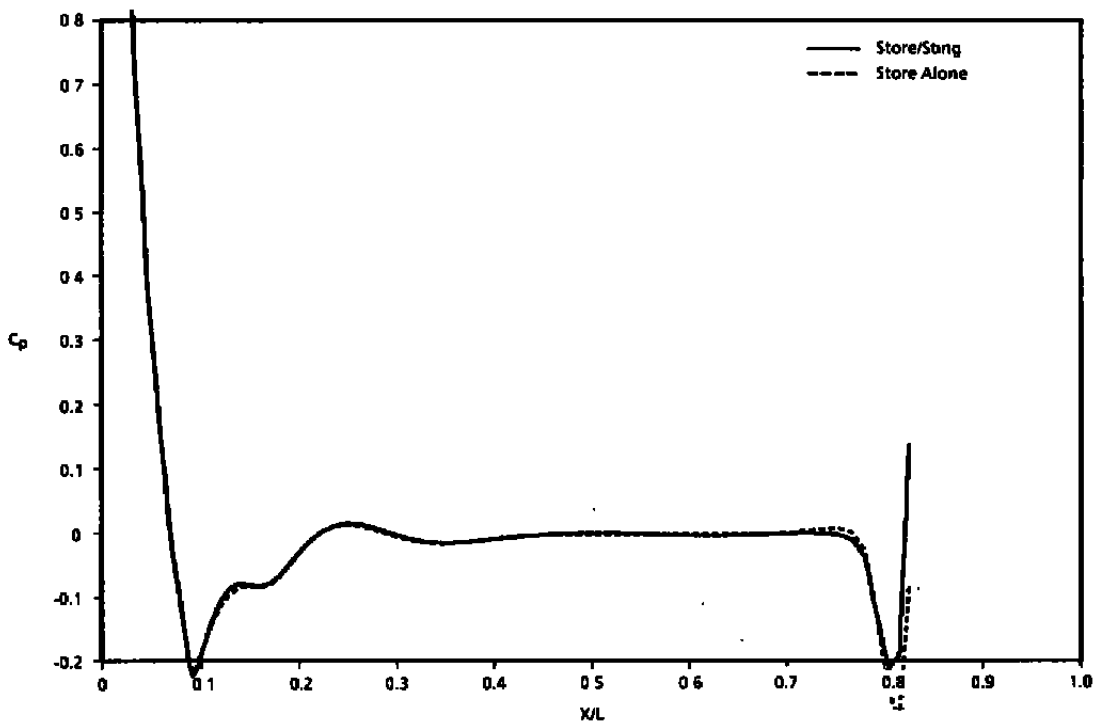


b. C_p on cavity side

Figure 41. Comparisons of computations for the store/sting and store alone in a free-stream flow, $M_\infty = 0.95$.



a. C_p on free-stream side



b. C_p on cavity side

Figure 42. Comparisons of computations for the store/sting and store alone in a free-stream flow, $M_\infty = 1.20$.

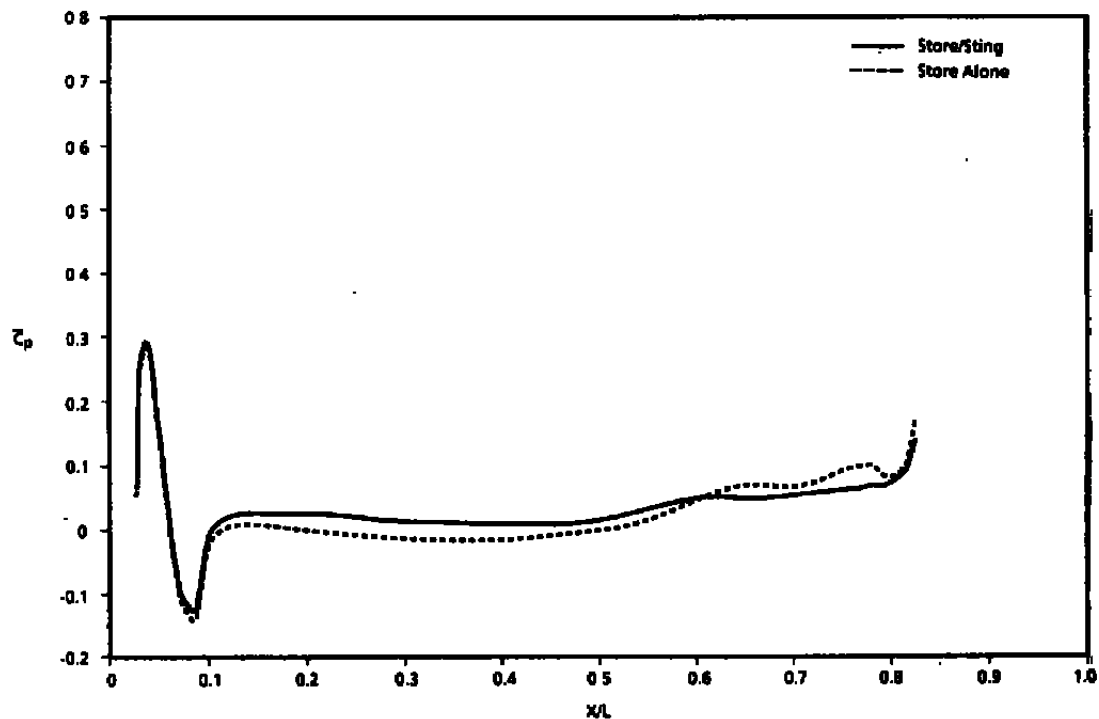
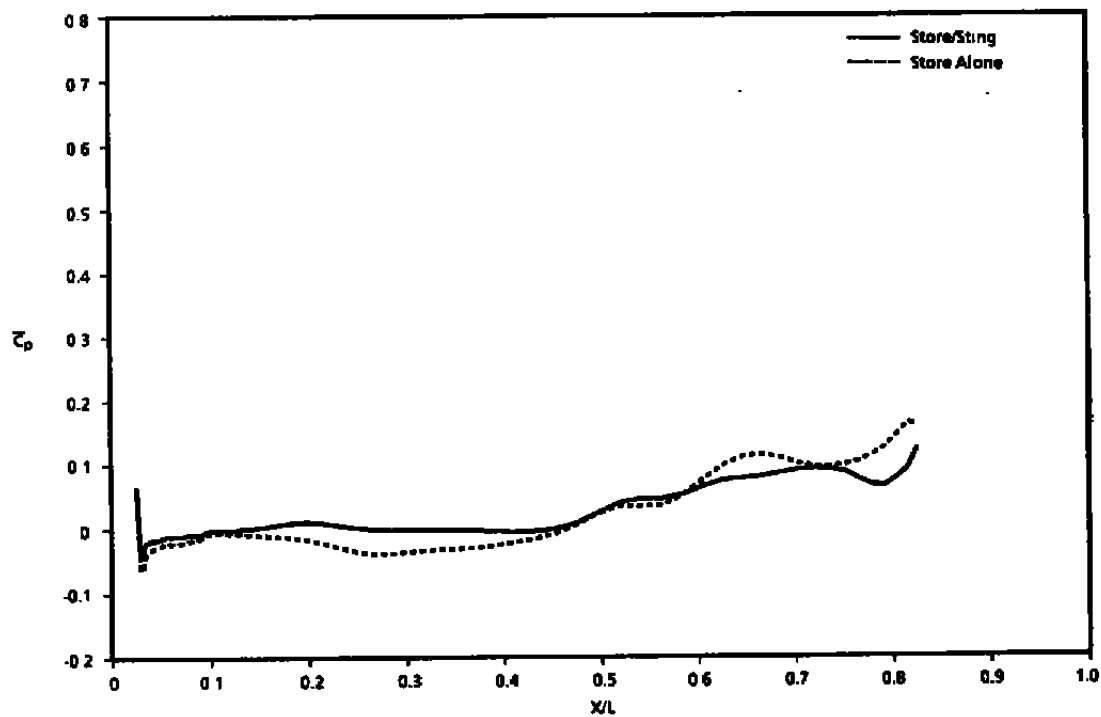
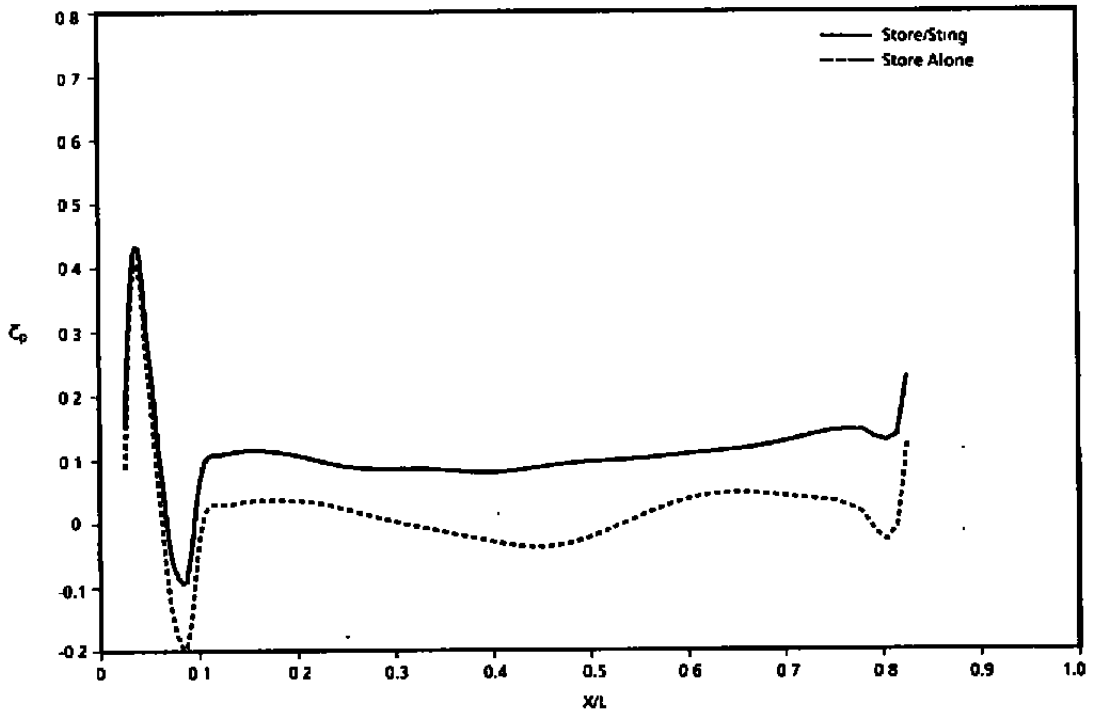
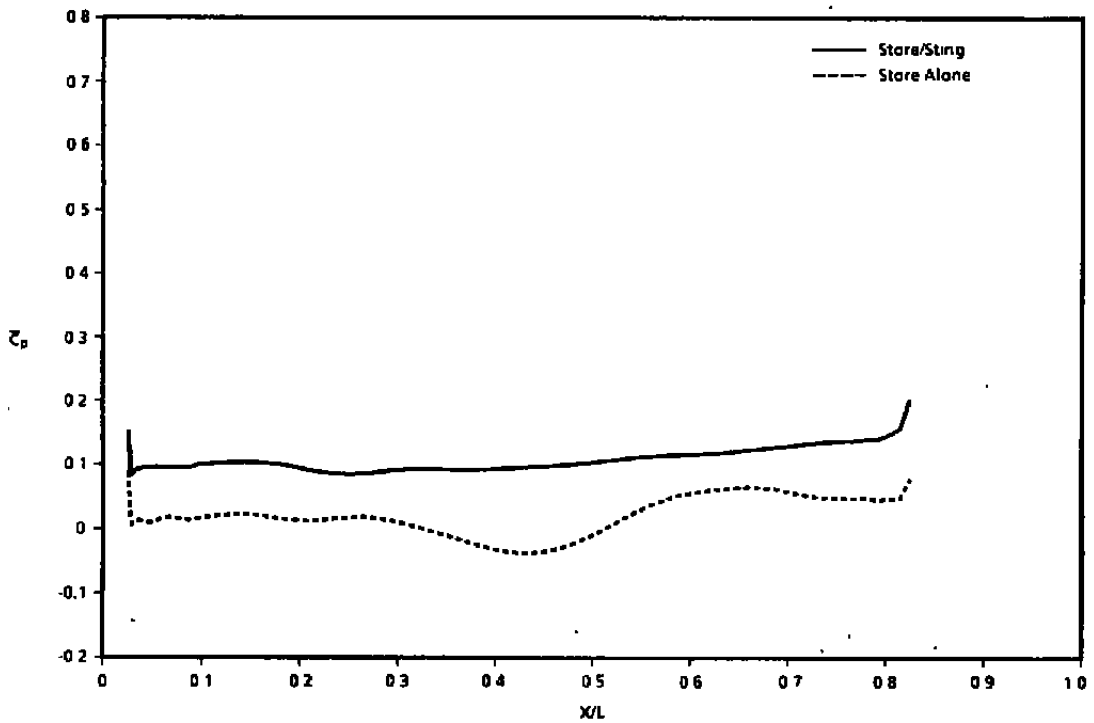
a. \bar{C}_p on free-stream sideb. \bar{C}_p on cavity side

Figure 43. Comparisons of computations for the store/sting and store alone in the cavity, $M_\infty = 0.60$, $Z_s/H = 0$.

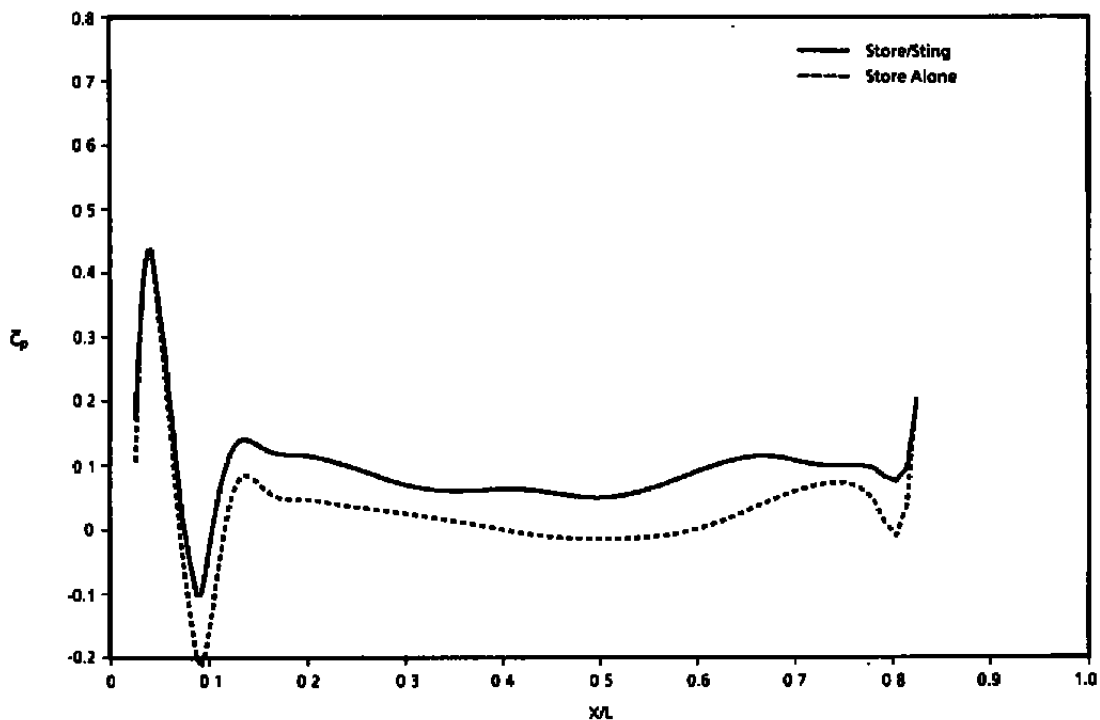


a. \bar{C}_p on free-stream side

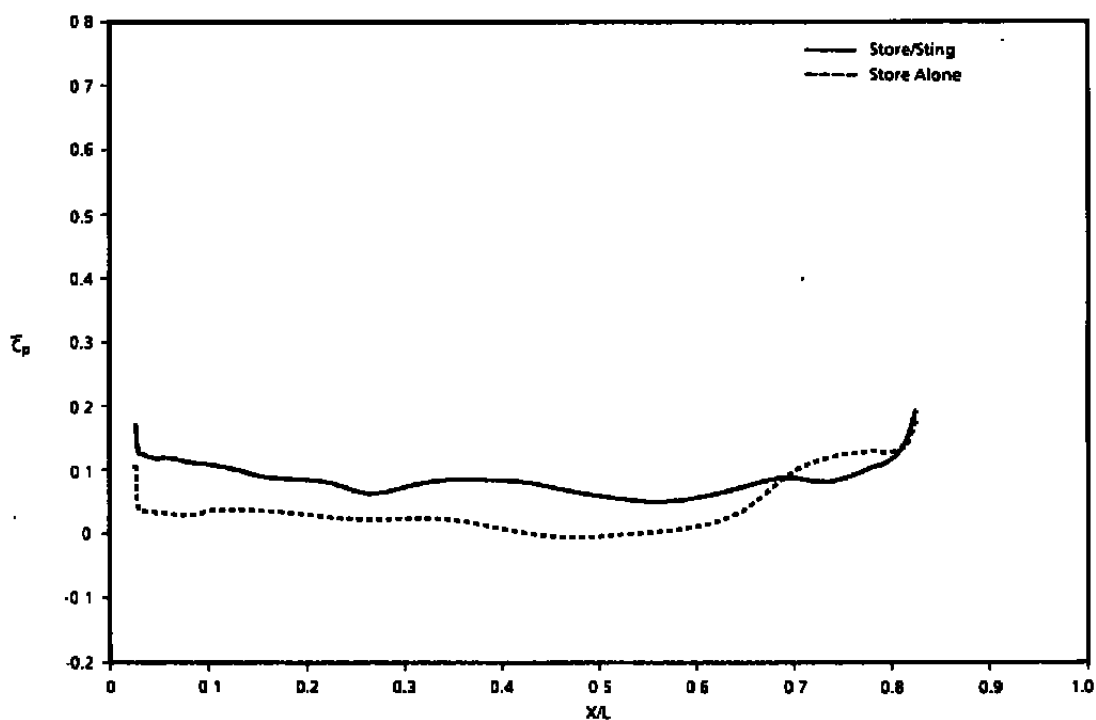


b. \bar{C}_p on cavity side

Figure 44. Comparisons of computations for the store/sting and store alone in the cavity, $M_\infty = 0.95$, $Z_s/H = 0$.

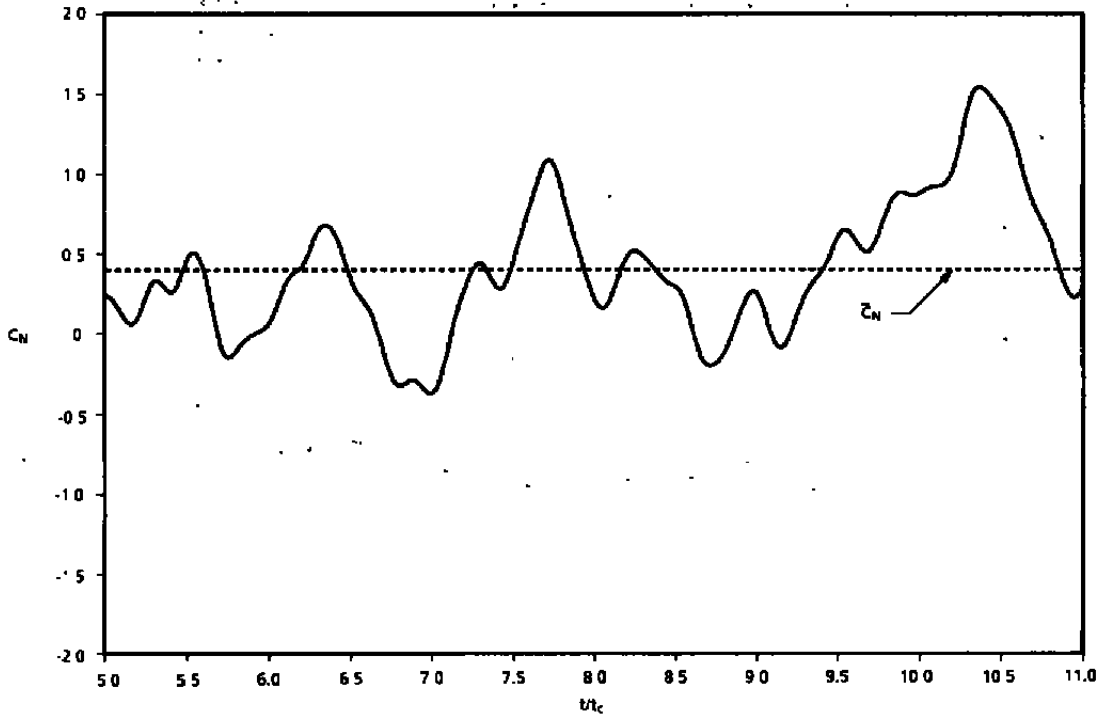


a. \bar{C}_p on free-stream side

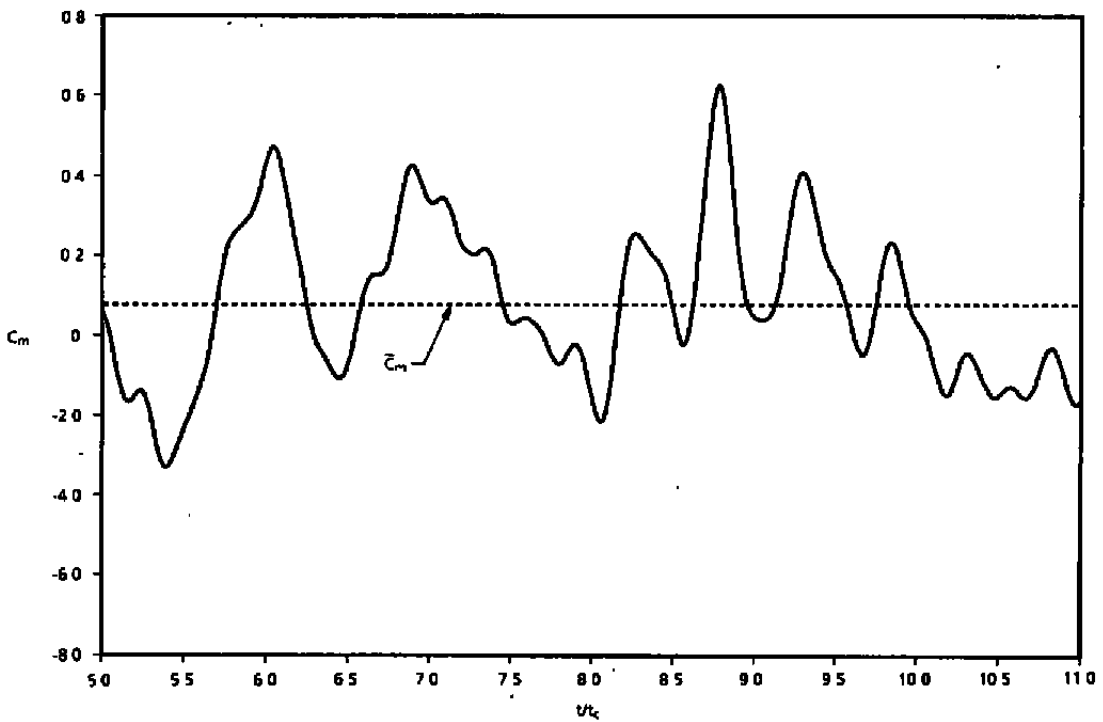


b. \bar{C}_p on cavity side

Figure 45. Comparisons of computations for the store/sting and store alone in the cavity, $M_\infty = 1.20$, $Z_s/H = 0$.

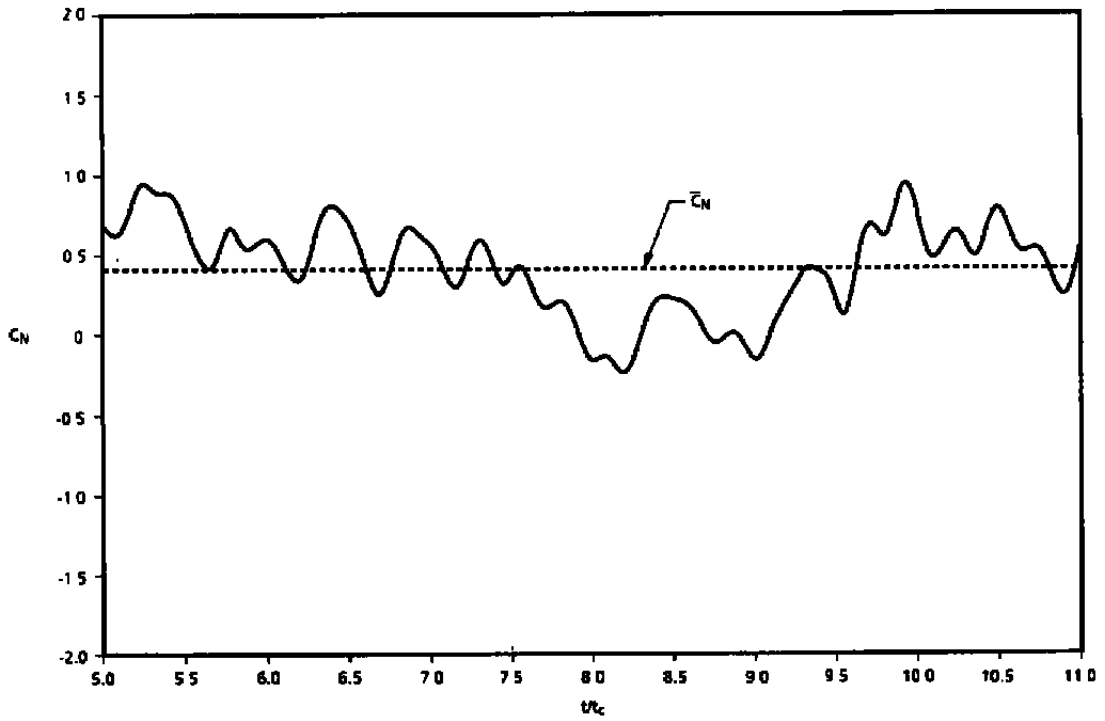


a. Normal-force coefficient, C_N

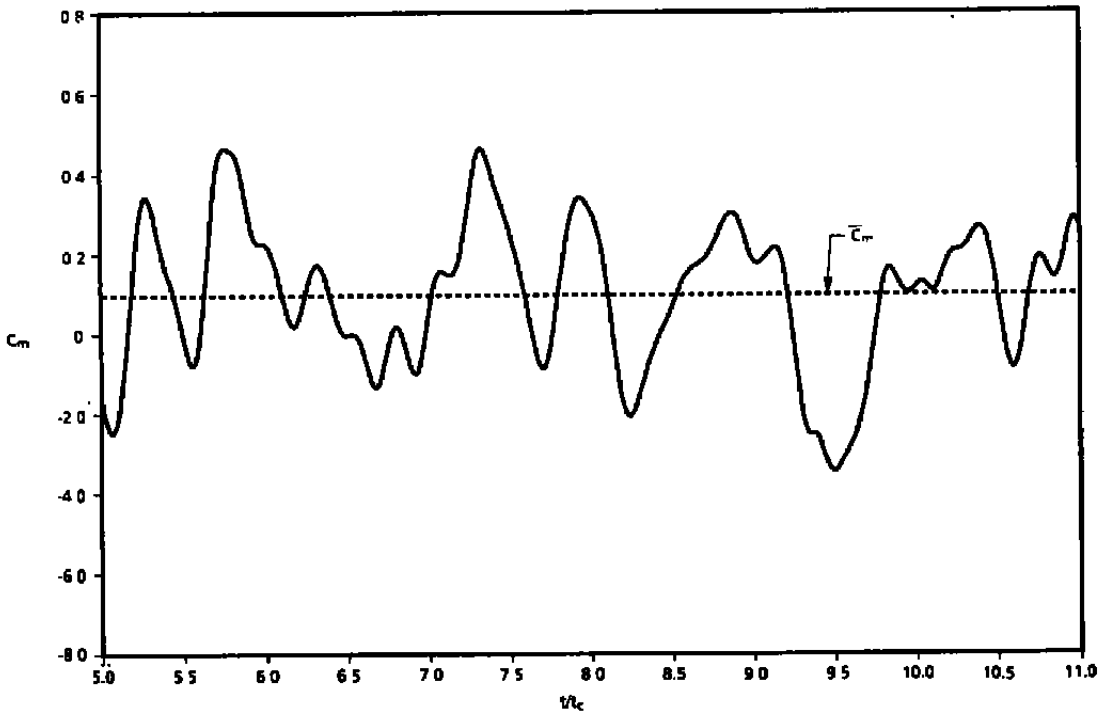


b. Pitching-moment coefficient, C_m

Figure 46. Time history of loads for the store/sting in the cavity, $M_\infty = 0.60$, $Z_s/H = 0$.



a. Normal-force coefficient, C_N



b. Pitching-moment coefficient, C_m

Figure 47. Time history of loads for the store alone in the cavity, $M_\infty = 0.60$, $Z_s/H = 0$.

Table 1. Load Comparisons for the Store/Sting and the Store Alone in the Free-Stream Flow

M_∞	C_N			C_m		
	Store/Sting	Store Alone	ΔC_N	Store/Sting	Store Alone	ΔC_m
0.60	0.085	-0.004	0.089	-0.578	0.034	-0.612
0.95	0.111	-0.002	0.113	-0.809	0.016	-0.825
1.20	0.062	0.000	0.062	-0.579	-0.005	-0.574

Table 2. Load Comparisons for the Store/Sting and the Store Alone in the Cavity, $Z_s/H = 0$

M_∞	\bar{C}_N			\bar{C}_m		
	Store/Sting (σ)	Store Alone (σ)	$\Delta \bar{C}_N$	Store/Sting (σ)	Store Alone (σ)	$\Delta \bar{C}_m$
0.60	0.398 (0.426)	0.411 (0.288)	-0.013	0.791 (1.991)	0.976 (1.817)	-0.185
0.95	0.151 (0.430)	0.015 (0.327)	0.136	1.032 (2.226)	1.203 (2.098)	-0.171
1.20	0.262 (0.526)	-0.044 (0.377)	0.306	-0.146 (3.219)	1.943 (2.672)	-2.089

NOMENCLATURE

a	Local speed of sound
a_∞	Free-stream speed of sound
C_m	Coefficient of pitching moment about an axis through the center of gravity of the store which is parallel to the Y axis, pitching moment/ $q_\infty SD$, positive counterclockwise looking in from the + Y direction (nose down into the cavity)
C_N	Coefficient of normal force in the XZ plane, normal force/ $q_\infty S$, positive in the +Z direction
\bar{C}_m	Pitching moment (C_m) obtained from time-averaged computational results
\bar{C}_N	Coefficient of normal force (C_N) obtained from time-averaged computational results
C_p	Pressure coefficient
C_p^e	Pressure coefficient obtained from the experimental data
\bar{C}_p	Pressure coefficient obtained from time-averaged computational results
\bar{C}_p^s	The sum of \bar{C}_p plus/minus the standard deviation of the time history of the calculated pressure coefficients about \bar{C}_p
D	Maximum diameter of the store
H	Cavity height
L	Cavity length
M_∞	Free-stream Mach number
P_{ref}	Standard reference pressure (2.90075 psi)
P_{rms}	Root-mean-square of the pressure fluctuations about the average, in psi
q_∞	Dynamic pressure in the free stream

S	Area of maximum cross section of the store
SPL	Sound pressure level
T_{avg}	Time interval for computing time averages
t_c	Characteristic time, i.e., the time required for the flow to traverse the length of the cavity
u,v,w	Velocity components in the X, Y, and Z directions, respectively
W	Width of the cavity
X,Y,Z	Rectangular coordinate system (see Fig. 12)
Z_s	Z location of the store
ΔC_m	Difference in C_m , the store with the sting minus the store without the sting [see Eq. (6)]
ΔC_N	Difference in C_N , the store with the sting minus the store without the sting [see Eq. (5)]
ΔC_p	Difference in C_p of the free-stream side minus the cavity side of the store [see Eq. (4)]
Δt_f	Minimum time step required to resolve the physically significant frequencies of the flow
Δt_i	Minimum time step required for stability of inviscid flow solver [see Eq. (1)]
Δt_v	Minimum time step required for stability of compressible Navier-Stokes flow solver [see Eq. (2)]
Δu	$u - a_\infty M_\infty$; to first order, $\Delta u = -a_\infty M_\infty C_p / 2$
$\Delta \bar{u}$	Time-averaged value of Δu

$\Delta X, \Delta Y, \Delta Z$ Grid spacing in the X, Y, and Z directions, respectively

ρ Density

σ Standard deviation

μ Viscosity